Phase separation and temperature effects in mixture of two atomic species

ScuDo

Scuola di Dottorato ~ Doctoral School

WHAT YOU ARE, TAKES YOU FAR

Doctoral Dissertation

Doctoral Program in Physics (29^{th}cycle)

Phase separation and temperature effects in mixture of two atomic species

By

Fabio Lingua

******

Supervisor(s):

Prof. Vittorio Penna, Supervisor

Doctoral Examination Committee:

Prof. Raffaella Burioni , Referee, Università degli Studi di Parma

Prof. Chiara Fort, Referee, LENS European Laboratory for Non-linear Spectroscopy and Università di Firenze

Prof. Michele Caselle, Università di Torino

Prof. Alessandro Pelizzola, Politecnico di Torino

Prof. Mario Trigiante, Politecnico di Torino

Politecnico di Torino

2017

Declaration

I hereby declare that, the contents and organization of this dissertation constitute my own original work and does not compromise in any way the rights of third parties, including those relating to the security of personal data.

Fabio Lingua
2017

* This dissertation is presented in partial fulfillment of the requirements for **Ph.D. degree** in the Graduate School of Politecnico di Torino (ScuDo).

Abstract

This thesis investigates bosonic mixtures in ultra-cold atom systems. We mainly focus on mixtures of two bosonic twin-species trapped in optical lattices, paying particular attention to the properties of spatial separation. The study is carried out by means of the path-integral quantum Monte Carlo by the two-worm algorithm and by analytical calculations where the complexity of the system allows it. The mixture is trapped in a square optical lattice at different filling and temperature conditions. We explore the ground-state phase diagram showing that various quantum phases can arise depending on the interplay between intra- and inter-species interactions. Demixed phases, characterized by spatial separation of the two species, are studied in details determining under which conditions they can be stabilized. The influence of temperature, filling factor and harmonic trap on phase separation is also investigated. An interesting dependence of the degree of demixing from temperature has been found, suggesting new ways to measure the temperature of a two-component bosonic mixture.

We also study spatial phase separation in the simple case of a two-component mixture in a double-well potential both numerically and by means of the *Bogoliubov approximaton*. We show that even in this simple case the main features of the mixing/demixing phase transitions are observed, and that the transition is characterized by a spectral collapse of the energy eigenvalues reflecting the dramatic change of algebraic structure of the model.

Contents

Introduction

Mixtures of two bosonic species in cold-atom systems feature a variety of unprecedented effects and quantum phases [1]-[26] resulting from the interplay between kinetic energy and intra-, inter-species density-density interactions. In the past decade, a considerable theoretical work has been devoted to investigate manifold properties of both lattice and continuous systems. Different aspects of the phase diagram have been studied by means of generalized mean-field schemes [16]-[18], Luttinger-liquid picture [19], or perturbation methods [20]. Moreover, the effect of phase separation [82, 22], the study of quantum emulsions and coherence properties of mixtures [23, 24], and the shift of Mott domains due to the presence of a second (superfluid) species [25] along with the interpretation of this shift in terms of polaron excitations [26] have been explored.

In the limit of large interactions, magnetic-like phases such as the incompressible double-checkerboard solid and the supercounterflow have been predicted theoretically [1]-[4] at total filling one and repulsive inter-species interaction, while paired superfluidity has been found [5] in the case of attractive inter-species interaction at equal integer filling of the two components. These findings stimulated further investigation of magnetic-like phases including finite temperature effects [10, 14], different optical lattice geometries [15] and dimensionality, and various interacting regimes [6]-[13], [20]. Nevertheless, over the ten years from initial theoretical investigation of these systems [1]-[4], their rich phase diagram still exhibits several unexplored aspects that challenge theoretical and numerical techniques, while its elusive character demands more sophisticated experimental techniques for the observation of these quantum phases.

The recent experimental realization of mixtures, either combining two different atomic species [27, 28] or using the same atomic species in two different internal energy states [29–32] demonstrated how refined experimental techniques allow to

control the model parameters, hence reinforcing the interest toward these systems. The possibility to observe such new phases in real systems is strongly affected by *i*) the presence of the trapping potential which introduces an undesired source of inhomogeneity, *ii*) the fact that their theoretic prediction is based on assuming rather ideal conditions (such as, for example, species A and B with the same boson numbers $N_a = N_b$, or large intra-species interactions), and *iii*) the difficulty in reaching low enough temperatures where such phases are expected. Concerning points *i*) and *ii*), the experimental realizability of magnetic phases has been analyzed in [33] leading to promising results at least for the double checkerboard phase.

Furthermore, in the past few years brand new experimental techniques [34–39] opened the possibility to resolve the observation of an optical lattice down to a single-site scale. This new and intriguing experimental opportunity, is potentially useful from the point of view of the detection of magnetic phases and related phenomena like phase separation.

In this thesis we basically study bosonic mixtures in ultra-cold atom systems. We focus our attention to investigate mixtures of two bosonic *twin*-species trapped in a two-dimensional, square, optical lattice. The study is carried out from the theoretical point of view by means of simulations through the Two-worm algorithm Quantum Monte Carlo [40], as well as by means of analytical computation where the complexity of the system allows it. The investigation is performed in both the homogeneous (periodic boundary conditions) and harmonically trapped cases. It is focused on the reconstruction of the ground-state phase diagram, paying particular attention to the conditions under which the different quantum phases can be stabilized. In particular, this thesis focuses on the study of the demixing effect that arise in the so-called *demixed phases*, namely: demixed Superfluid and demixed Mott-insulator phases. A demixed phase is a quantum phase in which the two components of the mixture are physically separated on the lattice. Phase-separation is studied in details both in the ground-state, and at finite temperature. An interesting competitive relationship between the demixed phases and the temperature of the system has been found. The key-point is that temperature fluctuations tend to destroy phase separation, and this can be very efficiently detected by means of a suitable demixing estimator. By exploiting the thermometric property of the phase separation it is possible to properly design a new thermometry technique capable to measure the temperature in ultra-cold mixtures through fundamental principle of miscibility. The technique is

proven to work well in both weakly- and strongly-interacting regimes filling a sorely felt need where standard and conventional techniques lack on reliability.

Measuring the temperature in optical lattices may be indeed cumbersome and far from trivial. Ultra-cold atoms are quite generally regarded as an almost ideal experimental setting to investigate many-body quantum physics in strongly correlated regimes [41]. However, atomic systems suffer from some notable limitations. Measuring fundamental parameters, such as temperature, for strongly correlated quantum gases can be very challenging. The main physical reason is because the primary thermometric quantity used in these systems is the momentum distribution. Momentum distributions in optical lattices can be measured through standard absorption images technique (Time-Of-Flight images) and can be relatively easy to obtain in standard experimental setups. However, in strongly-correlated regimes momentum distributions are often dominated by quantum rather than thermal fluctuations thereby becoming quite insensitive to temperature variations. Because of the lack of reliable estimator, thermometry for optical lattices in the last years stimulated numerous theoretical proposals and experiments [42]. Up to date, the main experimental techniques used for thermometry of optical lattice systems exploits either ancillary samples [43, 44, 85, 47], or measure of local density fluctuations with high-resolution imaging [34–39]. However, seminal works have been reported both with bosonic and fermionic samples. In 2009 demixing between two spin components of Rubidium atoms was induced by a magnetic field gradient and the width of the interface region was used to estimate the temperature [43]. While recently, the spin waves (magnons) in a spinor Rb condensate were used to reduce the entropy per particle to values as low as $0.02\,k_B$ [48]. On the fermionic side, anti-ferromagnetic correlations have been detected by means of Bragg scattering [49], and also, very recently, directly by means of single-site imaging [50–52]. However, all the methods mentioned above work well in the weakly-interacting regime, but lack on reliability when the interaction become strong enough. Within the effort to contribute to the research of a universal and standard method for thermometry of strongly correlated quantum gases, with our proposal we suggest a method particularly suitable for temperatures of the order of the tunneling energy, where “quantum magnetism” is expected, capable of filling the gap between the two interaction regimes.

In the spirit of trying to provide a more complete and exhaustive investigation, we finally focus on the study of the simple two-well lattice model (equivalent to a two-sites BH model) from the analytical and numerical point of view. Despite the

simplicity of the model, the analytical study reveals how the most fundamental and general principles found in the more accurate and complete analysis of more complex systems, can be grasped by the knowledge of much simpler one. By analyzing the simple and symmetric two-site and two-species Bose-Hubbard (BH) model by means of the *Bogolubov approximation*, we found indeed that the mixing/demixing phase transition can be interpreted as a change of the underlying algebraic structure of the model. And how this change is witnessed by the spectral collapse of the energy-eigenvalues.

This thesis is organized as follows. In the first chapter we analyze and derive the theoretical model underlying our study. We introduce the theoretical framework of the second-quantization formalism and we discuss the assumptions and hypothesis that lead to the derivation of the so called Bose-Hubbard model. We initially work considering a single weakly-interacting bosonic gas trapped in a periodical lattice. We then extend the picture to the case of two bosonic species, and derive the Hamiltonian of the Two-Species Bose Hubbard model.

In the second chapter we review and examine the Quantum Monte Carlo Algorithm used for our simulations. We describe the method and we unveil the key features of the worm-algorithm Quantum Monte Carlo [53, 54, 40]. We then move to analyze the results of our study. In chapter 3 we reconstruct the ground-state phase diagram of a mixture of two bosonic twin species trapped in an homogeneous optical lattice at commensurate unitary filling. We examine the property of phase separation, and the condition under which the different quantum phases can be stabilized and experimentally detected by means of Time-Of-Flight images. We then move to discuss both phase diagram and demixed phases for non-integer fillings and in the presence of a confining Harmonic potential. Within the latter scenario we study the momentum distributions and the experimental detectability of the different phases; we also investigate the appearance of spatial-shell-structures where different quantum phases can coexist due to the imposed variable local density.

In chapter 4 we study the system at finite temperature in both the homogeneous and the trapped case. We analyze phase separation away from $T = 0$ reconstructing the behaviour of the demixing parameter as a function of the temperature in both weakly and strong interacting regimes. In chapter 5 we exploit then these thermometric properties in order to propose a new method for measuring the temperature in ultra-cold atom systems. In chapter 6, we finally carry on the analytical study

of the simple two-well model by means of the Bogoliubov approximation showing how the energy spectrum obtained analytically well reproduces the exact spectrum determined numerically. We then summarize and conclude.

The main contents of this thesis have been published in the papers [55–57].

Chapter 1

Theoretical Framework

The theoretical framework that naturally fits the description of a mixture of two weakly interacting bosonic gases is the second-quantization formalism. The second-quantization process initially introduced by Paul Dirac in 1927 is a mathematical framework capable of describing and analyze quantum many-body systems. This formalism arises from the possibility to formulate the many-body quantum problem in terms of a many-oscillator model leading to the quantization of the many-body wavefunction Ψ in terms of normal modes. It naturally entails the preservation of the correct statistics due to the indistinguishability of quantum-particles.

Within the second-quantization approach each bosonic field is represented by a bosonic field-operator $\hat{\Psi}(\vec{x})$. The bosonic field operator satisfies the standard commutation relation of bosons

$$[\hat{\Psi}(\vec{x}),\hat{\Psi}^{\dagger}(\vec{s})] = \delta^3(\vec{x}-\vec{s}), \quad [\hat{\Psi}(\vec{x}),\hat{\Psi}(\vec{s})] = [\hat{\Psi}^{\dagger}(\vec{x}),\hat{\Psi}^{\dagger}(\vec{s})] = 0. \tag{1.1}$$

Bosonic field-operators and their conjugates, can be expanded in terms of normal modes in a given, arbitrary, basis:

$$\hat{\Psi}(\vec{x}) = \sum_i \psi_i(\vec{x}) a_i, \quad \hat{\Psi}^{\dagger}(\vec{x}) = \sum_j \psi_j(\vec{x}) a_j^{\dagger} \tag{1.2}$$

where $\{\psi_i(\vec{x})\}$ is a complete orthonormal basis of the many-body wavefunction, and a_i, $a_j^{\dagger}$ are annihilation and creation operators of modes i and j respectively. Creation

and annihilation operators a_i, $a_j^\dagger$ satisfy the commutation relations

$$[a_i, a_j^\dagger] = \delta_{ij}, \quad [a_i^\dagger, a_j^\dagger] = [a_i, a_j] = 0. \tag{1.3}$$

The choice of the basis is of course arbitrary, but peculiar choices can be particularly suitable for different physical problems. If dealing with periodic systems, e.g. optical lattices, convenient choices of the basis are the Bloch basis and the Wannier basis.

The Bloch Basis. The Bloch basis is formed by the complete orthonormal set of eigenfunction associated with the quantum mechanical problem of a particle in a periodic potential. The equation of motion describing the dynamic of the problem is described by the Schroedinger equation

$$i\hbar\Psi(x,t) = \hat{H}\Psi(x,t) \tag{1.4}$$

where $\hat{H} = -\frac{\hbar^2}{2m}\nabla^2 + V_p(\vec{x})$ is the 1-particle Hamiltonian operator and $V_p(\vec{x}) = V_p(\vec{x}+\vec{R})$ the given periodic potential of period $\vec{R} = ja_x\vec{u}_x + la_y\vec{u}_y + ma_z\vec{u}_z$, with $j,l,m \in \mathbb{Z}$ and a_x, a_y and a_z the periodicity along the x, y and z directions. Note that if $V_p(\vec{x})$ describes the periodic potential of a lattice, the index (j,l,m) identify the discrete coordinates of each lattice site. According to the *Bloch Theorem* [58] the solution of the problem (1.4) are

$$\Psi(x,t) = e^{i\frac{E_n(\vec{k})}{\hbar}t}\psi_{nk}(\vec{x}) \tag{1.5}$$

where $E_n(\vec{k})$ and $\psi_{nk}(\vec{x})$ are the eigenvalues and the eigenfunctions of the operator $\hat{H}$ respectively. Eigenfunctions $\psi_{nk}(\vec{x})$ have the form:

$$\psi_{nk}(\vec{x}) = e^{i\,\vec{k}\cdot\vec{x}}u_{nk}(\vec{x}), \tag{1.6}$$

and satisfy the property

$$\psi_{nk}(\vec{x}+\vec{R}) = e^{i\vec{k}\cdot(\vec{x}+\vec{R})}u_{nk}(\vec{x}+\vec{R}) = e^{i\vec{k}\cdot\vec{R}}u_{nk}(\vec{x}) \tag{1.7}$$

where $u_{nk}(\vec{x}+\vec{R}) = u_{nk}(\vec{x})$. The set of all the eigenfunction $\{\psi_{nk}(\vec{x})\}$ forms the complete orthonormal basis called the *Bloch basis*. It satisfy therefore the relation

$$(\psi_{mq}(\vec{x}), \psi_{nk}(\vec{x})) = \int_V d^3x\, \psi^*_{mq}(\vec{x})\psi_{nk}(\vec{x}) = \delta_{mn}\delta_{qk} \tag{1.8}$$

The bosonic field-operator expanded in the Bloch basis take the form:

$$\hat{\Psi}(\vec{x}) = \sum_{n,k} \psi_{nk}(\vec{x}) b_{nk} = \sum_{n,k} e^{i\vec{k}\cdot\vec{x}} u_{nk}(\vec{x}) b_{nk}, \tag{1.9}$$

$$\hat{\Psi}^\dagger(\vec{x}) = \sum_{n,k} \psi_{nk}(\vec{x}) b^\dagger_{nk} = \sum_{n,k} e^{i\vec{k}\cdot\vec{x}} u_{nk}(\vec{x}) b^\dagger_{nk}. \tag{1.10}$$

The Wannier Basis. In optical lattice applications is often useful to introduce another basis, namely, the Wannier Basis [58]. The Wannier modes are defined as the Fourier transform of the Bloch modes:

$$a_{ni} = \sum_k \frac{1}{\sqrt{M}} b_{nk} e^{i\vec{k}\cdot\vec{R}_i} \equiv a_{n\,jlm} = \sum_k \frac{1}{\sqrt{M}} b_{nk} e^{i(k_x a_x j + k_y a_y l + k_z a_z m)} \tag{1.11}$$

Due to the anti-transformation properties of the Fourier transform, the inverse definition also holds

$$b_{nk} = \sum_i \frac{1}{\sqrt{M}} a_{ni} e^{-i\vec{k}\cdot\vec{R}_i}. \tag{1.12}$$

By applying definition (1.12) to the expansion of (1.13), it is possible to represents the field-operator in the new basis.

$$\begin{aligned}\hat{\Psi}(\vec{x}) = \sum_{n,k} \psi_{nk}(\vec{x}) b_{nk} &= \sum_{n,k} \psi_{nk}(\vec{x}) \sum_i \frac{1}{\sqrt{M}} a_{ni} e^{-i\vec{k}\cdot\vec{R}_i} = \\ &= \sum_{n,i}\sum_k e^{i\vec{k}\cdot\vec{x}} u_{nk}(\vec{x}) \frac{1}{\sqrt{M}} e^{-i\vec{k}\cdot\vec{R}_i} a_{ni} = \\ &\sum_{n,i} \frac{1}{\sqrt{M}} \sum_k e^{i\vec{k}\cdot\vec{x}} e^{-i\vec{k}\cdot\vec{R}_i} u_{nk}(\vec{x}) a_{ni} = \sum_{n,i} W_{ni}(\vec{x}) a_{ni}\end{aligned} \tag{1.13}$$

where we define the *Wannier eigenfunctions* as:

$$W_{ni}(\vec{x}) = \frac{1}{\sqrt{M}} \sum_k e^{i\vec{k}\cdot(\vec{x}-\vec{R}_i)} u_{nk}(\vec{x}) \tag{1.14}$$

The set of $\{W_{ni}(\vec{x})\}$ form a complete orthonormal basis named as Wannier basis, and thus the $W_{ni}(\vec{x})$ satisfy the relation of orhogonality

$$(W_{mj}(\vec{x}), W_{ni}(\vec{x})) = \int_V d^3x W^*_{mj}(\vec{x}) W_{ni}(\vec{x}) = \delta_{mn}\delta_{ji} \tag{1.15}$$

Wannier $W_{ni(\vec{x})}$ describes the localization of bosons in the lattice site i. Lattice coordinates of a given site i corresponds to the lattice potential minima. If the lattice potential $V_p(\vec{x})$ in correspondence of the site $\vec{x} = \vec{R}_i$ can be approximated with an harmonic potential $V_p(\vec{x}) \approx \frac{1}{2} m\omega_p^2 (\vec{x} - \vec{R}_i)^2$ the Wannier function (1.14) can be seen as the solution of the 1-particle i^{th}-well problem (i.e. i^{th}-well Harmonic Oscillator):

$$\Big[-\frac{\hbar^2}{2m}\nabla^2 + \frac{1}{2} m\omega_p^2 (\vec{x} - \vec{R}_i)^2 \Big] W_i(\vec{x}) = E_0 W_i(\vec{x}) \tag{1.16}$$

whose solution is a gaussian-like function

$$W_i(\vec{x}) \simeq \frac{1}{\sqrt{\pi\sigma}} e^{-\frac{(\vec{x}-\vec{R}_i)^2}{2\sigma^2}} \tag{1.17}$$

where $\sigma = \sqrt{\frac{\hbar}{m\omega_p}}$. We can then observe that, from functions (1.17) it is easier to understand why Wannier functions $W_i(\vec{x})$ describe the localization of bosons in a given potential well i of the periodic lattice.

Bosonic field operator expanded in the Wannier basis are then

$$\hat{\Psi}(\vec{x}) = \sum_{n,i} W_{ni}(\vec{x}) a_{ni}, \quad \hat{\Psi}^\dagger(\vec{x}) = \sum_{n,j} W_{nj}(\vec{x}) a^\dagger_{nj}; \tag{1.18}$$

also in this case, local-mode operators a_i and $a^\dagger_j$ satisfy the standard bosonic commutation relations: $[a_{ni}, a^\dagger_{nj}] = \delta_{ij}$ and $[a^\dagger_{ni}, a^\dagger_{nj}] = [a_{ni}, a_{nj}] = 0$.

Within the second quantization formalism a many-body field expanded in a given basis, is represented by a collection of Harmonic oscillators described by the creation (annihilation) operators $a^\dagger_i$ (a_i) proper of that mode i. Let's try now to understand what is the contribution of each mode to the total field. The total number of particles

of a given field is described by the total number operator defined as:

$$\hat{N} = \int d^3x \hat{\Psi}^\dagger(\vec{x})\hat{\Psi}(\vec{x}) = \int d^3x \sum_i \sum_j \phi_i^*(\vec{x})\phi_j(\vec{x}) a_i^\dagger a_j = \sum_i \sum_j a_i^\dagger a_j \int d^3x \phi_i^*(\vec{x})\phi_j(\vec{x}) = \sum_i \sum_j a_i^\dagger a_j \delta_{ij} = \sum_i a_i^\dagger a_i = \sum_i \hat{n}_i \quad (1.19)$$

where $\hat{n}_i = a_i^\dagger a_i$ is number operator associated with the i^{th} Harmonic Oscillator (i^{th} mode). If one compute the expectation value of operator (1.19), will obtain the average number of particle in that field:

$$\langle \hat{N} \rangle = \langle \sum_i \hat{n}_i \rangle = \sum_i \langle \hat{n}_i \rangle \quad (1.20)$$

The average number of particle in a field is therefore given by the sum of the average number of particles in each mode. Each modes then contributes to the total field according to the weight associated to that mode in that representation. This weight is nothing more than the number of particle (quanta) in that given mode of oscillation.

The state of the physical system in the second-quantization formalism, can be represented by the collection of the occupation numbers of each mode (Harmonic Oscillator) that contributes to the field. This states are called Fock states and for bosonic fields are defined as tensor product of 1-body states of each harmonic oscillator in the occupation-number representation.

$$|n_1 n_2 \dots n_i \dots n_M\rangle = |n_1\rangle \otimes |n_2\rangle \otimes \cdots \otimes |n_i\rangle \otimes \cdots \otimes |n_M\rangle = \prod_{i=1}^{M} |n_i\rangle \quad (1.21)$$

where M is the dimension of the basis (e.g. the number of lattice sites in the Wannier basis). According to the definition of single-mode annihilation and creation operators their action on the Fock states (1.21) are defined as

$$a_i^\dagger |n_1 n_2 \dots n_i \dots n_M\rangle = \sqrt{n_i + 1} |n_1 n_2 \dots n_i + 1 \dots n_M\rangle, \quad (1.22)$$

$$a_i |n_1 n_2 \dots n_i \dots n_M\rangle = \sqrt{n_i} |n_1 n_2 \dots n_i - 1 \dots n_M\rangle, \quad (1.23)$$

while the action of the mode-i number operator $\hat{n}_i = a_i^\dagger a_i$ is given by

$$\begin{aligned}\hat{n}_i|n_1 n_2 \dots n_i \dots n_M\rangle = a_i^\dagger a_i |n_1 n_2 \dots n_i \dots n_M\rangle = \\ = \sqrt{n_i} a_i^\dagger |n_1 n_2 \dots n_i - 1 \dots n_M\rangle = \\ = \sqrt{n_i}\sqrt{n_i - 1 + 1}|n_1 n_2 \dots n_i + 1 \dots n_M\rangle = \\ = \sqrt{n_i}\sqrt{n_i}|n_1 n_2 \dots n_i + 1 \dots n_M\rangle = n_i |n_1 n_2 \dots n_i \dots n_M\rangle \quad (1.24)\end{aligned}$$

The action of $\hat{n}_i$ over the Fock state extracts the number of particles in mode i. For bosonic mode-operators (and bosonic field-operators) the allowed number of particle of each mode belong to the range $n_i \in [0, \infty)$.

Mixture of bosonic species . If one is willing to describe the behaviour of different bosonic species in a system, e.g. a mixture of two-quantum gases, he will need to take into account different bosonic field-operators, each one describing a different bosonic field.

To study a mixture of *two* bosonic species we need to define two different bosonic field-operators: $\hat{\Psi}_a(\vec{x})$ for species A and $\hat{\Psi}_b(\vec{x})$ for species B. The two field-operators are defined over different Fock spaces $\mathscr{H}_A$ and $\mathscr{H}_B$

$$\hat{\Psi}_a : \mathscr{H}_A \longrightarrow \mathscr{H}_A, \quad \hat{\Psi}_b : \mathscr{H}_B \longrightarrow \mathscr{H}_B. \quad (1.25)$$

Since the two field operators are defined over different Fock spaces, and $\mathscr{H}_A \cap \mathscr{H}_B = 0$ the two field-operator commutes

$$[\hat{\Psi}_a(\vec{x}), \hat{\Psi}_b(\vec{x})] = 0, \quad [\hat{\Psi}_a^\dagger(\vec{x}), \hat{\Psi}_b^\dagger(\vec{x})] = 0, \quad (1.26)$$

$$[\hat{\Psi}_a^\dagger(\vec{x}), \hat{\Psi}_b(\vec{x})] = 0, \quad [\hat{\Psi}_a(\vec{x}), \hat{\Psi}_b^\dagger(\vec{x})] = 0. \quad (1.27)$$

The two field-operator can be represented in a given basis. The choice, as always, is arbitrary and depends on the particular problem one is dealing with. However, it is usually convenient expand both field operators in the same basis.

$$\hat{\Psi}_a(\vec{x}) = \sum_i \psi_i(\vec{x}) a_i, \quad \hat{\Psi}_b(\vec{x}) = \sum_j \psi_j(\vec{x}) b_j; \quad (1.28)$$

$$\hat{\Psi}_a^\dagger(\vec{x}) = \sum_i \psi_i^*(\vec{x}) a_i^\dagger, \quad \hat{\Psi}_b^\dagger(\vec{x}) = \sum_j \psi_j^*(\vec{x}) b_j^\dagger; \quad (1.29)$$

where a_i ($a_i^\dagger$) and b_j ($b_j^\dagger$) are the single-mode annihilation (creation) operators of species A and B respectively. Note that, also the single-mode operators of two different species commutes

$$[a_i, b_j] = 0, \quad [a_i^\dagger, b_j^\dagger] = 0; \tag{1.30}$$

$$[a_i^\dagger, b_j] = 0, \quad [a_i, b_j^\dagger] = 0. \tag{1.31}$$

Once the representation basis as been fixed, it is possible to define the Fock states of the system in terms of occupation numbers. The Fock state of species A is defined as

$$|n_{a1} n_{a2} \dots n_{ai} \dots n_{aM}\rangle = |n_{a1}\rangle \otimes |n_{a2}\rangle \otimes \dots \otimes |n_{ai}\rangle \otimes \dots \otimes |n_{aM}\rangle = \prod_{i=1}^{M} |n_{ai}\rangle, \tag{1.32}$$

while the Fock state representing the state of species B is

$$|n_{b1} n_{b2} \dots n_{bj} \dots n_{bM}\rangle = |n_{b1}\rangle \otimes |n_{b2}\rangle \otimes \dots \otimes |n_{bj}\rangle \otimes \dots \otimes |n_{bM}\rangle = \prod_{j=1}^{M} |n_{bj}\rangle \tag{1.33}$$

The total Fock space $\mathscr{H}_T$ including all the possible states of a mixture of two bosonic species is then defined as the direct product of the single species Fock spaces.

$$\mathscr{H}_T = \mathscr{H}_A \otimes \mathscr{H}_B \tag{1.34}$$

While the total Fock state representing the quantum state of the entire mixture is defined as the direct product of the single species Fock states

$$|\vec{n}_a, \vec{n}_b\rangle = |n_{a1} n_{a2} \dots n_{ai} \dots n_{aM}\rangle \otimes |n_{b1} n_{b2} \dots n_{bj} \dots n_{bM}\rangle. \tag{1.35}$$

1.1 The Second-Quantization Hamiltonian

Within the second-quantization approach the second-quantization Hamiltonian that describes the dynamic of the many-body system take the form:

$$\hat{\mathscr{H}} = \int d^3x \hat{\Psi}^\dagger(\vec{x}) \hat{H} \hat{\Psi}(\vec{x}), \tag{1.36}$$

where $\hat{\Psi}^\dagger(\vec{x})$ and $\hat{\Psi}(\vec{x})$ are the field-operator and its hermitian conjugate defined above, and $\hat{H}$ the 1-particle Hamiltonian Operator describing the system.

The equation of motion are then obtained within the Heisenberg picture by applying the commutator brackets to the Hamiltonian operator (1.36) and the canonical field-operators $\hat{\Psi}^\dagger(\vec{x},t)$ and $\hat{\Psi}(\vec{x},t)$.

$$i\hbar\partial_t\hat{\Psi}(\vec{x},t) = [\hat{\Psi}(\vec{x},t),\hat{\mathscr{H}}], \quad i\hbar\partial_t\hat{\Psi}^\dagger(\vec{x},t) = [\hat{\Psi}^\dagger(\vec{x},t),\hat{\mathscr{H}}] \tag{1.37}$$

that, by expanding $\hat{\Psi}(\vec{x},t) = \sum_i \psi_i(\vec{x})a_i$ in terms on modes, read

$$i\hbar\partial_t a_i = [a_i,\hat{\mathscr{H}}], \quad i\hbar\partial_t a_j^\dagger = [a_j^\dagger,\hat{\mathscr{H}}] \tag{1.38}$$

1.1.1 The non-interacing Bose-Gas Hamiltonian

The Hamiltonian Operator of a free non-interacting Bose-Gas is defined, according to (1.36), as

$$\hat{\mathscr{H}} = \int d^3x\hat{\Psi}^\dagger(\vec{x})\hat{H}\hat{\Psi}(\vec{x}) = \int d^3x\hat{\Psi}^\dagger(\vec{x})\Big[-\frac{\hbar^2}{2m}\nabla^2 + V(\vec{x})\Big]\hat{\Psi}(\vec{x}) \tag{1.39}$$

where $\hat{H} = -\frac{\hbar^2}{2m}\nabla^2 + V(\vec{x})$ is the 1-particle Hamiltonian operator describing a single quantum-particle in a potential $V(\vec{x})$. Expanding the field-operator in a given basis, the hamiltonian can be rewritten in terms of annihilation and creation operators of the basis'modes.

$$\begin{aligned}
\hat{\mathscr{H}} = \int d^3x\hat{\Psi}^\dagger(\vec{x})\Big[-\frac{\hbar^2}{2m}\nabla^2 + V(\vec{x})\Big]\hat{\Psi}(\vec{x}) = \\
= \int d^3x\sum_i \phi_i^*(\vec{x})a_i^\dagger\Big[-\frac{\hbar^2}{2m}\nabla^2 + V(\vec{x})\Big]\sum_j \phi_j(\vec{x})a_j = \\
= \sum_i\sum_j\Big(\int d^3x\phi_i^*(\vec{x})\Big[-\frac{\hbar^2}{2m}\nabla^2 + V(\vec{x})\Big]\phi_j(\vec{x})\Big)a_i^\dagger a_j = \\
= \sum_i\sum_j\Big(-\frac{\hbar^2}{2m}\int d^3x\phi_i^*(\vec{x})\nabla^2\phi_j(\vec{x}) + \int d^3x\phi_i^*(\vec{x})V(\vec{x})\phi_j(\vec{x})\Big)a_i^\dagger a_j = \\
= \sum_i\sum_j(E_{ij}+V_{ij})a_i^\dagger a_j = \sum_i\sum_j H_{ij}a_i^\dagger a_j
\end{aligned} \tag{1.40}$$

Where $H_{ij} = E_{ij} + V_{ij}$ are the matrix element of the first-quantization hamiltonian $\hat{H}$ in the representation $\{\phi_i(\vec{x})\}$, and $E_{ij} = -\frac{\hbar^2}{2m}\int d^3x\,\phi_i^*(\vec{x})\nabla^2\phi_j(\vec{x})$ and $V_{ij} = \int d^3x\,\phi_i^*(\vec{x})V(\vec{x})\phi_j(\vec{x})$ the kinetic and potential energy parts respectively. The most convenient choice of the basis strongly depends on the shape of the potential and corresponds to the one in which $\hat{H}$ is in its diagonal form. This happens if the set $\{\phi_i(\vec{x})\}$ are the eigenfunction of $\hat{H}$. In that case the hamiltonian reduces to:

$$\begin{aligned}\hat{\mathscr{H}} = \int d^3x\hat{\Psi}^\dagger(\vec{x})\hat{H}\hat{\Psi}(\vec{x}) = \\ = \int d^3x\sum_i \phi_i^*(\vec{x})a_i^\dagger \hat{H}\sum_j \phi_j(\vec{x})a_j = \\ = \sum_i\sum_j H_{ij}\int d^3x\phi_i^*(\vec{x})\phi_j(\vec{x})a_i^\dagger a_j = \\ = \sum_i\sum_j H_{ij}\delta_{ij}a_i^\dagger a_j = \sum_i H_{ii}a_i^\dagger a_i = \sum_i E_i a_i^\dagger a_i = \sum_i E_i\hat{n}_i\end{aligned} \tag{1.41}$$

The hamiltonian is now written in terms of mode-number operators $\hat{n}_i$, so the associated eigenvalue problem has a trivial solution

$$\hat{\mathscr{H}}|\vec{n}\rangle = E|\vec{n}\rangle \tag{1.42}$$

$$\hat{\mathscr{H}}|\vec{n}\rangle = \sum_i E_i\hat{n}_i|\vec{n}\rangle = \sum_i E_i n_i|\vec{n}\rangle \tag{1.43}$$

so the energy eigenvalues of the system are $E = \sum_i E_i n_i$ and the eigenstates are the Fock states themeselves.

Unfortunately, obtaining the diagonal form of $\hat{H}$ is in general far from trivial.

1.1.2 The weakly-interacting Bose-Gas Hamiltonian

The Hamiltonian of a weakly interacting Bose-Gas is obtained by adding an intra-species interaction term to the hamiltonian (1.39).

$$\hat{\mathscr{H}} = \int d^3x\hat{\Psi}^\dagger(\vec{x})\Big[-\frac{\hbar^2}{2m}\nabla^2 + V(\vec{x}) + U(\vec{x})\Big]\hat{\Psi}(\vec{x}) \tag{1.44}$$

where the term $U(\vec{x})$ describes the *intra-species* interaction between the particles inside the Bose-Gas. It ìs a self-interaction term that takes into account the interactions of the quantum-field with itself. $U(\vec{x})$ is defined as a two-body interaction term of the form

$$U(\vec{x}) = \frac{1}{2}\int d^3y \hat{\Psi}^\dagger(\vec{y})U(|\vec{x}-\vec{y}|)\hat{\Psi}(\vec{y}) \tag{1.45}$$

By substituting in (1.44) the term (1.45) one gets:

$$\begin{aligned}\hat{\mathscr{H}} = \int d^3x \hat{\Psi}^\dagger(\vec{x})\Big[-\frac{\hbar^2}{2m}\nabla^2 + V(\vec{x})\Big]\hat{\Psi}(\vec{x}) + \\ + \frac{1}{2}\int\int d^3x d^3y \hat{\Psi}^\dagger(\vec{x})\hat{\Psi}^\dagger(\vec{y})U(|\vec{x}-\vec{y}|)\hat{\Psi}(\vec{y})\hat{\Psi}(\vec{x})\end{aligned} \tag{1.46}$$

In general in literature, Hamiltonian (1.44) is written directly in the form (1.46) as

$$\hat{\mathscr{H}} = \hat{\mathscr{H}_0} + \hat{\mathscr{U}} \tag{1.47}$$

where

$$\hat{\mathscr{H}_0} = \int d^3x \hat{\Psi}^\dagger(\vec{x})\Big[-\frac{\hbar^2}{2m}\nabla^2 + V(\vec{x})\Big]\hat{\Psi}(\vec{x}), \tag{1.48}$$

and

$$\hat{\mathscr{U}} = \frac{1}{2}\int\int d^3x d^3y \hat{\Psi}^\dagger(\vec{x})\hat{\Psi}^\dagger(\vec{y})U(|\vec{x}-\vec{y}|)\hat{\Psi}(\vec{y})\hat{\Psi}(\vec{x}). \tag{1.49}$$

This is done in order to visibly separate the one-body part $\hat{\mathscr{H}_0}$, depending only on the field operator $\hat{\Psi}(\vec{x})$ defined in $\vec{x}$, from the two-body interaction term $\hat{\mathscr{U}}$, depending on both the fields $\hat{\Psi}(\vec{x})$ and $\hat{\Psi}(\vec{y})$ defined at the coordinates $\vec{x}$ and $\vec{y}$ respectively. From the relation (1.49) is indeed clear the two-body character of this interaction: the field $\hat{\Psi}(\vec{x})$ interacts with the field $\hat{\Psi}(\vec{y})$ at distance $|\vec{x}-\vec{y}|$ through the potential $U(|\vec{x}-\vec{y}|)$.

For weakling interacting and dilute Bose-Gases the two-body interaction potential $U(|\vec{x}-\vec{y}|)$, can be defined as the contact potential

$$U(|\vec{x}-\vec{y}|) = U_0\delta^3(\vec{x}-\vec{y}) \tag{1.50}$$

where

$$U_0 = \frac{4\pi\hbar^2 a_0}{m} \tag{1.51}$$

with a_0 the s-wave scattering length of the scattering process between two-particles of the quantum gas. This assumption is valid only under the hypothesis of ultra-cold

and dilute gas, where the interparticle distance d is very large and due to the low temperature, the particles can be assumed relatively slow (momentum p such that $\frac{pr_0}{\hbar} \ll 1$, with r_0 the range of interatomic forces).
Under this assumptions it is possible to rewrite the 2-body interaction term of $\hat{\mathscr{H}}$ as

$$\begin{aligned}\hat{\mathscr{U}} &= \frac{U_0}{2}\int\int d^3x\, d^3y \hat{\Psi}^\dagger(\vec{x})\hat{\Psi}^\dagger(\vec{y})\delta^3(\vec{x}-\vec{y})\hat{\Psi}(\vec{y})\hat{\Psi}(\vec{x}) = \\ &= \frac{U_0}{2}\int d^3x\ \hat{\Psi}^\dagger(\vec{x})\hat{\Psi}^\dagger(\vec{x})\hat{\Psi}(\vec{x})\hat{\Psi}(\vec{x}) = \frac{U_0}{2}\int d^3x\ (\hat{\Psi}^\dagger(\vec{x}))^2(\hat{\Psi}(\vec{x}))^2 \quad (1.52)\end{aligned}$$

By substituting the new form of $\hat{\mathscr{U}}$ in the Hamiltonian (1.47), one obtains the new expression for the weakly-interacting Bose-Gas Hamiltonian

$$\hat{\mathscr{H}} = \int d^3x \hat{\Psi}^\dagger(\vec{x})\Big[-\frac{\hbar^2}{2m}\nabla^2 + V(\vec{x})\Big]\hat{\Psi}(\vec{x}) + \frac{U_0}{2}\int d^3x\ (\hat{\Psi}^\dagger(\vec{x}))^2(\hat{\Psi}(\vec{x}))^2. \quad (1.53)$$

1.1.3 Mixture of two weakly-interacting Bose-Gases Hamiltonian

The Second-Quantization Hamiltonian describing a mixture of two weakling interacting Bose-Gases trapped in a given potential $V(\vec{x})$ is defined as the sum of the Hamiltonian of the two separate Bose gases (1.53) plus an extra 2-body interaction term describing the *inter-species* interaction between the two different bosonic fields.

$$\hat{\mathscr{H}} = \hat{\mathscr{H}}_{0a} + \hat{\mathscr{U}}_a + \hat{\mathscr{H}}_{0b} + \hat{\mathscr{U}}_b + \hat{\mathscr{W}}, \quad (1.54)$$

where

$$\begin{aligned}\hat{\mathscr{H}}_{0a} &= \int d^3x \hat{\Psi}_a^\dagger(\vec{x})\Big[-\frac{\hbar^2}{2m}\nabla^2 + V(\vec{x})\Big]\hat{\Psi}_a(\vec{x}), & (1.55)\\ \hat{\mathscr{U}}_a &= \frac{U_a}{2}\int d^3x\ (\hat{\Psi}_a^\dagger(\vec{x}))^2(\hat{\Psi}_a(\vec{x}))^2, & (1.56)\\ \hat{\mathscr{H}}_{0b} &= \int d^3x \hat{\Psi}_b^\dagger(\vec{x})\Big[-\frac{\hbar^2}{2m}\nabla^2 + V(\vec{x})\Big]\hat{\Psi}_b(\vec{x}), & (1.57)\\ \hat{\mathscr{U}}_b &= \frac{U_b}{2}\int d^3x\ (\hat{\Psi}_b^\dagger(\vec{x}))^2(\hat{\Psi}_b(\vec{x}))^2, & (1.58)\\ \hat{\mathscr{W}} &= \int\int d^3x\, d^3y \hat{\Psi}_a^\dagger(\vec{x})\hat{\Psi}_b^\dagger(\vec{y})W(|\vec{x}-\vec{y}|)\hat{\Psi}_b(\vec{y})\hat{\Psi}_a(\vec{x}). & (1.59)\end{aligned}$$

Here $\hat{\mathscr{H}}_{0a} + \hat{\mathscr{U}}_a$ and $\hat{\mathscr{H}}_{0b} + \hat{\mathscr{U}}_b$ are the two separate Hamiltonians of the the two Bose-Gases written in terms of field operators $\hat{\Psi}_a(\vec{x})$ and $\hat{\Psi}_b(\vec{x})$ for species A and B respectively. While $\hat{\mathscr{W}}$ is the two-body inter-species interaction term describing the interaction between the bosonic field $\hat{\Psi}_a(\vec{x})$ of species A and the bosonic field $\hat{\Psi}_b(\vec{y})$ of species B. The inter-species interaction between the bosonic field-operator $\hat{\Psi}_a(\vec{x})$ at coordinate $\vec{x}$, and the bosonic field-operator $\hat{\Psi}_b(\vec{y})$ at coordinate $\vec{y}$, is described by the potential $W(|\vec{x}-\vec{y}|)$ and depends on the relative distance $|\vec{x}-\vec{y}|$ between the particles of two species.

In an analogous way of what has been done for the *intra-species* interaction term $\hat{\mathscr{U}}$ for the single bosonic gas, it is possible to rewrite the *inter-species* interaction term $\hat{\mathscr{W}}$ in a much simpler form. For sufficiently low-temperatures and dilute gases hypothesis, the interaction between the two species can be very-well described by a scattering process in the s-wave channel. This can be done if the mean inter-species distance is large enough $d_{ab} \gg r_{ab}$, and if the mean momenta p_c of particles of both species $c = a, b$ is small enough such that the condition $\frac{p_c r_{ab}}{\hbar} \ll 1$ is satisfied. Here r_{ab} states for the range of atomic forces between the species A and B. Under this assumptions the inter-species potential $W(|\vec{x}-\vec{y}|)$ can be rewritten as

$$W(|\vec{x}-\vec{y}|) = U_{ab}\delta^3(\vec{x}-\vec{y}), \tag{1.60}$$

where

$$U_{ab} = \frac{4\pi\hbar^2 a_{ab}}{m_{ab}}. \tag{1.61}$$

with m_{ab} the reduced mass and a_{ab} the s-wave scattering length of the A-B scattering process.
By substituting the new $W(|\vec{x}-\vec{y}|)$ in (1.59) we get the new expression for $\hat{\mathscr{W}}$:

$$\begin{aligned}\hat{\mathscr{W}} = U_{ab}\int\int d^3x\, d^3y \hat{\Psi}_a^\dagger(\vec{x})\hat{\Psi}_b^\dagger(\vec{y})\delta^3(\vec{x}-\vec{y})\hat{\Psi}_b(\vec{y})\hat{\Psi}_a(\vec{x}) = \\ = U_{ab}\int d^3x \hat{\Psi}_a^\dagger(\vec{x})\hat{\Psi}_b^\dagger(\vec{x})\hat{\Psi}_b(\vec{x})\hat{\Psi}_a(\vec{x})\end{aligned} \tag{1.62}$$

Since $\hat{\Psi}_a(\vec{x})$ and $\hat{\Psi}_b(\vec{x})$ commutes, inter-species term can be rewritten in the more usual form as a density-density operator:

$$\hat{\mathscr{W}} = U_{ab}\int d^3x \hat{\Psi}_a^\dagger(\vec{x})\hat{\Psi}_a(\vec{x})\hat{\Psi}_b^\dagger(\vec{x})\hat{\Psi}_b(\vec{x}) \tag{1.63}$$

The Hamiltonian of two-weakly interacting Bose-Gases takes finally the form:

$$\begin{aligned}\hat{\mathscr{H}} = \int d^3x \hat{\Psi}_a^\dagger(\vec{x}) \Big[-\frac{\hbar^2}{2m}\nabla^2 + V(\vec{x}) \Big] \hat{\Psi}_a(\vec{x}) + \\ + \int d^3x \hat{\Psi}_b^\dagger(\vec{x}) \Big[-\frac{\hbar^2}{2m}\nabla^2 + V(\vec{x}) \Big] \hat{\Psi}_b(\vec{x}) + \\ + \frac{U_a}{2} \int d^3x \, (\hat{\Psi}_a^\dagger(\vec{x}))^2 (\hat{\Psi}_a(\vec{x}))^2 + \\ + \frac{U_b}{2} \int d^3x \, (\hat{\Psi}_b^\dagger(\vec{x}))^2 (\hat{\Psi}_b(\vec{x}))^2 + \\ + U_{ab} \int d^3x \hat{\Psi}_a^\dagger(\vec{x}) \hat{\Psi}_a(\vec{x}) \hat{\Psi}_b^\dagger(\vec{x}) \hat{\Psi}_b(\vec{x}) \end{aligned} \quad (1.64)$$

1.2 The Bose-Hubbard Model

The Bose-Hubbard Model describes a weakly-interacting Bose-Gas trapped in a periodic potential [59]-[63]. It is particularly useful to describe quantum lattice-systems as ultracold atoms trapped in an optical lattice [58]. The model is described by the second-quantization hamiltonian written in the Wannier-modes representation

$$\hat{\mathscr{H}} = -t \sum_{\langle i,j \rangle} a_i^\dagger a_j + \frac{U}{2} \sum_i \hat{n}_i \big(\hat{n}_i - 1 \big) \quad (1.65)$$

where t is the hopping amplitude, and U the inter-species interaction, while the symbol $\langle i, j \rangle$ denotes the sum over the nearest neighboring sites. Single-mode operator $a_i^\dagger$ and a_j are the creation and annihilation operator in the Wannier-modes picture and satisfies the standard bosonic commutation relations $[a_i, a_j^\dagger] = \delta_{ij}$. While $\hat{n}_i = a_i^\dagger a_i$ is the mode-i number operator.

1.2.1 Derivation of the Bose-Hubbard Hamiltonian

The Bose-Hubbard Hamiltonian can be derived from the Hamiltonian of a weakly interacting Bose-Gas (1.53) assuming the potential $V(\vec{x})$ to be periodic. Let's take Hamiltonian of the weakly-interacting Bose-Gas

$$\hat{\mathscr{H}} = \hat{\mathscr{H}_0} + \hat{\mathscr{U}}, \quad (1.66)$$

$$\hat{\mathscr{H}_0} = \int d^3x \hat{\Psi}^\dagger(\vec{x}) \Big[-\frac{\hbar^2}{2m}\nabla^2 + V(\vec{x}) \Big] \hat{\Psi}(\vec{x}), \tag{1.67}$$

$$\hat{\mathscr{U}} = \frac{U}{2} \int d^3x \, (\hat{\Psi}^\dagger(\vec{x}))^2 (\hat{\Psi}(\vec{x}))^2, \tag{1.68}$$

$$\tag{1.69}$$

and set the potential $V(\vec{x})$ such that

$$V(\vec{x}) = V_0 \cos^2(\vec{K}_p \cdot \vec{x}) \tag{1.70}$$

where $\vec{K}_p = K_x\vec{u}_x + K_y\vec{u}_y + K_z\vec{u}_z = \frac{\pi}{a_x}\vec{u}_x + \frac{\pi}{a_y}\vec{u}_y + \frac{\pi}{a_z}\vec{u}_z$ is the wave-vector of the lattice embedding its periodicity. While a_x, a_y and a_z are the lattice steps along the three directions. For two-dimensional optical lattice the potential $V(\vec{x}) = V_0 e^{-\sigma z^2} \cos^2(\vec{K}_{2D} \cdot \vec{x})$ with $K_{2D} = \frac{\pi}{a_x}\vec{u}_x + \frac{\pi}{a_y}\vec{u}_y$. The gaussian along the z direction forces the confinement in that direction.

Here, we derive the Bose-Hubbard Hamiltonian for the most general case of a 3D lattice, the generalization to lower dimensions is straightforward by simply applying different lattice potentials. The Bose-Hubbard Hamiltonian is obtained by expanding the bosonic field-operator in the Wannier basis. We develop the derivation in two steps, we first analyze the Kinetic term $\hat{\mathscr{H}_0}$ (1.68) and then the two-body intra-species interaction term $\hat{\mathscr{U}}$ (1.68).

Derivation of $\hat{\mathscr{H}_0}$. Since the potential is periodic, it is natural to expand the field operator in the Bloch basis and then use the transformations (1.11) and (1.12) to obtain its representation in the Wannier basis.

$$\hat{\Psi}(\vec{x}) = \sum_{n,\vec{k}} \phi_{nk}(\vec{x}) b_k = \sum_{n,\vec{k}} e^{i\vec{k}\cdot\vec{x}} u_{nk}(\vec{x}) b_{nk} \tag{1.71}$$

Substituting (1.71) in $\hat{\mathscr{H}_0}$:

$$\begin{aligned}
\hat{\mathscr{H}_0} &= \int d^3x \sum_{n,\vec{k}} e^{-i\vec{k}\cdot\vec{x}} u^*_{nk}(\vec{x}) b^\dagger_{nk} \Big[-\frac{\hbar^2}{2m}\nabla^2 + V(\vec{x}) \Big] \sum_{m,\vec{q}} e^{i\vec{q}\cdot\vec{x}} u_{mq}(\vec{x}) b_{mq} \\
&= \sum_{n,\vec{k}} \sum_{m,\vec{q}} b^\dagger_{nk} b_{mq} \int d^3x e^{-i\vec{k}\cdot\vec{x}} u^*_{nk}(\vec{x}) \Big[-\frac{\hbar^2}{2m}\nabla^2 + V(\vec{x}) \Big] e^{i\vec{q}\cdot\vec{x}} u_{mq}(\vec{x}) \\
&= \sum_{n,\vec{k}} \sum_{m,\vec{q}} \varepsilon_n(k) \delta_{mn} \delta_{kq} b^\dagger_{nk} b_{mq} = \sum_{n,\vec{k}} \varepsilon_n(k) b^\dagger_{nk} b_{nk}
\end{aligned} \tag{1.72}$$

where $\varepsilon_n(k)$ are the Bloch eigenvalues derived explicitly from the Bloch Theorem. If the single particle states are extremely localized in space, then the expression for the Bloch eigenvalues reduces to

$$\varepsilon_n(k) = 2\varepsilon_n \sum_{r\in x,y,z} [1-\cos(a_r k_r)] \tag{1.73}$$

where a_r is the period of the lattice in direction $r = x,y,z$. By applying the transformations (1.11) and (1.12) is now possible to swap from the Bloch basis to the Wannier basis representation

$$b_{nk} = \sum_i \frac{1}{\sqrt{M}} a_{ni} e^{-i\vec{k}\cdot\vec{R}_i}. \tag{1.74}$$

The final form of Hamiltonian $\hat{\mathscr{H}_0}$ is then obtained by substituting expression (1.74) in (1.72) after a number of mathematical passages (see Appendix A for the detailed calculation):

$$\hat{\mathscr{H}_0} = 6\sum_n \varepsilon_n \sum_i \hat{n}_{ni} - \sum_n \varepsilon_n \sum_{\langle i,j\rangle} a^\dagger_{ni} a_{nj}. \tag{1.75}$$

Derivation of $\hat{\mathscr{U}}$. Lets now move to derivate the two-body interspecies interaction term (1.68). To do so we expand the field operator in the Wannier basis

$$\begin{aligned}\hat{\mathscr{U}} &= \frac{U}{2}\int d^3x (\hat{\Psi}^\dagger(\vec{x}))^2 (\hat{\Psi}(\vec{x}))^2 = \\ &= \frac{U}{2}\sum_{ni}\sum_{mj}\sum_{lr}\sum_{gs}\int d^3x W^*_{ni}(\vec{x}) W^*_{mj}(\vec{x}) W_{lr}(\vec{x}) W_{gs}(\vec{x}) a^\dagger_{ni} a^\dagger_{mj} a_{lr} a_{gs}\end{aligned} \tag{1.76}$$

Since Wannier functions $W_{pc}(\vec{x})$s are orthogonals among each other, the integral $\int d^3x W^*_{ni}(\vec{x}) W^*_{mj}(\vec{x}) W_{lr}(\vec{x}) W_{gs}(\vec{x}) = \delta_{ijrs}\delta_{mnlg}$.

$$\hat{\mathscr{U}} \quad = \quad \frac{U}{2}\sum_{ni}\sum_{mj}\sum_{lr}\sum_{gs}\delta_{ijrs}\delta_{mnlg} a^\dagger_{ni} a^\dagger_{mj} a_{lr} a_{gs} \quad = \quad \frac{U}{2}\sum_{ni} a^\dagger_{ni} a^\dagger_{ni} a_{ni} a_{ni} \tag{1.77}$$

By exploiting the bosonic commutation relation $[a_{ni}, a_{ni}^\dagger] = 1$:

$$\hat{\mathscr{U}} = \frac{U}{2}\sum_{ni} a_{ni}^\dagger a_{ni}^\dagger a_{ni} a_{ni} = \\ = \frac{U}{2}\sum_{ni} a_{ni}^\dagger (a_{ni} a_{ni}^\dagger - 1) a_{ni} = \frac{U}{2}\sum_{ni} (a_{ni}^\dagger a_{ni} a_{ni}^\dagger a_{ni} - a_{ni}^\dagger a_{ni}) = \\ = \frac{U}{2}\sum_{ni} (\hat{n}_{ni}\hat{n}_{ni} - \hat{n}_{ni}) = \frac{U}{2}\sum_{ni} \hat{n}_{ni}(\hat{n}_{ni} - 1). \quad (1.78)$$

Putting together the $\hat{\mathscr{H}}_0$ and $\hat{\mathscr{U}}$ terms one derive the final form of the Hamiltonian $\hat{\mathscr{H}}$:

$$\hat{\mathscr{H}} = 6\sum_n \varepsilon_n \sum_i \hat{n}_{ni} - \sum_n \varepsilon_n \sum_{\langle i,j \rangle} a_{ni}^\dagger a_{nj} + \frac{U}{2}\sum_n \sum_i \hat{n}_{ni}(\hat{n}_{ni} - 1). \quad (1.79)$$

In a good approximation, at low enough temperatures, only the lowest energy band ε_0 contributes. In this limit by dropping terms at $n > 0$ we get the single-band Hamiltonian of the Bose-Hubbard model

$$\hat{\mathscr{H}} = 6\varepsilon_0 \hat{N} - \varepsilon_0 \sum_{\langle i,j \rangle} a_i^\dagger a_j + \frac{U}{2}\sum_i \hat{n}_i(\hat{n}_i - 1), \quad (1.80)$$

where $\hat{N} = \sum_i \hat{n}_{ni}$ is the total boson number operator. Now, by renaming $\varepsilon_0 = t$ and dropping the term $6\varepsilon_0 \hat{N}$ as $\hat{N}$ is a constant of motion, we obtain the usual form of the Bose-Hubbard Hamiltonian (1.65) introduced above:

$$\hat{\mathscr{H}} = -t \sum_{\langle i,j \rangle} a_i^\dagger a_j + \frac{U}{2}\sum_i \hat{n}_i(\hat{n}_i - 1). \quad (1.81)$$

1.3 The Two-Species Bose-Hubbard Model

The best theoretical model that describe a mixtures of two, weakly-interacting, Bose-Gases trapped in an optical lattice is the Two-Species Bose-Hubbard model. The Hamiltonian of this model is derived from the Hamiltonian of a mixture of two weakly-interacting Bose-Gases (1.64) by expanding the two bosonic field-operator $\hat{\Psi}_a(\vec{x})$ and $\hat{\Psi}_b(\vec{x})$ in the Wannier basis. The Two-Species Bose-Hubbard Hamiltonian

has the form

$$\hat{\mathscr{H}} = -t_a \sum_{\langle i,j \rangle} a_i^\dagger a_j + \frac{U_a}{2} \sum_i \hat{n}_{ai}(\hat{n}_{ai} - 1) + \\ - t_b \sum_{\langle i,j \rangle} b_i^\dagger b_j + \frac{U_b}{2} \sum_i \hat{n}_{bi}(\hat{n}_{bi} - 1) + U_{ab} \sum_i \hat{n}_{ai}\hat{n}_{bi} \quad (1.82)$$

where t_a (t_b) is the hopping amplitudes of species A (B), U_a (U_b) the intra-species interaction of species A (B) and U_{ab} is the inter-species interaction between the bosons of the two species. Single-mode operator $a_i^\dagger$ and a_j ($b_i^\dagger$ and b_j) are the creation and annihilation operators in the Wannier-modes picture of species A (B). They satisfy the standard bosonic commutation relations $[a_i, a_j^\dagger] = \delta_{ij}$ ($[b_i, b_j^\dagger] = \delta_{ij}$). While $\hat{n}_{ai} = a_i^\dagger a_i$ ($\hat{n}_{bi} = b_i^\dagger b_i$) is the mode-$i$ number operator of species A (B).

The derivation of Hamiltonian (1.82) is obtained by the expansion of the field operators of the two-species Hamiltonian (1.64) in the Wannier spatial-mode basis. This derivation is straightforward with respect to the one of the single-species Bose-Hubbard model (1.65) and is presented in details in the Appendix B. Hamiltonian (1.82) is essentially composed by the two single-species Bose-Hubbard Hamiltonians of species A and B respectively plus the inter-species interacting term $U_{ab}\sum_i \hat{n}_{ai}\hat{n}_{bi}$. This term describes the onsite interaction between the two bosonic fields and it is derived from the two-body interaction term $\hat{\mathscr{W}}$ of the two weakly-interacting Bose-Gases Hamiltonian (see Appendix B for details).

In this thesis, and often in literature when working within the Grand-Canonical ensamble formulation of quantum-statistical mechanics, it is useful to work with *Free-Energy* operator instead of the Hamiltonian operator. The free-energy is defined as

$$\hat{\mathscr{F}} = \hat{\mathscr{H}} - \sum_c \sum_i \mu_{ci}\hat{n}_{ci} \quad (1.83)$$

where the sum over c runs over all the species present in the model and μ_{ci} is the local-chemical potential of species C ($C = A, B$ in our case).

Unless otherwise noted, since in this thesis we actually work almost-only with the free-energy operator, following a very common practice in literature, we will refer to $\hat{\mathscr{H}}$ as the free-energy of our system (instead of calling it $\hat{\mathscr{F}}$). The Two-Species

Bose-Hubbard Free-energy/Hamiltonian takes therefore the form:

$$\hat{\mathscr{H}} = \frac{U_a}{2}\sum_i \hat{n_{ai}}(\hat{n_{ai}}-1) - t_a \sum_{\langle i,j\rangle} a_i^\dagger a_j - \sum_i \mu_{ai}\hat{n}_{ai} + \\ + \frac{U_b}{2}\sum_i \hat{n_{bi}}(\hat{n_{bi}}-1) - t_b \sum_{\langle i,j\rangle} b_i^\dagger b_j - \sum_i \mu_{bi}\hat{n}_{bi} + U_{ab}\sum_i \hat{n}_{ai}\hat{n}_{bi} \quad (1.84)$$

where μ_{ai} and μ_{bi} are the chemical potential of species A and B respectively.

1.4 The Twin-Species Model

The Twin-Species Model is that symmetrical case of the Two-Species Bose-Hubbard Model in which the two bosonic components features the same value of the hopping amplitude, intra-species interaction and chemical potential.

$$t_a = t_b = t \quad (1.85)$$
$$U_a = U_b = U \quad (1.86)$$
$$\mu_{ai} = \mu_{bi} = \mu_i \quad (1.87)$$

Under these constraints the Hamiltonian of the model becomes:

$$\hat{\mathscr{H}} = \frac{U}{2}\sum_i \hat{n_{ai}}(\hat{n_{ai}}-1) - t \sum_{\langle i,j\rangle} a_i^\dagger a_j - \sum_i \mu_i\hat{n}_{ai} + \\ + \frac{U}{2}\sum_i \hat{n_{bi}}(\hat{n_{bi}}-1) - t \sum_{\langle i,j\rangle} b_i^\dagger b_j - \sum_i \mu_i\hat{n}_{bi} + U_{ab}\sum_i \hat{n}_{ai}\hat{n}_{bi} \quad (1.88)$$

In this thesis, unless otherwise noted, the chemical potential μ_{ci} are set to be global among all the lattice sites and used to tune the number of particles in the system.

$$\mu_i = \mu \quad (1.89)$$

1.4.1 Experimental realization of the Twin-Species Model

A mixture with $t_a = t_b$ and $U_a = U_b$ can be realized with ^{41}K atoms in the two lowest hyperfine states $a = |F = 1, m = 1\rangle$ and $b = |F = 1, m = 0\rangle$ (it is understood that the hyperfine quantum numbers are used only as labels at high magnetic fields). At $B_0 \simeq 675$G the above mixture is predicted to feature a relatively narrow Feshbach resonance ($\delta B = 0.15$G) between unlike states, while for like particles the scattering lengths are approximately constant across the narrow resonance and equal to each other ($a_a \simeq a_b \simeq 60a_0$) [64]. Therefore, with a magnetic field near B_0 it is possible to tune U_{ab}, with minimal changes in U_a and U_b. For a heteronuclear mixture of $a =^{41}$K and $b =^{87}$Rb in a square lattice, tunneling rates can be made nearly equal with an appropriate choice of the lattice step. For example, for a lattice step $d = 380$ nm, at lattice strengths such as $5 \leq U_b/t_b \leq 30$, we have $0.85 \leq t_b/t_a \leq 1.15$ and the ratio $U_b/U_a = 0.58$ is constant. Typical values of the tunnelling amplitude are $t_{Rb}/k_B = 2.08\ nK$ for Rubidium and $t_K/k_B = 17.9\ nK$ for Potassium.

Chapter 2

The worm-algorithm Quantum Monte Carlo

In this chapter we analyze the Quantum Monte Carlo Algorithm used for the simulation that led to the results of this thesis. The Quantum Monte Carlo algorithm used for this thesis is a Path-Integral quantum Monte Carlo technique based on the famous *Worm-algorithm Quantum Monte Carlo* developed by Prokof'ev *et al.* in 1997. This algorithm is carefully described in the papers *Worm algorithm quantum Monte Carlo* [53] and *Exact, complete, and universal continuous-time worldline Monte Carlo approach to the statistics of discrete quantum systems* [54]. Both articles discuss a Quantum Monte Carlo technique developed by Prokof'ev *et al.* from Russian Research Center Kurchatov Institute, Moscow in late 1997. The former one it generally presents the quantum Monte Carlo scheme used showing some simulations results of a pure bosonic Hubbard model in 1D. The latter enters more into details of the quantum Monte Carlo (QMC) algorithm developed, providing more information about how actually the simulation is performed. Furthermore they clearly show how this wordline quantum Monte Carlo procedure, can be formulated directly in continuous time, making the scheme exact.

Prokof'ev *et al.* in 1997 came up with a brand new quantum Monte Carlo algorithm named "Worm" Algorithm quantum Monte Carlo. This algorithm has a particular wordline approach based on imaginary time that allows it to work with non-zero winding numbers and within the grand canonical ensemble. Quantum Monte Carlo procedures in general suffers from significant shortcomings such as the

presence of systematic error due to artificial time discretization, restriction to the simulation with the zero winding numbers, fixed number of particles in the system that restrict simulations within the canonical ensemble only... And more in general, problems related to the numerical nature of the procedure as the well known sign problem, the slow accumulation of statistics when calculating correlation functions of operators not present in the initial Hamiltonian; computation time strongly dependent on the system size, and a general small acceptance rates in update procedures for system described by Hamiltonians with different energy scales. Even though no MC scheme has been found so far capable to overcome all these problems, the cited Worm algorithm QMC has been proven to efficiently remove some of the limitations listed above. Within this approach it is indeed possible to run simulations in grand canonical ensemble, and explore non-zero winding number configurations. This allows the possibility to take into account the contribution of a transition from an initial bosonic Fock state $|\phi_1\phi_2...\phi_L>$ to a final state $|\eta_1\eta_2...\eta_L>$ where the set $\{\eta_k\}$ being obtained by cyclically permuting $\{\phi_k\}$ M times (with M the value of winding number). The possibility to evaluate a much larger configuration space it is by itself quite important, but can be considered way more crucial if we understand that the possibility to evaluate transition with $M \neq 0$ it allows as a matter of a fact, to measure somehow the delocalization of the system. If we think at the transition probability of the system from an initial state $|n_1n_2...n_L>$ to the same final state $|n_1(t)n_2(t)...n_L(t)>$ after time t:

$$< n_1n_2...n_L|n_1n_2...n_L(t)>=< n_1n_2...n_L|\hat{\mathbf{U}}(\mathbf{t})|n_1n_2...n_L>= \\ =< n_1n_2...n_L|e^{-\frac{i}{\hbar}\hat{\mathbf{H}}t}|n_1n_2...n_L> \quad (2.1)$$

If we split the time in N time intervals Δt_k the transition probability (2.1) gets

$$< n_1n_2\ldots n_L|e^{-\frac{i}{\hbar}\hat{\mathbf{H}}t}|n_1n_2\ldots n_L>= \\ =< n_1n_2\ldots n_L|e^{-\frac{i}{\hbar}\hat{\mathbf{H}}\Delta t_1}e^{-\frac{i}{\hbar}\hat{\mathbf{H}}\Delta t_2}\ldots e^{-\frac{i}{\hbar}\hat{\mathbf{H}}\Delta t_N}|n_1n_2\ldots n_L>= \\ =< n_1n_2\ldots n_L|e^{-\frac{i}{\hbar}\hat{\mathbf{H}}\Delta t_1}\mathbb{I}e^{-\frac{i}{\hbar}\hat{\mathbf{H}}\Delta t_2}\mathbb{I}\ldots\mathbb{I}e^{-\frac{i}{\hbar}\hat{\mathbf{H}}\Delta t_N}|n_1n_2\ldots n_L> \quad (2.2)$$

Recalling the completeness relation definition

$$\mathbb{I} = \sum_{k_1=0}^{\infty}\sum_{k_2=0}^{\infty}\ldots\sum_{k_L=0}^{\infty}|k_1k_2\ldots k_L><k_1k_2\ldots k_L|, \quad (2.3)$$

and substituting it in eq.(2.2) we obtain:

$$< n_{1...L}|e^{-\frac{i}{\hbar}\hat{\mathbf{H}}\Delta t_1}\mathbb{I}e^{-\frac{i}{\hbar}\hat{\mathbf{H}}\Delta t_2}\mathbb{I}\ldots\mathbb{I}e^{-\frac{i}{\hbar}\hat{\mathbf{H}}\Delta t_N}|n_{1...L}>=$$
$$= \sum_{t_1=0}^{\infty}\sum_{t_2=0}^{\infty}\cdots\sum_{t_L=0}^{\infty} \quad \sum_{k_1=0}^{\infty}\sum_{k_2=0}^{\infty}\cdots\sum_{k_L=0}^{\infty} \quad \cdots \quad \sum_{j_1=0}^{\infty}\sum_{j_2=0}^{\infty}\cdots\sum_{j_L=0}^{\infty}$$
$$< n_{1..L}|e^{-\frac{i}{\hbar}\hat{\mathbf{H}}\Delta t_1}|t_{1..L}>< t_{1..L}|e^{-\frac{i}{\hbar}\hat{\mathbf{H}}\Delta t_2}|k_{1..L}>\cdots< j_{1..L}|e^{-\frac{i}{\hbar}\hat{\mathbf{H}}\Delta t_N}|n_{1..L}> \quad (2.4)$$

Where the multiple sums run over all the possible configuration of the system from time 0 to t and each product

$$< n_{1..L}|e^{-\frac{i}{\hbar}\hat{\mathbf{H}}\Delta t_1}|t_{1..L}>< t_{1..L}|e^{-\frac{i}{\hbar}\hat{\mathbf{H}}\Delta t_2}|k_{1..L}>\cdots< j_{1..L}|e^{-\frac{i}{\hbar}\hat{\mathbf{H}}\Delta t_N}|n_{1..L}> \quad (2.5)$$

is a possible path or configuration that leads the system from the initial state at time 0 to the same final state at time t. We've just shown that the transition probability may be expressed in terms of sum of all the infinite possible transitions that could lead the system to the specified final state. And this is somehow exactly how the Monte Carlo simulation works, summing together different contribution of each possible configuration in order to evaluate the expectation of value of different physical quantities. Obviously within the context of a numerical simulations, just a finite number of this possible paths are summed in order to have a converged estimate of the quantity wanted. For each one of those paths (2.5) can be computed the number of permutation M the system undergoes from it's initial state to the final one. This number is called the *"winding number"* and it's intimately related with the considered configuration. By collecting all the computed winding number of all the different configurations summed, one can obtain the distribution of winding numbers among all the different configurations. It is then clear that if the main contribution to the evaluation of the probability of the system to remain in the same state (eq.(2.4)) is given by those configuration with large value of M, this would lead us to the conclusion that the particles of the system described by that state may have an intrinsic delocalized behaviour. Otherwise, if the main contribution is given by state whose $M = 0$ or small in general, that might means that the particles of the system tends to stay in the very same configuration as the time goes by. This information in terms of winding number, and more in general, the possibility to have an algorithm capable to explore those configurations with $M \neq 0$, can be therefore very peculiar for the simulation of highly delocalized and strongly correlated systems

such as Bose-Einstein Condensates (BEC) and exotic phase transitions in ultra-cold atoms.

Another interesting feature that comes out quite naturally from this new simulation scheme is a way more efficient calculation of the Green function at finite temperature. Despite other quantum Monte Carlo procedures experience a slow accumulation of statistics when computing this quantity, this new technique is able to solve this problem by formulating a new local update procedure in terms of motion of *two* worldline discontinuities (the so called *worm*).

2.1 Worm Algorithm Quantum Monte Carlo

The Worm Algorithm Quantum Monte Carlo [53, 54] is a *Path-Integral Monte Carlo (PIMC)* technique based on the so called imaginary time approach. PIMC are in general imaginary time Quantum Monte Carlo in which is possible to evaluate the expectation value of the partition function and other physical quantities at finite temperature T. According to the rules of Statistical Quantum Mechanics, the expectation value of a general observable operator $\hat{O}$ is given by:

$$< \hat{O} >= Tr(\hat{\rho}\hat{O}) \tag{2.6}$$

Where $\hat{\rho}$ is the density operator, defined as:

$$\hat{\rho} = \frac{1}{Tr(e^{-\beta\hat{F}})} Tr(e^{-\beta\hat{F}}) \tag{2.7}$$

With $\beta = \frac{1}{k_B T}$ the inverse temperature and $\hat{\mathbf{F}}$ the grand canonical potential operator defined as

$$\hat{\mathbf{F}} = \hat{\mathbf{H}} - \mu\hat{N} = \hat{\mathbf{H}} - \mu \sum_i \hat{n}_i. \tag{2.8}$$

Recalling the Heisenberg picture the time evolution of an operator is given by:

$$-i\hbar \frac{d\hat{O}}{dt} = [\hat{\mathbf{H}}, \hat{O}] \tag{2.9}$$

Whose general solution is:

$$\hat{O}_{(t)} = \hat{U}^{\dagger}_{(t)} \hat{O} \hat{U}_{(t)} \tag{2.10}$$

where

$$\hat{U}_{(t)} = e^{-\frac{i}{\hbar}t\hat{\mathbf{H}}} \tag{2.11}$$

is the time evolution operator.

By making a change of variable $\beta = -\frac{t}{i\hbar}$ one can rewrite equation 2.9 in the so called *imaginary-time* picture.

$$\frac{d\hat{O}}{d\beta} = [\hat{\mathbf{H}}, \hat{O}] \tag{2.12}$$

Where the imaginary-time evolution become

$$\hat{O}_{(\beta)} = \hat{U}^{\dagger}_{(\beta)}\hat{O}\hat{U}_{(\beta)} \tag{2.13}$$

with

$$\hat{U_{(\beta)}} = e^{-\beta\hat{\mathbf{H}}} \tag{2.14}$$

the imaginary-time evolution operator.

It can now be easily seen that the density operator defined by (2.7) not only satisfies (2.12) and (2.13) but it is exactly proportional to the imaginary-time evolution operator (2.11). This allow one to treat the finite temperature problem, and compute the expectation of value of hermitian operators related to physical quantities at finite temperature, as an imaginary-time evolution. Furthermore, it can be rigorously shown that this imaginary-time scheme allow an easy and correct evaluation of the ground state too. If we consider for example the Hamiltonian operator $\hat{\mathbf{H}}_0$ represented in a given complete orthonormal basis $\{|\alpha>\}$ of Fock's states and taking as zero energy scale the ground-state energy ε_0:

$$\hat{\mathbf{H}}_0 = \hat{\mathbf{H}} - \varepsilon_0 = \sum_{\alpha} \varepsilon_\alpha a^{\dagger}_{\alpha} a_\alpha - \varepsilon_0 \tag{2.15}$$

And we compute the expectation values of $\hat{\mathbf{H}}_0$ using (2.6)

$$
\begin{aligned}
< \hat{\mathbf{H}}_0 >= Tr(\hat{\rho}\hat{\mathbf{H}}_0) = Tr(\frac{e^{-\beta\hat{\mathbf{H}}_0}}{\mathrm{Z}}\hat{\mathbf{H}}_0) = \\
= \frac{1}{\mathrm{Z}}\sum_{\alpha} < \alpha|e^{-\beta\hat{\mathbf{H}}_0}\hat{\mathbf{H}}_0|\alpha >= \frac{1}{\mathrm{Z}}\sum_{\alpha} < \alpha|e^{-\beta(\hat{\mathbf{H}}-\varepsilon_0)}(\hat{\mathbf{H}}-\varepsilon_0)|\alpha >= \\
= \frac{1}{\mathrm{Z}}\sum_{\alpha} < \alpha|e^{-\beta(\hat{\mathbf{H}}-\varepsilon_0)}\hat{\mathbf{H}}|\alpha > -\frac{\varepsilon_0}{\mathrm{Z}}\sum_{\alpha} < \alpha|e^{-\beta(\hat{\mathbf{H}}-\varepsilon_0)}|\alpha > \quad (2.16)
\end{aligned}
$$

Where $\mathrm{Z} = Tr(e^{-\beta(\hat{\mathbf{H}}-\varepsilon_0)})$ is the partition function and follows directly by the expression (2.7). Hence $|\alpha >$ are eigenstates of $\hat{\mathbf{H}}$ by hypothesis the expression (2.16) becomes:

$$
\begin{aligned}
< \hat{\mathbf{H}}_0 >= \frac{1}{\mathrm{Z}}\sum_{\alpha} e^{-\beta(\varepsilon_\alpha-\varepsilon_0)} < \alpha|\hat{\mathbf{H}}|\alpha > -\frac{\varepsilon_0}{\mathrm{Z}}\sum_{\alpha} e^{-\beta(\varepsilon_\alpha-\varepsilon_0)} < \alpha|\alpha >= \\
= \frac{1}{\mathrm{Z}}\sum_{\alpha} e^{-\beta(\varepsilon_\alpha-\varepsilon_0)}\varepsilon_\alpha < \alpha|\alpha > -\frac{\varepsilon_0}{\mathrm{Z}}\sum_{\alpha} e^{-\beta(\varepsilon_\alpha-\varepsilon_0)} = \\
= \frac{1}{\mathrm{Z}}\sum_{\alpha} \varepsilon_\alpha e^{-\beta(\varepsilon_\alpha-\varepsilon_0)} - \frac{\varepsilon_0}{\mathrm{Z}}\sum_{\alpha} e^{-\beta(\varepsilon_\alpha-\varepsilon_0)} = \\
= \frac{1}{\mathrm{Z}}\sum_{\alpha} \varepsilon_\alpha e^{-\beta(\varepsilon_\alpha-\varepsilon_0)} - \frac{\varepsilon_0}{\mathrm{Z}}\sum_{\alpha} e^{-\beta(\varepsilon_\alpha-\varepsilon_0)} = \\
= \frac{1}{\mathrm{Z}}\sum_{\alpha} \varepsilon_\alpha e^{-\beta(\varepsilon_\alpha-\varepsilon_0)} - \varepsilon_0\frac{\mathrm{Z}}{\mathrm{Z}} = \\
= \frac{1}{\mathrm{Z}}\sum_{\alpha} \varepsilon_\alpha e^{-\beta(\varepsilon_\alpha-\varepsilon_0)} - \varepsilon_0 \quad (2.17)
\end{aligned}
$$

Where the definition of the partition function Z has been used in the second term of 2.17. One can suddenly notice, that in the limit $\beta \to \infty$ the expectation value of $\hat{\mathbf{H}}_0$

it is exactly zero.

$$\begin{aligned}
\lim_{\beta\to+\infty} <\hat{\mathbf{H}}_0> &= \lim_{\beta\to+\infty} \frac{1}{Z}\sum_\alpha \varepsilon_\alpha e^{-\beta(\varepsilon_\alpha-\varepsilon_0)} - \varepsilon_0 = \\
&= \lim_{\beta\to+\infty} \frac{1}{\sum_i e^{-\beta(\varepsilon_i-\varepsilon_0)}}\sum_\alpha \varepsilon_\alpha e^{-\beta(\varepsilon_\alpha-\varepsilon_0)} - \varepsilon_0 = \\
&= \lim_{\beta\to+\infty} \frac{1}{e^{-\beta(\varepsilon_0-\varepsilon_0)} + \sum_{i=1} e^{-\beta(\varepsilon_i-\varepsilon_0)}}(\varepsilon_0 e^{-\beta(\varepsilon_0-\varepsilon_0)} + \sum_{\alpha=1} \varepsilon_\alpha e^{-\beta(\varepsilon_\alpha-\varepsilon_0)}) - \varepsilon_0 = \\
&= \lim_{\beta\to+\infty} \frac{1}{1+\sum_{i=1} e^{-\beta(\varepsilon_i-\varepsilon_0)}}(\varepsilon_0 + \sum_{\alpha=1} \varepsilon_\alpha e^{-\beta(\varepsilon_\alpha-\varepsilon_0)}) - \varepsilon_0 = \\
&= \frac{1}{1+0}(\varepsilon_0+0) - \varepsilon_0 = \varepsilon_0 - \varepsilon_0 = 0 \quad (2.18)
\end{aligned}$$

as the terms $e^{-\beta(\varepsilon_{\alpha/i}-\varepsilon_0)}$ go to zero when β goes to infinity and $\alpha/i \neq 0$ because of the exponential dumping (due to the real exponent β) . While for $\alpha/i = 0$ the exponent value is exactly zero, forcing the term to be exactly one. Using the relation (2.17) with the result (2.18) is now possible to define a way to compute the value of the energy ground state simply as

$$\varepsilon_0 = \lim_{\beta\to+\infty} \frac{1}{Z}\sum_\alpha \varepsilon_\alpha e^{-\beta(\varepsilon_\alpha-\varepsilon_0)} \quad (2.19)$$

That means that within this picture one can get the tool to correctly evaluate the expectation of value of a given operator (observable) at the system ground state (if $\beta \to \infty$), as well as the correct behaviour of the quantum system at finite temperature. Furthermore, when the imaginary-time evolution is computed by means of a Monte Carlo simulation, as the imaginary-time variable β is not "imaginary" anymore ($\beta \in \Re$), this new picture allows to avoid the well known *sign problem* that affect others quantum Monte Carlo schemes.

2.1.1 General Principles

Prokof'ev *et al.* in their *worm algorithm quantum Monte Carlo*, developed the discussed imaginary-time scheme starting from the interaction picture. They wrote the grand canonical Hamiltonian operator $\hat{H}$ of the system as a sum of two parts:

$$\hat{H} = \hat{H}_0 + \hat{V} \quad (2.20)$$

Where $\hat{H}_0$ is the diagonal part, and $\hat{V}$ the off-diagonal part. The Hamiltonian $\hat{H}$ is chosen in a given representation corresponding to the full set $\{|\alpha>\}$ of eigenstate of $\hat{H}_0$, such that $\hat{H}_0|\alpha>=E_\alpha|\alpha>$. They defined then the imaginary-time evolution operator (2.14) in its iterative expansion form (the Matsubara time evolution operator) following the standard rules of many-body quantum field theory in the interaction picture:

$$e^{-\beta\hat{H}} = e^{-\beta\hat{H}_0}\mathbf{T}\exp\left\{-\int_0^\beta \hat{V}(\tau)d\tau\right\} \tag{2.21}$$

Where $\mathbf{T}$ is the time ordering operator. And $\hat{V}(\tau) = e^{\tau\hat{H}_0}\hat{V}e^{-\tau\hat{H}_0}$ is the imaginary-time dependent interaction potential in the interaction representation. Writing in its explicit form the Matsubara evolution operator
$\hat{\sigma} = \mathbf{T}\exp\{-\int_0^\beta \hat{V}(\tau)d\tau\}$ one gets exactly the expression found in the paper of Prokof'ev *et al.* [53, 54].

$$\hat{\sigma} = \mathbb{I} - \int_0^\beta d\tau\hat{V}(\tau) + \ldots \\ \cdots + (-1)^m \int_0^\beta d\tau_m \ldots \int_0^{\tau_2} d\tau_1 \hat{V}(\tau_m)\ldots\hat{V}(\tau_1) + \ldots \tag{2.22}$$

It is possible to define $\hat{V}$ as a sum of elementary Hermittian operators $\hat{Q}_s$, whose action on any state of the set $\{|\alpha>\}$ results in another state from the same set.

$$\hat{V} = \sum_s \hat{Q}_s, \qquad \hat{Q}_s = \hat{Q}_s^\dagger, \qquad \hat{Q}_s|\alpha>=-q_{\gamma\alpha}(s)|\gamma> \tag{2.23}$$

This allow to rewrite the Matsubara operator(2.22) as:

$$\hat{\sigma} = \mathbb{I} - \sum_s \int_0^\beta d\tau\hat{Q}_s(\tau) + \ldots \\ \cdots + \sum_{s_1,\ldots,s_m} (-1)^m \int_0^\beta d\tau_m \ldots \int_0^{\tau_2} d\tau_1 \hat{Q}_{s_m}(\tau_m)\ldots\hat{Q}_{s_1}(\tau_1) + \ldots \tag{2.24}$$

Which in components representation turns

$$\begin{aligned}\sigma_{\alpha\gamma} =& < \alpha|\hat{\sigma}|\gamma > = < \alpha|\mathbb{I}|\gamma > - \sum_s \int_0^\beta d\tau < \alpha|\hat{Q}_s(\tau)|\gamma > + \dots \\ \cdots &+ \sum_{s_1,\dots,s_m} (-1)^m \int_0^\beta d\tau_m \dots \int_0^{\tau_2} d\tau_1 < \alpha|\hat{Q}_{s_m}(\tau_m)\dots\hat{Q}_{s_1}(\tau_1)|\gamma > + \cdots = \\ &= \delta_{\alpha\gamma} + \sum_s \int_0^\beta d\tau q_{\alpha\gamma}(s) e^{\tau(E_\alpha - E_\gamma)} + \dots \\ \cdots &+ \sum_{s_1,\dots,s_m} \int_0^\beta d\tau_m \dots \int_0^{\tau_2} d\tau_1 q_{\alpha\nu}(s_m) e^{\tau_m(E_\alpha - E_\nu)} \dots q_{\mu\gamma}(s_1) e^{\tau_1(E_\mu - E_\gamma)} + \dots\end{aligned} \tag{2.25}$$

Where $\{E_\alpha\}$ are the energy eigenstates of $\hat{H}_0$. As we have seen above the average of any observable can be computed thanks to the relations (2.6,2.7) in terms of the imaginary-time evolution. It is therefore sufficient to estimate the matrix element (2.25), to be able to completely describe the state of the system under inspection. According to the expression (2.25) each element $\alpha\gamma$ of the operator $\hat{\sigma}$ can be written as a sum of different contribution

$$\sigma_{\alpha\gamma(\beta)} = \Delta\sigma^{(0)}_{\alpha\gamma(\beta)} + \Delta\sigma^{(1)}_{\alpha\gamma(\beta)} + \Delta\sigma^{(2)}_{\alpha\gamma(\beta)} + \cdots + \Delta\sigma^{(m)}_{\alpha\gamma(\beta)} + \dots \tag{2.26}$$

Where the single $m-th$ contribution $\Delta\hat{\sigma}(\beta)^{(m)}$ correspond to the multiple sum and integral

$$\Delta\sigma^{(m)}_{\alpha\gamma(\beta)} = \sum_{s_1,\dots,s_m} (-1)^m \int_0^\beta d\tau_m \dots \int_0^{\tau_2} d\tau_1 < \alpha|\hat{Q}_{s_m}(\tau_m)\dots\hat{Q}_{s_1}(\tau_1)|\gamma >, \tag{2.27}$$

given by splitting the imaginary-time interval $[0,\beta]$ in m subintervals $\tau_j, (j \in [1 \div m])$.

$$(-1)^m < \alpha|\hat{Q}_{s_m}(\tau_m)\dots\hat{Q}_{s_1}(\tau_1)|\gamma > = q_{\alpha\nu}(s_m) e^{\tau_m(E_\alpha - E_\nu)} \dots q_{\mu\gamma}(s_1) e^{\tau_1(E_\mu - E_\gamma)} \tag{2.28}$$

The general term (2.28) of the series (2.27) represent a sort of *path* in imaginary-time that the system can follow to get from its initial state $|\alpha>$ to the final state $|\gamma>$. The $m-th$ contribution is therefore given by the sum of all the possible path of m imaginary-time steps, that allow the transition from $|\alpha>$ to $|\gamma>$.

The Worm Algorithm Quantum Monte Carlo developed by Prokof'ev *et al.*, performs an estimate of such a form of the Matsubara imaginary-time operator (2.25), in terms of evaluation of the multiple sums and integrals(2.27). The Monte Carlo simulation is used to estimates the value of the singles contributions (2.27) by generating and summing together the contribution of different paths. A sort of random walk is performed in order to generate at each MC step the new trajectory contribution to be added to the current estimate of the Matsubara operator. To do so the series (2.27) is represented by introducing the notion of a "kink of type s_j" which is characterized by a time τ_j, a matrix element of $q_{\alpha\gamma}(s_j)$ and a diagonal energy difference $E_{\alpha\gamma} = E_\alpha - E_\gamma$. The Monte Carlo procedure consists then in a number of rules, or updating procedures, which describes how to go from a trajectory to another by changing the number of kinks, their types and time position. Hence a generic state $|\alpha>$ of the system is represented as a Fock state in the occupation number representation.

$$|\alpha>=|n_{\alpha 1} n_{\alpha 2} ... n_{\alpha L}> \tag{2.29}$$

the transition operators $\hat{Q}_{s_m}(\tau_m)\ldots\hat{Q}_{s_1}(\tau_1)$ from a state to another can be expressed as a succession of creation and annihilation sub-processes on different modes $i \in [1 \div L]$. In such a context, where the state of the system is expressed in terms of occupation number, the trajectory or path described by (2.28) can be visualized graphically by a sort of *Feynman-like* diagram named worldline such the one displayed in figure (2.1). The worldline represent the path in imaginary-time (from 0 to β) described by the state in terms of its occupation numbers, i.e. their change in imaginary time. All the procedures that alter the number, type and positions of the kinks in a worldline actually changes the shape of the worldline pictured in figure (2.1). The entire Monte Carlo process can be seen indeed as a random generator of worldlines, capable to sum together the contribution of these sort of *Feynman Diagram* to the estimate of a set of established physical quantities. However, such a set of procedures need to be chosen very carefully in order to guarantee that the resulting statistic does really correspond to that introduced by eq. (2.25).

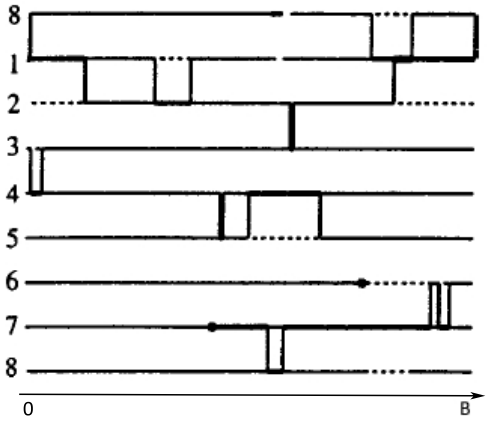

Fig. 2.1 Example of a worldline representing the path of the Fock state of the system in imaginary-time (from 0 to β). Labels $i \in [1,2,3,\dots 8]$ refers to the mode occupation number $\{n_{\alpha i}\}$ of the state (2.29). The width of the solid line is proportional to the mode occupation number $n_{\alpha i}$, and dashed lines are empty modes ($n_{\alpha i} = 0$).

2.1.2 Update Procedures and Statistics

A Monte Carlo technique estimates a generic multiple sum and integral, thanks to the "law of large numbers", by simply averaging over the statistics of different configurations.

$$\sum_{s_1 \dots s_m} \int_0^\beta d\tau_m \dots \int_0^{\tau_2} d\tau_1 g_{s_1 \dots s_m}(\tau_1 \dots \tau_m) f_{s_1 \dots s_m}(\tau_1 \dots \tau_m) = \\ = \lim_{N \to +\infty} \frac{1}{N} \sum_l g_l(T_l), \quad l = \{s_{l1} \dots s_{lm}\}, T_l = \{\tau_{l1} \dots \tau_{lm}\} \quad (2.30)$$

with $f_{s_1 \dots s_m}(\tau_1 \dots \tau_m)$ the probability density distribution and N the number of samplings.
In the algorithm from Prokofe'ev *et al.* the multiple sums and integrals (2.27) are

estimated in a similar way (2.30):

$$\Delta\sigma^{(m)}_{\alpha\gamma(\beta)} = \sum_{s_1,\dots,s_m} (-1)^m \int_0^\beta d\tau_m \dots \int_0^{\tau_2} d\tau_1 < \alpha|\hat{Q}_{s_m}(\tau_m)\dots\hat{Q}_{s_1}(\tau_1)|\gamma >=$$

$$= \sum_{s_1,\dots,s_m} (-1)^m \int_0^\beta d\tau_m \dots \int_0^{\tau_2} d\tau_1 \frac{< \alpha|\hat{Q}_{s_m}(\tau_m)\dots\hat{Q}_{s_1}(\tau_1)|\gamma >}{f_{s_1\dots s_m}(\tau_1\dots\tau_m)} f_{s_1\dots s_m}(\tau_1\dots\tau_m) \approx$$

$$\approx \frac{1}{N}\sum_l \frac{< \alpha|\hat{\mathbf{Q}}_l(T_l)|\gamma >}{f_l(T_l)}, \quad \hat{\mathbf{Q}}_l(T_l) = \hat{Q}_{s_{lm}}(\tau_{lm})\dots\hat{Q}_{s_{l1}}(\tau_{l1}) \quad (2.31)$$

Where the algorithm at each Monte Carlo step update the sum over the index l by randomly generating the new path $< \alpha|\hat{\mathbf{Q}}_l(T_l)|\gamma >$ through a random implementation of kink-motions and kink-modifications procedures; adding then the new contribution updating the new value of the average (2.31) (and the related physical quantities: expectation value of physical operators computed thanks to the Matsubara Operator, e.g. energy, number of particles...). In order to assure that the annihilation and creation procedures used to move and generate new kinks, satisfies the required statistics, a Metropolis method is used to reproduce the correct sampling of the probability distribution $f_l(T_l)$ of the paths. The Metropolis method assures that the random generation of a general path follows a given probability distribution by satisfying a proper balancing condition (2.32). To understand how the Metropolis method has been implemented for the "worm algorithm" QMC, let us start by considering a very general case for a creation and an annihilition procedures involving the modification of n kinks of a given type $s_1\dots s_n$ and at a given imaginary-time instant $\{\tau_1\dots\tau_n\}$.

Creation The creation procedure involve two steps:

1. One first consider the probability $W(\tau_1\dots\tau_n)$ of the creation of a set of n kinks of a given type, at a particular n-dimensional time instant $\{\tau_1\dots\tau_n\}$. This probability is arbitrary but chosen nonzero at every physically meaningful configuration of kinks.
2. The second step is to accept with probability $P_{acc}(\tau_1\dots\tau_n)$ or reject the proposed set of n kinks.

Annihilation The annihilation procedure is much simpler as the set of n kinks can be either removed with probability $P_{rem}(\tau_1\dots\tau_n)$ or remain untouched.

By both considering the probability density $A_n(\tau_1 \dots \tau_n)$ of finding a configuration with the specified n kinks (for creation procedures), and the probability A_0 of finding a configuration without the specified n kinks (for annihilation procedures). Together with the probability p_c and p_a of addressing the 2 procedures (creation and annihilation respectively). One finds that the equation of balance of the two sub-processes is:

$$p_c A_0 W(\tau_1 \dots \tau_n) P_{acc}(\tau_1 \dots \tau_n) d\tau_n \dots d\tau_1 = p_a dAn(\tau_1 \dots \tau_n) P_{rem}(\tau_1 \dots \tau_n), \quad (2.32)$$

that states the equivalence of processes that can creates/annihilates n kinks. Adding the considerations on the statistical interpretation of equation (2.25):

$$\frac{dAn(\tau_1 \dots \tau_n)}{A_0} = d\tau_n \dots d\tau_1 \prod_{i=1}^{n} q_{\alpha_i \nu_i}(s_i) e^{\tau_i (E_{\alpha_i} - E_{\nu_i})}. \quad (2.33)$$

Combining (2.32) and (2.33) we finally get the self-balancing condition of the two processes:

$$\frac{W(\tau_1 \dots \tau_n) P_{acc}(\tau_1 \dots \tau_n)}{P_{rem}(\tau_1 \dots \tau_n)} = \frac{p_a}{p_c} \prod_{i=1}^{n} q_{\alpha_i \nu_i}(s_i) e^{\tau_i (E_{\alpha_i} - E_{\nu_i})} \triangleq R(\tau_1 \dots \tau_n). \quad (2.34)$$

This result allows us to write the probability of acceptance or removal of a given randomly generated set of n kinks as:

$$\begin{aligned} P_{acc}(\tau_1 \dots \tau_n) &= \begin{cases} \frac{R(\tau_1 \dots \tau_n)}{W(\tau_1 \dots \tau_n)}, & \text{if } R(\tau_1 \dots \tau_n) \leq W(\tau_1 \dots \tau_n); \\ 1, & \text{otherwise.} \end{cases} \\ P_{rem}(\tau_1 \dots \tau_n) &= \begin{cases} \frac{W(\tau_1 \dots \tau_n)}{R(\tau_1 \dots \tau_n)}, & \text{if } R(\tau_1 \dots \tau_n) \geq W(\tau_1 \dots \tau_n); \\ 1, & \text{otherwise.} \end{cases} \end{aligned} \quad (2.35)$$

As discussed above every procedure of creating/modifing a given set of kinks can be expressed in terms of creation and annihilation procedures. These two procedures can be adressed respectively with probability p_c and p_a providing the possibility to create more complex procedures. Below are described in summary the possible update procedures that the algorithm performs in order to efficiently visit the configuration space.

Kink motion Is that class of procedures that do not changes the number of kinks in the worldline. In this procedures a kink is moved in imaginary-time. Firstly is decided randomly an imaginary-time step τ_0. Then the kink is removed from its position in τ_0 and another kink is created in another arbitrary position $\tau_f \in [\tau_1, \tau_2]$. Where τ_1 and τ_2 are the nearest lower and upper kinks respectively, in imaginary-time.

Creation and Annihilation of kink-antikink pairs A procedure where a pair of kink-antikink is created or destroyed. It follows straightforward from the general guideline explained above in terms of creation and annihilation procedures. This kind of update routine alters the number of kinks in a worldline by a factor of four as the each kink process added or deleted modifies two kink labels $q_{\alpha_i \nu_i}(s_i)$. For this reason one passes from a number of kink N_{label} in a worldline to a number $N_{label}+4$ after the pair is added (for creation). While from a number of kink N_{label} to $N_{label}-4$ when the pair is removed. Hence in general the probability to adress a creation/annihilation process in a given place is uniform and is $\propto 1/N_{label}$, the ratio p_a/p_c in (2.34) are modified depending on the fact we are creating or annihilating the pair.

$$\begin{aligned} \frac{p_a}{p_c} &= \frac{N_{label}}{N_{label}+4} \qquad \text{(creation)} \\ \frac{p_a}{p_c} &= \frac{N_{label}-4}{N_{label}} \qquad \text{(annihilation)} \end{aligned} \tag{2.36}$$

From this point, it comes out quite naturally how annihilation and creation processes adress probability are different in general.

Motion/Modification of worldline discontinuities Are those procedures that insert discontinuities in the worldline, and practically alters the numbers of particles of the system. They allow to explores those configurations with $M \neq 0$ and simulate quantum statistic among configurations with different numbers of particles, i.e. to work in the grand canonical ensemble. We refer to this procedures more accurately in the next section.

2.1.3 A Worm in a worldline

In this final section we discuss those update procedures that are the main characteristic and literally names this Quantum Monte Carlo algorithm. These procedures, as mentioned above, allow to explore the contribution of nonzero winding numbers worldline and simulate the system with different particle number configuration. This gives the possibility to accumulate statistics from configuration of the system with different number of particles and work indeed in the grand canonical ensemble. In general, most of the QMC algorithms that works in grand canonical ensemble try to attempt the goal of exploring configurations with different number of particles by inserting *fixed* discontinuities in the worldline. A discontinuity is in general inserted at a given *fixed* imaginary-time τ_1 and then removed at imaginary-time τ_2. The algorithm performs then standard modification procedures of the worldline exploring the contribution of different configurations with those two fixed discontinuity. When enough statistics is collected, the position of the discontinuities is changed and the calculation is repeated. For each position of the discontinuities is computed the contribution of different configuration to the Matsubara operator (2.22) together with the Green function $\mathscr{G}(i,j,\tau_1,\tau_2)$:

$$\mathscr{G}(i,j,\tau_1,\tau_2) = Tr(\hat{\rho}\mathbf{T}\hat{a}_i(\tau_1)\hat{a}_j{}^{\dagger}(\tau_2)) = \frac{1}{Tr(e^{-\beta\hat{H}})} Tr(e^{-\beta\hat{H}_0}\mathbf{T}\hat{\sigma}\hat{a}_i(\tau_1)\hat{a}_j{}^{\dagger}(\tau_2)) \tag{2.37}$$

Where $\mathbf{T}$ is the imaginary-time ordering operator, and $\hat{H}$ represents in this case the grand canonical Hamiltonian with the term $-\mu\hat{N}$ included. The Green function (2.37) gives exactly the transition probability of creating a kink at τ_1 end destroying another at τ_2. It is the average value of the operator $\hat{a}_i(\tau_1)\hat{a}_j{}^{\dagger}(\tau_2)$ computed throughout the relation (2.6) using the Matsubara operator.

The knowledge of the Green function contributes to the evaluation of the correlators of field operators and enables us to find a whole series of physical characteristics of a system. Formally, the only difference between the statistics given by eq. (2.22) and the Green's function is that there are two extra kinks. Hence one has the possibility of calculating the Green's function in a unified process, together with standard thermodynamic averages. Unfortunately, the mechanism discussed above is extremely slow and suffers from slow accumulation of statistic. Prokof'ev *et al.* showed how it is possible to overcome this drawback and find a more efficient way to compute the Green's function of the system. They come up with a rather simple idea,

they proposed to simply introduce the possibility to move the discontinuities rather then keep them fixed. They called this method a *"worm" algorithm* as a disconnected worldline resemble a worm. They suggested:

What if instead of sampling different trajectories around the dead worm, we will make it "alive" and sample different trajectories through the motion of worldline discontinuities?

In this way, the algorithm can accumulate statistics more efficiently by randomly choose from a wider class of procedures without the need to split the calculation between steps of imposed fixed discontinuities. Naturally it comes out that procedures that alters just the shape of the worldline, without touching the discontinuities, will contribute more to the evaluation of the evolution operator; while those that handle the creation/annihilation and motion of discontinuities will contribute more to the computation of the Green's function. Within this context below are summarized the set of procedures that involves discontinuity motion, creation and destruction both in space and in imaginary-time.

Creation and Annihilation of two worldline discontinuities This procedure create/annihilate two discontinuities (particles) in a given place of a worldline: $\hat{a}_i(\tau_1)\hat{a}_i^{\dagger}(\tau_2)$ or $\hat{a}_i^{\dagger}(\tau_1)\hat{a}_i(\tau_2)$. When a particle is deleted at imaginary-time τ_1 another is created at time $\tau_2 > \tau_1$. If at time τ_1 the particle is created, another is destroyed at time τ_2. The annihilation procedure deletes discontinuities and makes the trajectory closed. It can be applied, say, when the "head" and the "tail" are on the same site and there are no other kinks between them. The opposite procedure creates a short straight worm (thus seeding a new worldline, or a gap in an existing worldline).

Jump / Reconnection This procedure corresponds to the shift of the worm end in space by inserting/deleting a kink to the left of the discontinuity annihilating a particle (the "head") and to the right of the discontinuity creating a particle (the "tail").

Shift in time This is a trivial procedure of choosing another time position for the discontinuity on an interval between the two adjacent kinks.

Prokof'ev *el al.* finally show that the above discontinuity handling procedures naturally include those listed in the prevoius section (kink motion, and kink-antikink pair creation/destruction) pointing that: *"One can even completely ignore all the other update procedures, such as moving other kinks and working with kink-antikink pairs, probably at the expense of being less efficient, but still remaining accurate, complete, and universal"*.

The general scheme of this Worm Algorithm Monte Carlo is in summary really simple: at each Monte Carlo step, by choosing from different update procedures according to a proper probability, a new worldline is generated and added to the estimate of the Matsubara operator. Parallely, different physical quantities are computed and their estimate updated. Strictly speaking, by simply moving the head and the tail of the worm among the wordline, new configurations are explored and used to compute the average of the desired physical observables. Here, head and tail of the worm act exactly as annihilation $\psi_{(\mathbf{r})}$ and creation $\psi^{\dagger}_{(\mathbf{r})}$ field operators respectively. Furthermore, by collecting statistics of the presence of head and tail in every single site i it is possible to estimate all those physical quantities related with the local creation and annihilation operators $a_i^{\dagger}$ and a_i (e.g. single-site occupation numbers $\langle \hat{n}_i \rangle$, correlators $\langle a_i^{\dagger} a_j \rangle$ etc. ...).

The main physical quantities that can be computed with this algorithm are then the mean energy of the system, the mean number of particles, the Green function, the winding number distribution, the mean occupation number of each lattice site, different possible density-density correlators... However, it is always possible to handle the different procedures implemented, make modifications, and compute different physical observables whose computation was not physically implemented in the original version of the code. This feature enhance considerably the capability of the algorithm initially thought by Prokof'ev *et. al.* opening it to a wide range of possible applications.

2.2 The 2-worm Algorithm

The Quantum Monte Carlo algorithm used in this thesis is the *2-worm algorithm* Quantum Monte Carlo [40], a modification of the original worm algorithm described above that allows the quantum-mechanical statistical study of a mixture of 2 bosonic

species trapped in an optical lattice. In this version of the code, a second worm is introduced in order to explore the configurations of the Fock space of the second bosonic species.

Here the presence of the two worms, gives the possibility to estimate the expectation values of all those physical quantities related to the annihilation and creation operators of the two bosonic species: a_i, $a_i^\dagger$, b_i and $b_i^\dagger$. By simply moving head and tail of the two worms across the lattice and the imaginary time steps, different configurations are generated and used to compute the quantum-statistical averages of the desired physical quantities, both global (e.g. $\langle H \rangle$, $\langle N_a \rangle$, $\langle N_b \rangle$ ...) and local (e.g. $\langle n_{ai} \rangle$, $\langle n_{bi} \rangle$ ...).

2.3 Final remarks

The discussed Monte Carlo technique is very useful in order to understand properties of the ground state of the system under simulation, as well as its mean behaviour at finite temperature. The possibility to work with non zero winding number and the efficient method adopted to evaluate the Green function of the system increase its potential and make this scheme very useful for the study of many-body quantum systems at very low temperatures. Furthermore, the extreme flexibility and the possibility to easily add to the algorithm the computation of desired physical observables adapting it to the needs of different physical problems, easily explain the reasons of the success of this algorithm in the world of quantum simulation.

Chapter 3

The twin-species model Phase Diagram

In this chapter we reconstruct the ground-state phase diagram of two bosonic twin species trapped in a two-dimensional, square, optical lattice. The results and the discussions contained in this chapter have mainly been published in the paper [55]. A system of two bosonic species trapped in an optical lattice is well described by the Bose-Hubbard model shown in chapter 1. In the past, countless papers joined the effort to reconstruct the ground state phase diagram of this model [55]-[26]. However, as can be noticed by Hamiltonian 1.82 the phase diagram of the 2-components Bose-Hubbard model can be extremely complicated as it depends, in principle, on at least seven degrees of freedom: t_a, t_b, U_a, U_b, U_{ab}, μ_a, and μ_b. However, despite the great efforts made in these years, the entire picture is far from being complete. A considerable work is still required in order to unravel the complete structure of the phase diagram. Within this spirit, this chapter focuses on the investigation of the ground-state phase diagram restricted to the so-called twin-species case (see chapter 1). The twin-species model is that symmetric case where the two bosonic components features equal hopping parameters $t_a = t_b = t$, equal intra-species interactions $U_a = U_b = U$, and equal number of particles $N_a = N_b$.

We initially compute the phase diagram by considering a homogeneous lattice (periodic boundary conditions) at total integer filling $n = N/M = 1$ where, $N = N_a + N_b$ is the total number of particles and M is the number of lattice sites (i.e. one particle per lattice site). We then move away from this initial symmetrical

condition by adding increasing level of complication in order to explore more general situations and include effects characterizing real systems. This is done for example by studying the behaviour of the phase diagram at generic non-integer filling and population imbalance. Or by relaxing the homogenous lattice hypothesis by applying an external harmonic confinement in order to simulate more realistic situations closer to experimental realizations.

We show in the present chapter how the twin-species BH phase diagram exhibits a rich variety of exotic quantum phases such as double super fluids, supercounterflow, demixed superfluid and demixed Mott-Insulator. Demixed phases are quantum phases characterized by spatial separation of the two species in the lattice. In literature, demixing effects have been widely studied in the context of continuous systems [66–72], while a smaller effort have been devoted to the study of systems in a lattice of both Bose-Fermi mixtures [73, 74] and Bose-Bose mixtures [1, 82, 22, 65]. Besides the derivation of the ground state phase diagram, one of the central topic we want to focus on in this chapter is indeed the investigation on the conditions under which these phases can be stabilized and detected. We introduce for such a task a suitable demixing parameter and we exploit particular off-diagonal correlators which allows to design experimental observation of the various phases through time-of-flight images.

The chapter is organized as follows, we first briefly review the model and method used for our investigation, we then move to the description of the reconstruction of the phase diagram for the homogeneous twin species model at total filling $n = 1$. We analyze here in details the different quantum phases that arise from the phase diagram and the method used for their detection. We then move to study both phase diagram and demixed phases for generic non-integer filling factors. We also study supercounterflow in the case of population imbalance ($N_a \neq N_b$) and find that SCF is stabilized as long as the condition $n = 1$ is satisfied, although the superfluid response in the counter-flow channel does depend on the population imbalance. Finally, we study the system in a trap where the local filling factor imposed by the presence of an external harmonic trap, leads to the formation of spatial shell structures of mixed/demixed configurations depending on the interplay between inter- and intra-species potentials.

3.1 Method and Model

For the sake of clearness we remind here the Hamiltonian of the twin-species Bose-hubbard model describing a mixture of twin bosonic species trapped in a uniform, two-dimensional (2D), square optical lattice.

$$H = H_a + H_b + U_{ab} \sum_i n_{ai} n_{bi} \tag{3.1}$$

where U_{ab} is the inter-species repulsion, $n_{ai,bi}$ is the number operator at site i for species A and B, and

$$H_c = \frac{U}{2} \sum_i n_{ci}(n_{ci} - 1) - t \sum_{\langle ij \rangle} c_i^\dagger c_j - \sum_i \mu_{ci} n_{ci} \, , \tag{3.2}$$

with $c = a, b$ denoting the bosonic species, and operators c_i, $c_i^\dagger$ satisfying the standard commutator $[c_i, c_i^\dagger] = 1$. Parameter U represents the common intra-species repulsion, t is the hopping amplitude for the two bosonic twin-species, and $\mu_{ci} = \mu_c$ ($\mu_{ci} = \mu_c - \omega_H \vec{r}_i^{\,2}$) the chemical potentials in the homogeneous (trapped) case. Chemical potentials μ_c are chosen to be $\mu_a = \mu_b = \mu$ to satisfy the symmetric balanced population requirement ($N_a = N_b$) of the twin-species model; this condition is relaxed when we study the super counterflow phase in presence of population imbalance. The symbol $\langle ij \rangle$ refers to summation over nearest neighboring sites. Unless otherwise noted, we work at zero temperature and integer total filling $n = N/M = 1$ where, $N = N_a + N_b$ is the total number of particles and $M = L^2$ is the number of sites for a lattice of linear size L (in unit of the lattice step a which we set as our unit length). The lattice topology is chosen to be square (four nearest neighborhood) and homogeneous (periodic boundary conditions). Obviously, we relax the latter condition when we analyze the system in a trap.

In this chapter, we explore the phase diagram of model (3.1) as a function of U/t and U_{ab}/t with particular emphasis on the supercounterflow and demixed phases. Our results are based on large-scale path-integral quantum Monte Carlo simulations by a two-worm algorithm [40] (see chapter 2 for details). Unless otherwise noted, we perform simulations for system sizes $L = 8, 16, 24, 36$ and we work at inverse temperature $\beta = L/t$ which ensures that the system is in its ground state.

3.2 Ground state phase diagram at $n = 1$

The ground-state phase diagram of the twin-species model (3.1) at integer total filling $n = 1$ is shown in FIG. 3.1 in the U/t vs U_{ab}/t plane. As shown in the phase

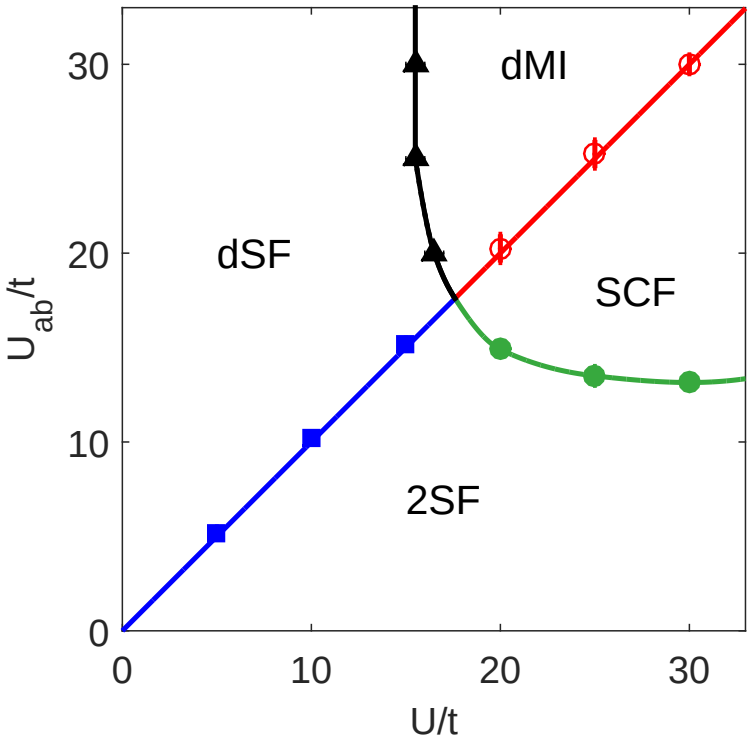

Fig. 3.1 Ground-state phase diagram of twin bosonic species trapped in a uniform optical lattice at $n = 1$. Four phases are stabilized: double superfluid (2SF), supercounterflow (SCF), demixed Mott-Insulator (dMI), and demixed superfluid (dSF). Symbols mark the phase boundaries as calculated from Monte Carlo simulations (see text). Whenever not visible, error bars lies within the symbol size.

diagram of FIG. 3.1 we found the presence of four different quantum-phases and a *demixing* effect whenever the inter-species potential U_{ab}/t become stronger than the intra-specie interaction U/t. The demixing effect, also known in literature under the name of phase segregation or phase separation, consists in a spatial separation between the two bosons species in the lattice. We now describes the four quantum phases found in the phase diagram of FIG. 3.1.

Double Superfluids (2SF) is a quantum phase in which both bosons species coexist in a superfluid state. In this phase, the phase coherence imposed by the superfluid states leads to a uniform density of the two bosonic components among the lattice sites. This is due to a constant value of the mean occupation number $\langle n_{ai}\rangle = \langle n_{bi}\rangle = \frac{n}{2}$, while the non-zero quantum fluctuation $\langle n_{ci}^2\rangle \neq 0$ ($c = a, b$) and the gapless excitation spectra reflect the superfluid character of the two components. The 2SF phase features two $U(1)$ broken symmetries and is characterized by order parameters $\langle a\rangle \neq 0$ and $\langle b\rangle \neq 0$, or, equivalently, finite stiffness of the total superfluid flow $\rho_{\text{tot}} \neq 0$, and finite stiffness of the relative superfluid flow $\rho_{\text{SCF}} \neq 0$ (see subsection 3.2.2 for details and definitions of the superfluidity stiffnesses).

Demixed-SuperFluid (dSF) A double superfluid phase where the two bosons species are spatially separated on the lattice (they complementary occupy different portion of the lattice). The property of the two superfluids are the same as those described for the 2SF phase with the only difference lying in their spatial distribution. The dSF features two $U(1)$ broken symmetries, but the two species occupy different regions of the lattice. Therefore, in this case the mean occupation number are $\langle n_{ai}\rangle = n$ and $\langle n_{bi}\rangle = 0$ ($\langle n_{ai}\rangle = 0$ and $\langle n_{bi}\rangle = n$) for the lattice site occupied by species A (B).

Demixd-Mott-Insulator (dMI) is a quantum phase in which the two bosonic species are two spatially separated Mott-Insulators. A Mott-Insulator is an incompressible, insulating quantum phase featured by an energy gap between the ground state and first exited states. While the dSF is characterized by two U(1) broken symmetries over spatially separated regions, in the dMI these symmetries are restored, that is, the system loses its off-diagonal long range (anisotropic) correlations and becomes insulating. In this phase quantum fluctuations are totally forbidden $\langle n_{ci}^2\rangle = 0$ ($c = a, b$) and the mean occupation number can assume only integer values $\langle n_{ci}\rangle = n \in \mathbb{N}$.

Super Counterflow (SCF) is a quantum phase where the mixture globally behaves as a Mott-Insulator but low-energy transport is allowed as non-dissipative superfluid of particle-hole pairs [1]. Strictly speaking, the name *super counterflow* [1] come from the presence of two finite superfluid currents of the two species in opposite directions (two counter-superfluids). The SCF phase restores one $U(1)$ broken symmetry and is characterized by order parameter

$\langle ab^{\dagger}\rangle \neq 0$ while $\langle a\rangle = 0$ and $\langle b\rangle = 0$, or, equivalently, zero total superfluid stiffness, $\rho_{\mathrm{tot}} = 0$, and finite relative superfluid stiffness, $\rho_{\mathrm{SCF}} \neq 0$.

As we previously mentioned, the demixed phases are characterized by spatial separation of the two components. This phenomenon is observed whenever $U_{ab} > U$ (as found in [1] within the isospin picture of bosonic mixtures for the Mott region). A heuristic derivation of this condition for the case of generic filling factor is given in subsection 3.2.1. In agreement with [75], we find that demixing is observed as soon as $U_{ab}/t > U/t$ for any value of U/t. In a demixed phase the density distribution of the two components is anisotropic on the lattice with density maxima of one species corresponding to density minima of the other (each site can be occupied either by bosons of species A or B, but never by both at the same time). This is even clearer by looking at the density maps of FIG. 3.2 where we can compare the typical density distributions of different quantum phases. In FIG. 3.2 are displayed the quantum-statistical average of the particle number $\langle n_{ai}\rangle$, $\langle n_{bi}\rangle$. The x and y axis denote the x and y coordinates on the lattice. The color code is displayed on the the right bar. Panel a) refers to the 2SF case where the density of each species is uniformly distributed in the lattice, corresponding to the spatial coexistence of the two species. Panel b) and c) refer to the dSF phase and dMI phase respectively. Here, we clearly see that the two components occupy spatially-separated regions with well defined boundaries of a few lattice steps of thickness where the two components coexist. By comparing panel b) and c) of FIG. 3.2 we can notice that, in the double Mott case, the boundaries between the regions occupied by the two species tend to be rough and irregular, and compenetration between the regions is more pronounced. The reasons that lead to this evidence seems to be suggested by the reduced mobility of bosons in the dMI phase due to the stronger interaction regime in which this phase is stabilized (dMI phase is stabilized for higher value of U/t and U_{ab}/t than the dSF phase). In FIG. 3.2 we neglected to plot the density map of the SCF phase as it results perfectly identical to the density map of the 2SF phase (panel a)). The particle-hole superfluidity of the SCF phase leads the mean occupation numbers of the two species to be identical and equal to $n/2$ (as in the 2SF phase), this classifies the SCF as a mixed phase from the mixing/demixing point of view.

As a final comment to the phase diagram of FIG. 3.1, it is worth noting that both 2SF and dSF are conducting phases, while dMI and SCF are insulating phases, although SCF supports flow in the so-called particle-hole channel. In order to reach

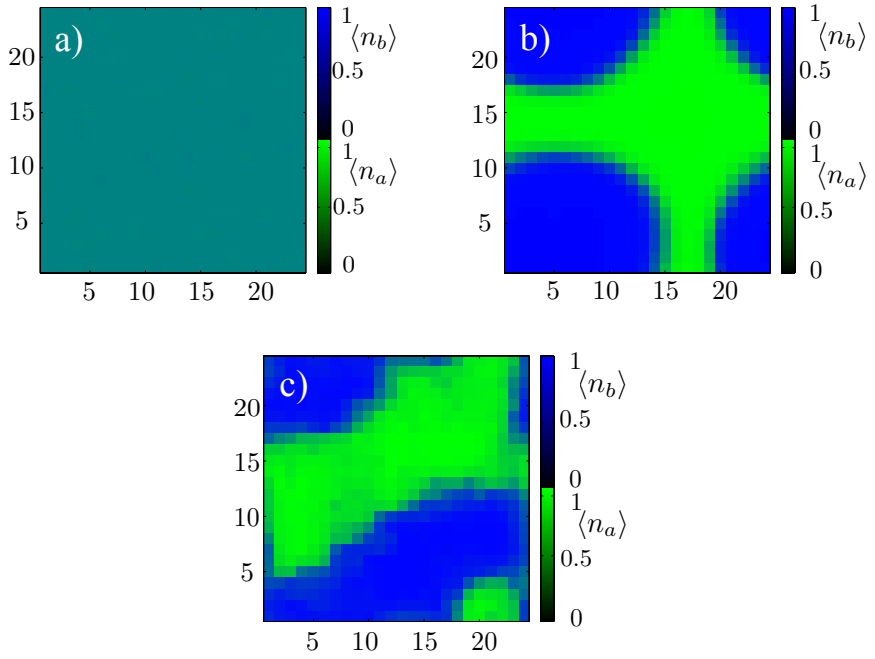

Fig. 3.2 Quantum-statistical average of the particle number $\langle n_{ai} \rangle$, $\langle n_{bi} \rangle$. The x and y axis denote the x and y coordinates on the lattice. The color code is displayed on the the right bar. Panel a): 2SF phase at $U/t = 10$, $U_{ab}/t = 7$ with density uniformly distributed in the lattice. Panel b): dSF phase at $U/t = 15$, $U_{ab}/t = 20$ with two components occupying spatially-separated regions of the lattice. Panel c): dMI phase at $U/t = 20$, $U_{ab}/t = 22$ with two components occupying spatially-separated regions of the lattice. Compenetration between the two regions is noticeable.

the insulating phases, both intra- and inter-species interactions have to be strong enough. Indeed, for $U_{ab}/t \leq 13.5$ ($U/t \leq 15.5$) the 2SF (dSF) phase is stable for arbitrarily large U/t (U_{ab}/t).

3.2.1 Derivation of the condition for demixing

The mixing/demixing effect can be interpreted in a simple way for the dSF-SF transition at generic filling factor. In a perturbative framework, where the energy contribution of tunneling processes is assumed to be negligible, one should compare the energy of the ground-state with the two species spatially separated to the energy of the ground-state where the two species coexist within the lattice. When the two

species occupy spatially separated regions of the lattice $\mathscr{R}_a$ and $\mathscr{R}_b$, we assume that M_a (M_b) sites of $\mathscr{R}_a$ ($\mathscr{R}_b$) are occupied by bosons A (B), with r_a (r_b) sites containing $n+1$ ($m+1$) bosons, and $M_a - r_a$ ($M_b - r_b$) sites containing n (m) bosons. Note that the total number of sites is given by $M = M_a + M_b$ while the total number of particles is $N_a = M_a n + r_a$, $N_b = M_b m + r_b$. The nonuniform filling in $\mathscr{R}_a$ and $\mathscr{R}_b$ reflects the SF character of the two species. The resulting energy reads:

$$\begin{aligned} E_0 &= \frac{U_a}{2} M_a n(n-1) + \frac{U_b}{2} M_b m(m-1) \\ &+ U_a r_a n + U_b r_b m - \mu_a N_a - \mu_b N_b \,, \end{aligned} \tag{3.3}$$

where the U_{ab}-dependent term is absent due to the spatial separation of the two species. The mixing effect is described by: a boson is lost from each site of $\mathscr{R}_a$ ($\mathscr{R}_b$) occupied by $n+1$ ($m+1$) bosons while r_a (r_b) sites appear in $\mathscr{R}_b$ ($\mathscr{R}_a$) with m bosons B and one boson A (n bosons A and one boson B). U_{ab} interaction term is now activated and the resulting energy is

$$\begin{aligned} E_0' &= \frac{U_a}{2} M_a n(n-1) + \frac{U_b}{2} M_b m(m-1) \\ &+ U_{ab}(r_a m + r_b n) - \mu_a N_a - \mu_b N_b \,. \end{aligned} \tag{3.4}$$

This mutual exchange of bosons between $\mathscr{R}_a$ and $\mathscr{R}_b$ represents the mixing process with the lowest-energy cost in the minimum-energy scenario. The condition $E_0 < E_0'$ (justifying the transition from the uniform ground state to the demixed state) implies that $U_{ab}(r_a m + r_b n) > U_a r_a n + U_b r_b m$ which reduces to the well-known condition $U_{ab} > U$ for $n = m$ and $U_a = U_b$. This elementary argument is valid in the SF regime due to its semiclassical character. Although the condition for demixing $U_{ab} > U$ seems to hold in general for any value of the interactions Uab/t and U/t, this simple treatment cannot be extended to the transition from the dMI-SCF phase where quantum correlations and hopping processes play a preminent role.

3.2.2 SCF phase transitions

The Super Counterflow phase is a global Mott-insulator phase where mobility is allowed as superfluidity of particle-hole pairs. The detection of the transition to a SCF phase is achieved by measuring the superfluidity stiffness [76] in the channel

of super-counterfluidity. This is possible by performing a change of variable in the definition of the winding numbers. As shown in chapter 2 the winding numbers are physical quantities that carry the information of both the amount of delocalization and long-range correlation of a given boson field $\hat{\phi}_c(\vec{r})$ ($c = a, b$). Winding numbers are defined as topological quantum numbers and are associated to a particular evolution in imaginary-time of the configuration representing the lattice (see chapter 2). In two-dimensions they are a vectorial quantity and they are computed along both the spatial directions x and y. The winding number $\vec{W}_c = (W_c^x, W_c^y)$ numerically describes the net number of times the N_c bosons of a species $c = a, b$ wound around the periodic cell along a given direction (x and y) in imaginary-time (they note how many times periodic boundary conditions have been invoked).

As any quantum-mechanical physical observable, the winding numbers, from the physical point of view, are described by a proper quantum operator and can be known only in statistical terms by measuring their expectation value $\langle \vec{W}_c \rangle$ and the quantum fluctuation $\langle \vec{W}_c^2 \rangle$ (their variance). In terms of quantum simulation, expectation value and variance of $\vec{W}_c$ are computed by collecting statistics of all the possible values of the winding number $\vec{W}_c$ from different configurations'evolution generated throughout the simulation. The QMC algorithm during the simulation collects the statistical distribution of possible winding numbers, and compute expectation values and quantum fluctuations of $\vec{W}_c$ by measuring the statistical mean and variance of such a distribution. What plays a central role in measuring the delocalization (and therefore correlation) of a bosonic species $C = A, B$ is the expectation value of the fluctuation $\langle \vec{W}_c^2 \rangle$ of the winding number operator ($c = a, b$). If $\langle \vec{W}_c^2 \rangle = 0$ ($\langle \vec{W}_c^2 \rangle \neq 0$) it means that the species C is localized (delocalized).

As mentioned above, in order to investigate the presence of the SCF phase, it is useful to define the new set of winding number $\vec{W}_s = \vec{W}_a + \vec{W}_b$ and $\vec{W}_d = \vec{W}_a - \vec{W}_b$ where $\vec{W}_a$ and $\vec{W}_b$ refer to winding numbers of species A and B respectively. The superfluidity stiffness in both total ($\vec{W}_s$), and relative ($\vec{W}_d$) channels are then defined as:

$$\rho_{tot} = \frac{\langle \vec{W}_s^2 \rangle}{2\beta} \tag{3.5}$$

$$\rho_{SCF} = \frac{\langle \vec{W}_d^2 \rangle}{2\beta} \tag{3.6}$$

where $\langle \vec{W}_s^2 \rangle$, $\langle \vec{W}_d^2 \rangle$ are the computed mean values of the $\vec{W}_s^2$ and $\vec{W}_d^2$ operators that give information proportional to the width of the quantum fluctuations of the new set winding numbers (width of the winding numbers distribution). For the sake of notation, from now on, we will refer to ω_s and ω_d to identify particular winding number values in the statistics of the winding number operators $\vec{W}_s$ and $\vec{W}_d$.

The 2SF phase is characterized by relatively large and finite values of both $\langle \vec{W}_s^2 \rangle$ and $\langle \vec{W}_d^2 \rangle$ (and therefore ρ_{TOT} and ρ_{SCF}). This is due to the isotropic long-range correlation of both bosonic species through the entire lattice. For the SCF phase this is no longer the case, the presence of only the particle-hole superfluidity and a total filling factor equal to 1, forces indeed only counter-superflow of different particles to be allowed, resulting in a statistical relevant collection of configurations featured by $\omega_s = 0$ ($\omega_a = -\omega_b$). On the other hand, along the *SCF* channel we still measure long correlation length due to the presence of the particle-hole super-counterflow. In the SCF regime *MC*-simulations show equivalence in the occurrence of winding number of species *A* and *B* $\omega_a = -\omega_b$ whenever ω_a is observed (as the only possible total winding number is $\omega_s = 0$). This forces the statistic of the winding number ω_d to go identically to zero, whenever ω_d is odd. The winding number ω_d distribution is here characterized by the very unique behaviour in which only even winding numbers are allowed (see left panel of FIG. 3.4). This fact can be understood by looking at the system

$$\begin{cases} \omega_s = 0 \\ \omega_d = k \end{cases} \Rightarrow \begin{cases} \omega_a + \omega_b = 0 \\ \omega_d = \omega_a - \omega_b = k \end{cases} \Rightarrow \begin{cases} \omega_a = -\omega_b \\ \omega_d = 2\omega_a = k \end{cases} \tag{3.7}$$

where k is integer by *winding number* definition. System (3.7) has clearly integer solution ω_a and ω_b, if and only if $\omega_d = k$ is even.

Another limit situation that can provide useful information on the quantum phase of the system is when both $\rho_{tot} = 0$ and $\rho_{SCF} = 0$. In this case the system is in the dMI phase as it features short-range correlation and the superfluidity signature is missing in all the possible channels. In particular, the change from a finite ρ_{SCF} to a $\rho_{SCF} = 0$ is the signature of a transition from a SCF phase to a dMI phase. From the simulative point of view this transition is well visible by looking at the distribution of the collected statistics of the $\vec{W}_d$ winding number. In the SCF-dMI transition this distribution undergoes a change passing from the exotic behaviour of the SCF phase

(left panel of FIG. 3.4) to the Dirac-delta-like behaviour of a Mott-Insulator phase (right panel of FIG. 3.4).

In summary, evidence of both transitions concerning the SCF phase (2SF-SCF and SCF-dMI) can be achieved in terms of changes in the superfluidity stiffness (3.5) and (3.6). In Fig. 3.1, solid circles correspond to the 2SF-SCF transition. This transition belong to the (2+1)-XY universality class. Transition points are found using standard finite-size scaling of ρ_{tot} as it can be seen FIG. 3.3 where we plot the scaled total superfluidity as a function of interaction U_{ab}/t for system sizes $L = 8, 16, 24, 36$ and $U/t = 20$. The curves corresponding to different sizes intersect at the critical point $U_{ab}/t = 14.9 \pm 0.1$. Both 2SF and SCF are stable for $U_{ab} < U$.

The empty circles in Fig. 3.1 correspond to the SCF-dMI transition. Upon entering the dMI the system restores the U(1) broken symmetry characterizing the SCF. In order to detect the transition to the dMI phase has been measured the ρ_{SCF} across the transition line and the parameter Δ illustrated in the next section for the detection of the phase separation between the two species. Similarly to the 2SF-dSF transition (see next section for details), we observe an increase of about three orders of magnitude in Δ, while ρ_{SCF} goes to zero, resulting in a shrink in the winding number distribution to delta-like behaviour as seen in FIG. 3.4.

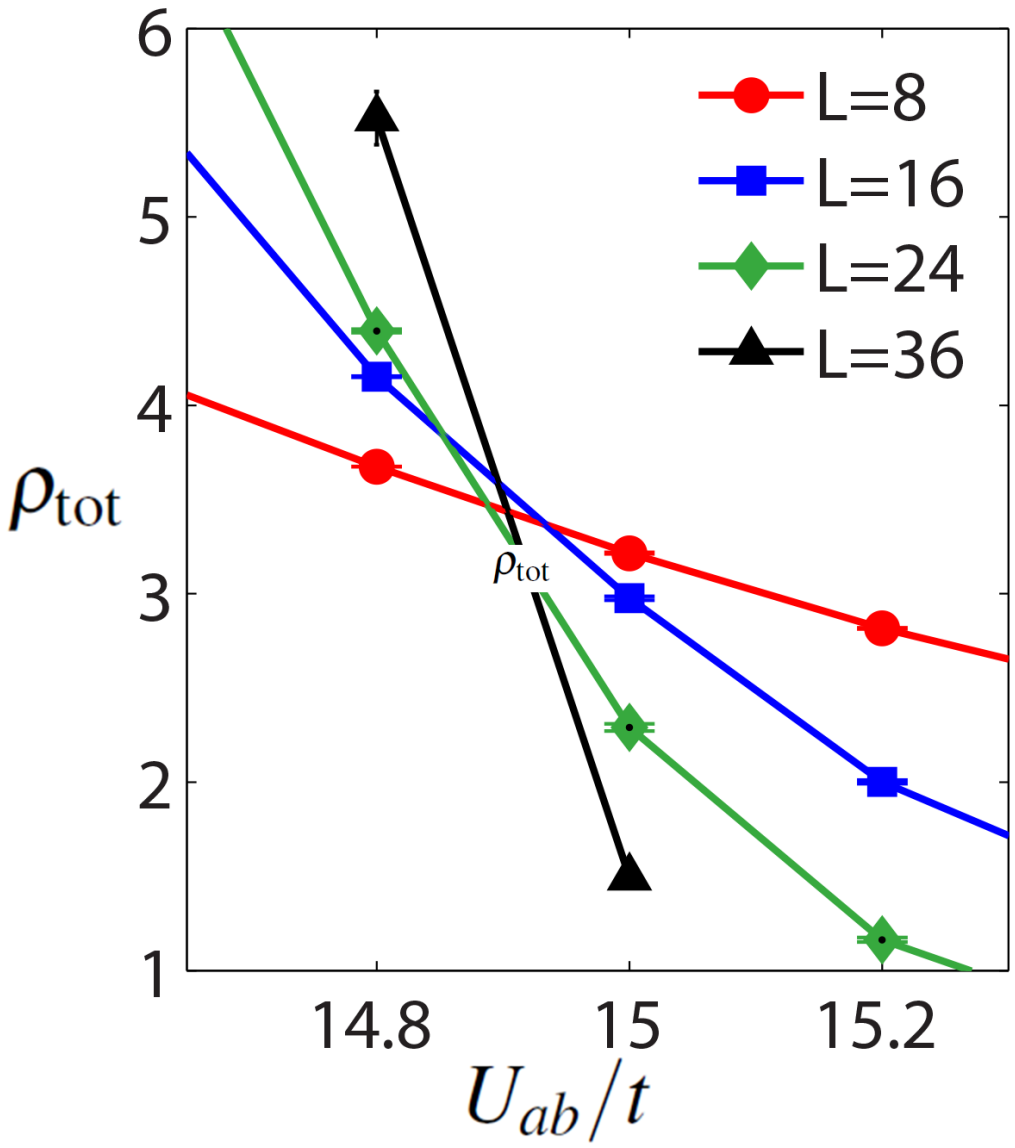

Fig. 3.3 Scaled total superfluidity ρ_{tot} as a function of the inter-species interaction U_{ab}/t for system sizes $L = 8, 16, 24, 36$ and $U/t = 20$. The intersection between curves corresponding to different system sizes gives the transition point for the 2SF-SCF transition.

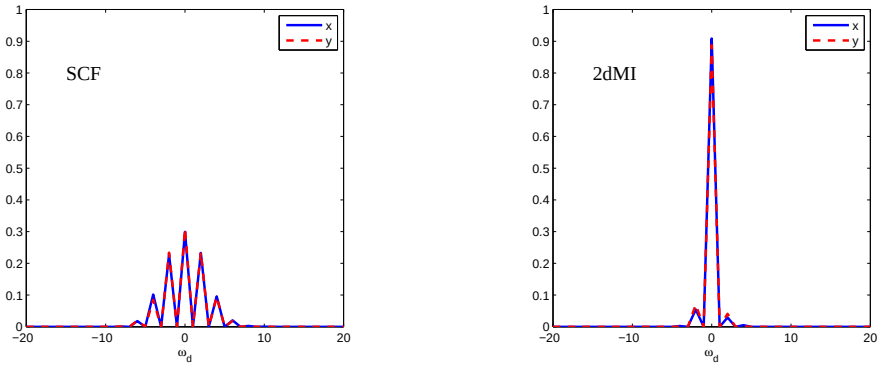

Fig. 3.4 Winding number distribution of $\vec{W}_d$ for the SCF phase ($U/t = 20$, $U_{ab}/t = 19.5$ - Left) and for the dMI phase($U/t = 20$, $U_{ab}/t = 22$ - Right).

SCF phase under population imbalance

We stop now to briefly show in this short subsection how the SCF phase behaves in the presence of population imbalance. As previously shown the SCF phase can be stabilized at $n = 1$ for sufficiently strong values of U/t but $U < U_{ab}$. To perform this study we keep fixed the total number of particles N in order to satisfy the condition $n = 1$, but we tune single-specie chemical potential μ_a and μ_b independently, in order to achieve different population for the two bosons species $N_a \neq N_b$. Here we are interested in showing that SCF still exists with non-zero imbalance although its robustness depends on the latter. In Fig. 3.5 we plot ρ_{SCF} for different values of ratio N_b/N_a. We observe that SCF remains robust also for large population imbalance although the largest superfluid response corresponds to the balanced case.

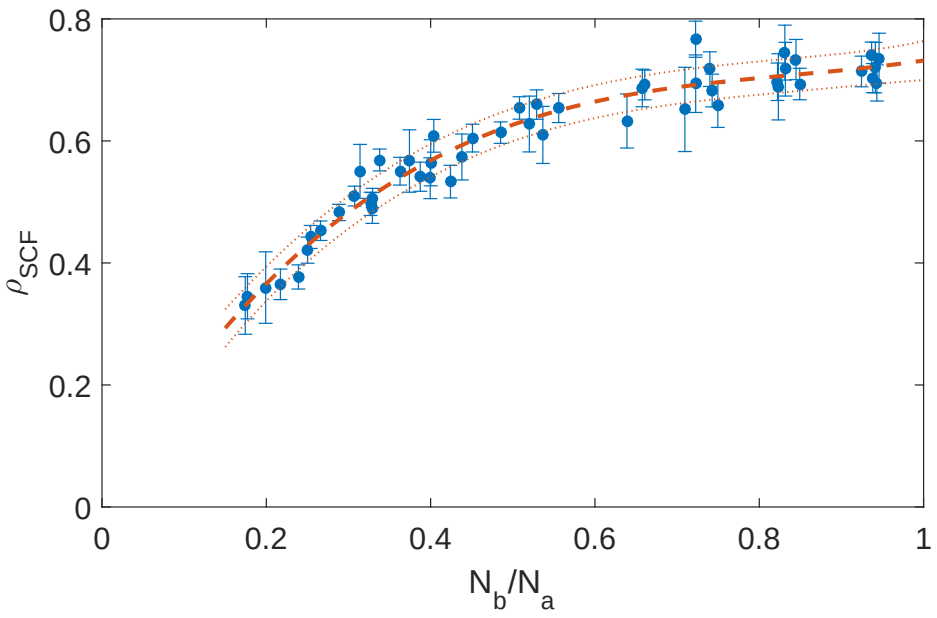

Fig. 3.5 Super-counterfluidity stiffness as a function of N_b/N_a ($U/t = 20$, $U_{ab}/t = 17$ and $L = 24$). Dashed line is a cubic polynomial least-square fit, while dotted lines represent one-σ deviation contours from the fit.

3.2.3 Transition to a demixed phase

According to *Boninsegni et. al.* the phase separation of bosons species in continuous systems can be efficiently detected by the demixing parameter $D = \left[\frac{\langle N_a\rangle - \langle N_b\rangle}{\langle N_a\rangle + \langle N_b\rangle}\right]^2$

described in [66]. In this work we propose an alternative parameter more suitable to lattice systems capable of describing with an high degree of rigourousness the transition to a demixed quantum phase. The demixing parameter we chose for such a task is:

$$\Delta = \frac{1}{M}\sum_i \left[\frac{\langle n_{ai}\rangle - \langle n_{bi}\rangle}{\langle n_{ai}\rangle + \langle n_{bi}\rangle}\right]^2 \tag{3.8}$$

where $\langle n_{ci}\rangle$ is the quantum-thermal average of the density of component $c = a,b$ at site i. Parameter (4.1) is basically a lattice average of the square of the imbalance of the local species' density and is proportional to the expectation value of the single site isospin $\langle \hat{S}_{z_i}\rangle^2$ operator of the underlying $SU(2)$ algebra[1]. Moreover, unlike the parameter D, Δ can also be measured experimentally (see chapter 5 for details) as it measures the average imbalance of the two population among all the lattice sites. Parameters D works well from the theoretical point of view in a simulative background within the grand canonical ensemble picture. In that context, the demixing condition leads to a depopulation of one of the two species, measurable as a global population imbalance by the D parameter. However, depending on the expectation value of the entire species populations $\langle N_a\rangle$ and $\langle N_b\rangle$, parameter D cannot work in a real experimental realization of the twin-species model where the total number of bosons of each species are conserved and the condition $N_a \approx N_b$ is satisfied. Relying on local quantities $\langle n_{ci}\rangle$, demixing parameter Δ (4.1) does not suffer this drawback.

The phase transition between 2SF and dSF (squares in FIG. 3.1) is detected by studying the behavior of the Δ parameter. In Fig. 3.6 we show Δ as a function of U_{ab}/t for $U/t = 5$, $U/t = 10$, $U/t = 15$, circles, squares, triangles respectively. A jump of four orders of magnitude is clearly visible when $U_{ab}/t \sim U/t$ signaling the onset of the demixed phase dSF at the expense of the 2SF. The large increase in Δ underlies a strong evidence of an uniformity change in the species' distribution. Since the two species have been found to lie in a superfluid state both below and above the diagonal of the phase diagram ($\rho_{TOT} \neq 0$ and $\rho_{SCF} \neq 0$), the jump in Δ clearly reveals the presence of a transition to the *demixed superfluid* phase. The same method has been applied to detect the transition from the mixed to the demixed phase in the strong interaction regime, namely, from the SCF phase to the dMI phase. It has

[1]Holstein and Primakoff [77] shown that spin lattice systems are equivalent to lattice boson systems, therefore Hamiltonian (3.1) can be rewritten in terms of isospin operators $\hat{S}_{xi}$, $\hat{S}_{yi}$, and $\hat{S}_{zi}$. The isospin operators along the z pseudo-direction are defined as $\hat{S}_{zi} = \frac{\hat{n}_{ai}-\hat{n}_{bi}}{2}$, their expectation value is therefore proportional to the population imbalance of each lattice site.

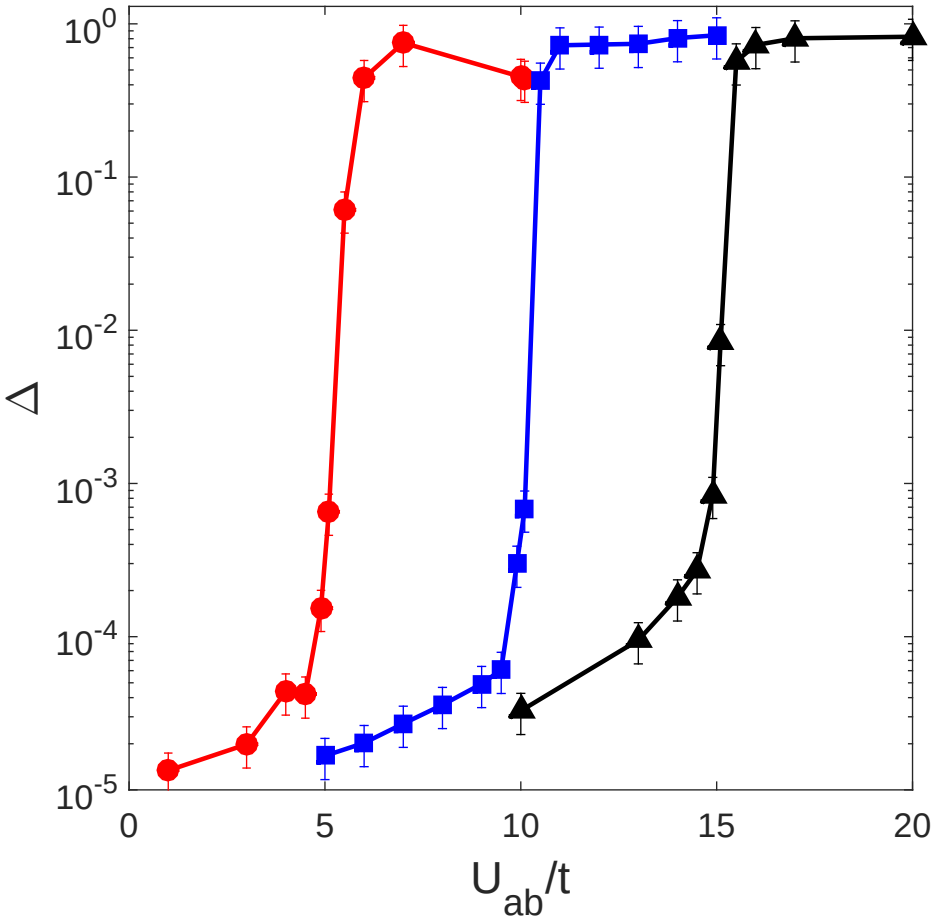

Fig. 3.6 Demixing parameter Δ as function of U_{ab}/t for $U/t = 5, 10, 15$ (circles, squares, triangles respectively) across the 2SF-dSF transition. A jump of four orders of magnitude is clearly visible when $U_{ab}/t \sim U/t$ signaling the onset of the demixed phase dSF at the expense of the 2SF.

been found that even in the strong interaction regime the Δ parameter as a function of U_{ab}/t manifests a step-like behaviour indicating the evidence of a transition to a demixed phase (dMI).

The dSF phase becomes unstable towards a dMI phase upon increasing the intra-species interaction (triangles in FIG. 3.1). We compute the phase boundary by verifying the drop of the SF density of each component for system sizes $L = 8, 16, 24$. While the dSF is characterized by two U(1) broken symmetries over spatially separated regions, in the dMI these symmetries are restored, that is, the

system loses its off-diagonal long range (anisotropic) correlations and becomes insulating. Investigating the details of this phase transition is challenging. Finite-size scaling of the SF stiffness cannot be performed in proximity of demixed regions since the statistics of winding numbers is affected by the topography and the topology of the regions themselves, both of which depend on the initial conditions. If the shape of the demixed regions is connected and restricted to a region that do not cross the periodic boundaries, the computation of the winding numbers returns always zero, leading to the conclusion that the superfluidity in that region is absent. This makes the possibility to distinguish dSF and dMI phases strongly dependent by the topology of the demixed regions. In order to avoid this problem the long-range (short-range) correlation featuring dSF (dMI) phase has been checked through the computation of auxiliary density-density correlators:

$$\xi_c(d) = \langle \hat{\psi}_c^\dagger(\mathbf{r})\hat{\psi}_c(\mathbf{r}')\rangle \ : \ |\mathbf{r}| = r \ and \ |\mathbf{r}'| = r + d \tag{3.9}$$

where $c = a, b$ denotes the species $C = A, B$. If correlators $\xi_c(d)$ are different from zero for large distances d, the species $C = A, B$ features long-range correlation and therefore is superfluid.

3.2.4 Time-Of-Flight Images of the different phases

We compute the momentum distribution for the different quantum phases that arises from the phase diagram of FIG. 3.1. Momentum distribution are computed according to the relation [78]:

$$n_{c\mathbf{k}} = |\phi_{(\mathbf{k})}|^2 \sum_{i,j} e^{i\mathbf{k}(\mathbf{r}_i - \mathbf{r}_j)} \langle c_i^\dagger c_j \rangle \tag{3.10}$$

through the computation of the correlators $\langle c_i^\dagger c_j \rangle$ for species $c = a, b$. Where $\phi_{(\mathbf{k})}$ is the Fourier transform of Wannier function $\phi(\mathbf{r})$, which we do not compute here. If interactions of particles during the flight can be neglected, momentum distribution are proportional to the Time-Of-Flight (TOF). TOF images are those absorption images that arises from interference between particles when the confining potentials are turned off and particles are let to propagate in space; they can be obtained experimentally by standard absorption imaging techniques.

In figure 3.7 we show the computed momentum distributions for species $c = a, b$. TOF profiles along x and y lattice directions within the first Brillouin zone are plotted

in FIG. 3.7 for the 2SF (panel a)), dSF (panel b)), SCF (panel c)) and dMI (panel d)). Note that the TOF image of SCF corresponds to the one of the particle-hole pair. The insets show the corresponding quantum-statistical average of the density of the two components within the lattice. We observe different profiles featuring the different quantum phases with an evident detectable anisotropy of distributions $n_{c\mathbf{k}}$ along the $x-$ and $y-$direction for dSF. This is expected due to the anisotropy of the spatial separation and represents a clear experimental signature of the dSF. On the other hand the TOF image of dMI doesn't reflect anisotropy of spatial separation due to the absence of off-diagonal long range order. In general, we observe no differences in the momentum distributions between the two species. By looking at the momentum distribution of dMI we notice that it features a much broader response in momentum if compared with the other quantum phases where some sort of superfluidity is present. This is basically due to the Heisenberg Uncertainty Principle: in dMI the high localization of particles results in a broader response in momenta, while in SF phases (or counter-superfluid phases like SCF) the high delocalization leads to a sharper and extremely localized response in momentum space.

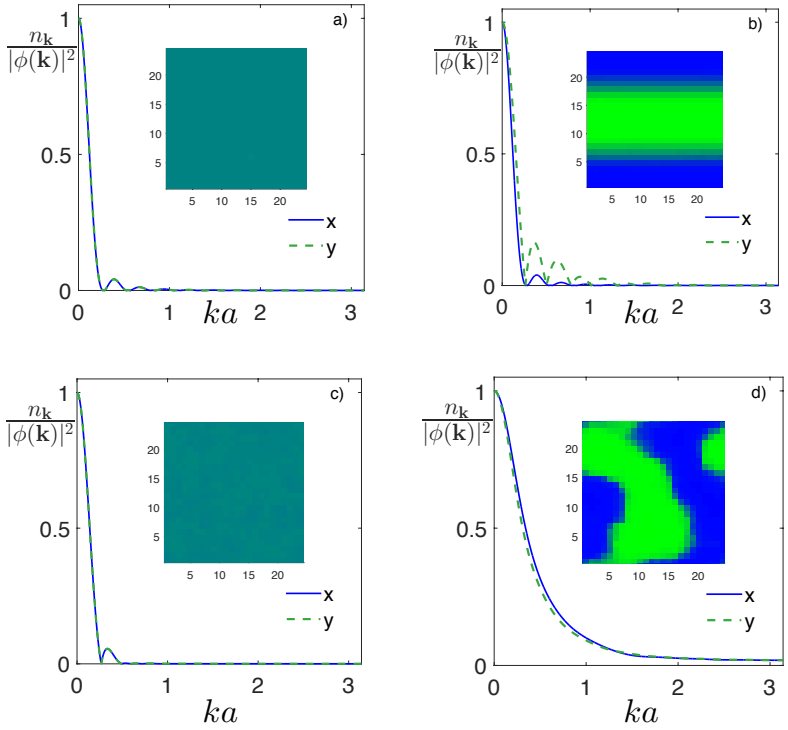

Fig. 3.7 Momentum distributions n_k in the first Brillouin zone for double superfluid 2SF (panel a)), demixed superfluid dSF (panel b)), supercounterflow (panel c)) and demixed Mott-Insulator (panel d)). The insets show the corresponding quantum-statistical average of the density of the two components within the lattice. The demixed phases dSF shows an evident anisotropy along the $x-$ and $y-$direction. This is expected due to the anisotropy of the spatial separation.

3.3 Ground-state phase diagram for non-integer filling

Away from commensurate total filling neither the dMI nor the SCF phase can be stabilized. For non-integer total filling n the phase diagram of model (3.1) becomes much simpler featuring only two quantum phases: a demixed superfluid phase whenever the condition $U_{ab} > U$ is satisfied, and a 2SF phase otherwise. In FIG. 3.8 we plot the ground state phase diagram for non-integer filling. As can be noticed by the diagram itself, non-integer fillings lead to the stabilization of only superfluid phases independently to the strength of the interaction U_{ab}/t and U/t. Furthermore, we will show briefly that, although weakening for $n < 1$, the presence of a transition

to a demixed phase along the diagonal $U_{ab} = U$ seems to have a universal nature and be independent on the filling factor of the system.

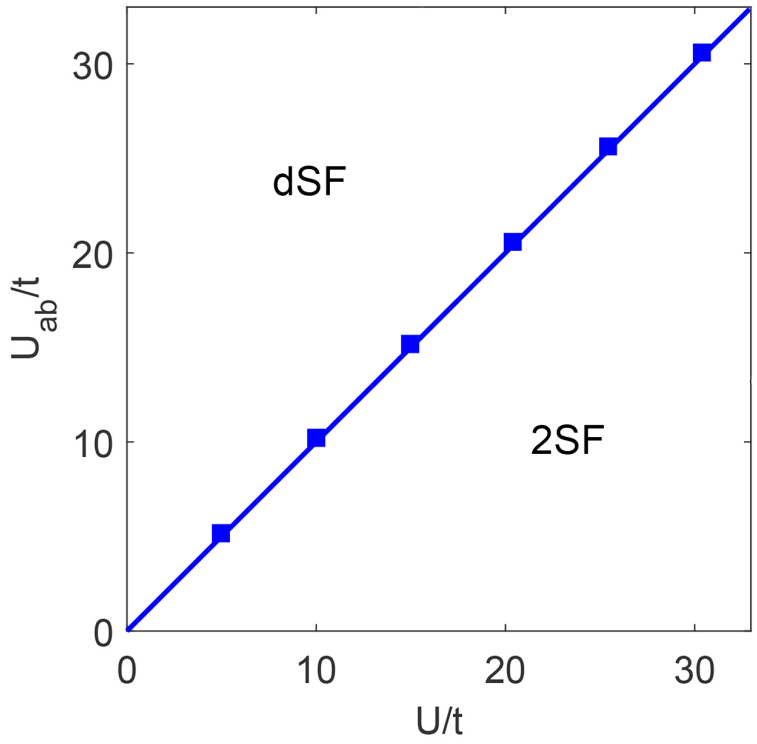

Fig. 3.8 Ground-state phase diagram of twin bosonic species trapped in a uniform optical lattice for non-integer total filling n. Only two phases are stabilized: double superfluid (2SF) and demixed superfluid (dSF).

We now want to show the properties of the dSF phase as a function of the total filling n. We find that demixing effects are still present at $n < 1$ although the spatial separation between the two components A, B is not as pronounced as for $n \geq 1$. This can be seen in Fig. 3.9, where we plot the demixing parameter Δ as a function of n (circles). A substantial drop in the value of Δ is observed for $n < 1$. This is due to the presence of large regions in the lattice where A and B overlap, as shown in the left inset of Fig. 3.9 where we plot the quantum statistical average of the densities of the two species at $n = 0.3$. This overlap region results from enhanced hopping of particles which is responsible for larger fluctuations of $\langle n_{a,b} \rangle$. For comparison, in the right inset of Fig. 3.9, we show the species densities at $n = 1.3$. A net spatial separation between A and B is observed. Despite this substantial drop in the value of Δ for $n < 1$, we find that Δ is still a good indicator that demixing has occurred.

Indeed, Δ values in the 2SF phase (triangles in Fig. 3.9) are still orders of magnitude smaller than in the dSF phase. These results suggest that demixing effects can be observed in the presence of an external harmonic trap where a variation of n within the trap is present.

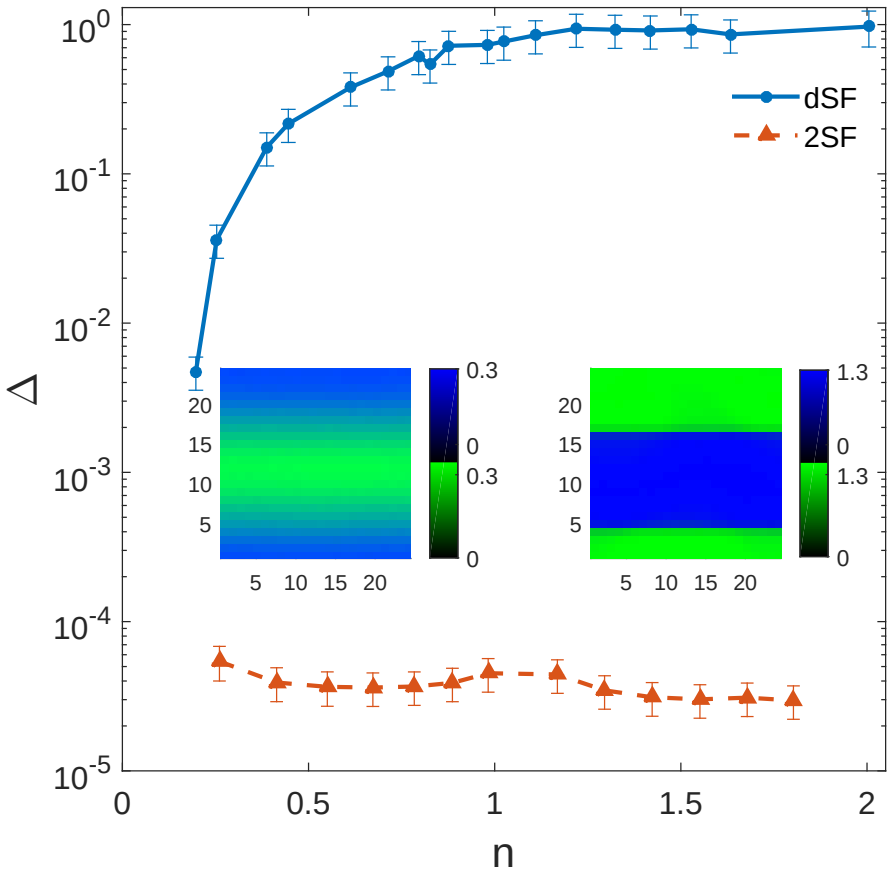

Fig. 3.9 Δ parameter as a function of total filling n for dSF (circles, $U/t = 10$, $U_{ab}/t = 15$ and $L = 24$) and 2SF (triangles, $U/t = 10$, $U_{ab}/t = 7$ and $L = 24$) phases. Insets represent the average densities of the two components for $n = 0.3$ (left), $n = 1.3$ (right).

3.4 Harmonically Trapped system

In order to provide further information for the case of non-commensurate filling, we move now to analyze the system in non-homogeneous conditions in the presence of a harmonic trap. This also allows to simulate in a more realistic scenario, closer to

real experimental realizations, giving us the opportunity to improve our grasp on the experimental realizations of real finite-size systems.

In the following we consider balanced populations ($N_a = N_b$). We basically show that even in the trapped case, demixed phases appears in both strong and weak interaction regimes whenever $U_{ab} > U$. Furthermore, in the strong interaction regime (corresponding to the SCF and dMI regions of FIG. 3.1) due to presence of a radially variable filling factor, spatial shell structures can arise. The presence of a harmonic confinement induces a variable filling profile in the lattice, the profile manifests the same circular symmetry of the trap and features a decreasing filling factor moving radially outward from the center of the trap (center of the lattice). If the interactions are strong enough, insulating phases can be stabilized in proximity of integer local-filling factor, this lead to the appearance of spatial shell structures where shell of insulating phases (dMI or SCF) intercalates shell of superfluids phases (2SF or dSF).

In the presence of a harmonic potential, the chemical potential of species $c = a, b$, occurring in the Hamiltonian (3.1) transforms according to

$$\mu_{ci} = \mu_c - \omega_H \vec{r}_i^{\,2} \tag{3.11}$$

where ω_H is the strength of the harmonic trap (expressed in unit of the hopping amplitude t), and $\vec{r}_i$ the position vector of lattice site i. As anticipated above, this leads to a variable local filling factor $n_{\vec{r}}$ through the lattice, allowing us to explore in a more complete way the influence of the filling variation on the phase diagram of the system. As we showed in the section 3.3, demixing persists away from filling $n = 1$, as long as $U_{ab} > U$. This is even more evident in the trapped case. In figure 3.10 we show the density map of a demixed superfluid in which a harmonic confinement forces the mixture to occupy only the central regions of the lattice with radially decreasing filling. In the right panel of figure 3.10 we display the demixed density profiles of the two species for a radial section perpendicular to the interface between the two superfluids. It is evident that demixing persists at any value of the radial coordinate and for different values of the filling. It is worth noticing that, as predicted in [72] for a mixture of two Bose-Einstein condensates in a harmonic trap, the overlap energy is minimized when the boundary is a straight line.

For higher values of the inter- and intra-species potentials, within the SCF region of the phase diagram (FIG. 3.1), we observe the presence of the well-known spatial

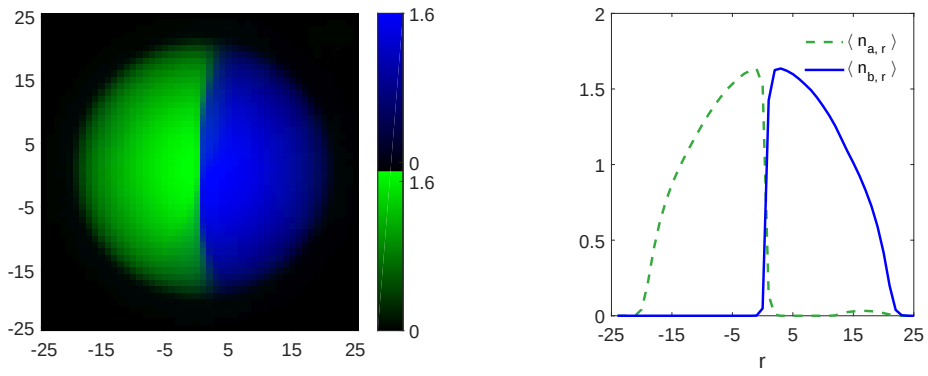

Fig. 3.10 dSF phase ($U/t = 10$, $U_{ab}/t = 15$, $N_a = 639$, $N_b = 641$) confined in a Harmonic trap ($\omega_H/t = 0.12$). Left-Panel shows density maps for both species over the entire trap. Right-Panel shows a radial section of density maps, perpendicular to the boundary.

shell structure [79–81]. For increasing total number of particles in the system, we observe a spatial structure in which shells of 2SF phase intercalate SCF-phase shells, depending on the value of the local filling factor. The different panels of Fig. 3.11 show density profiles for different values of $N = N_a + N_b$ but same parameters $U/t = 20$, $U_{ab}/t = 17$ and $\omega_H/t = 0.12$. From top to bottom, radial profiles of total density with increasing boson number are displayed. By increasing N, the spatial shell structure appears, revealing the alternate shells of the two phases, with the SCF characterized by a density plateau. The plateau are due to the incompressible character of the Mott-Insulator-like phases (SCF is a global Mott-Insulator). We do not observe a plateau at $n = 2$ in agreement with reference [82] where the formation of SCF phase at double-commensurate filling is observed for larger values of U/t.

Always in the strong interaction regime, but for values of inter-species interaction stronger than intra-species one, the system exhibts spatial shell structure featuring evidence of tiny shell of dMI phases intercalating phases of dSF. Again, the incompressible character of dMI phases is revealed by the presence of density plateau in the total density profile for integer local-filling. This can be noticed in FIG. 3.12 where we plot density map (left panel) and density profile (right panel) along the radial direction for a mixture stabilized for $U/t = 20$, $U_{ab}/t = 24$ trapped with a harmonic potential strength of $\omega_H/t = 0.12$. The roughness and irregularities of the demixed regions can be understood in terms of the presence of the dMI phase. High values of interactions U/t and U_{ab}/t play a prominent role in determining the final shape of demixed regions both in the homogeneous and in the trapped case. If

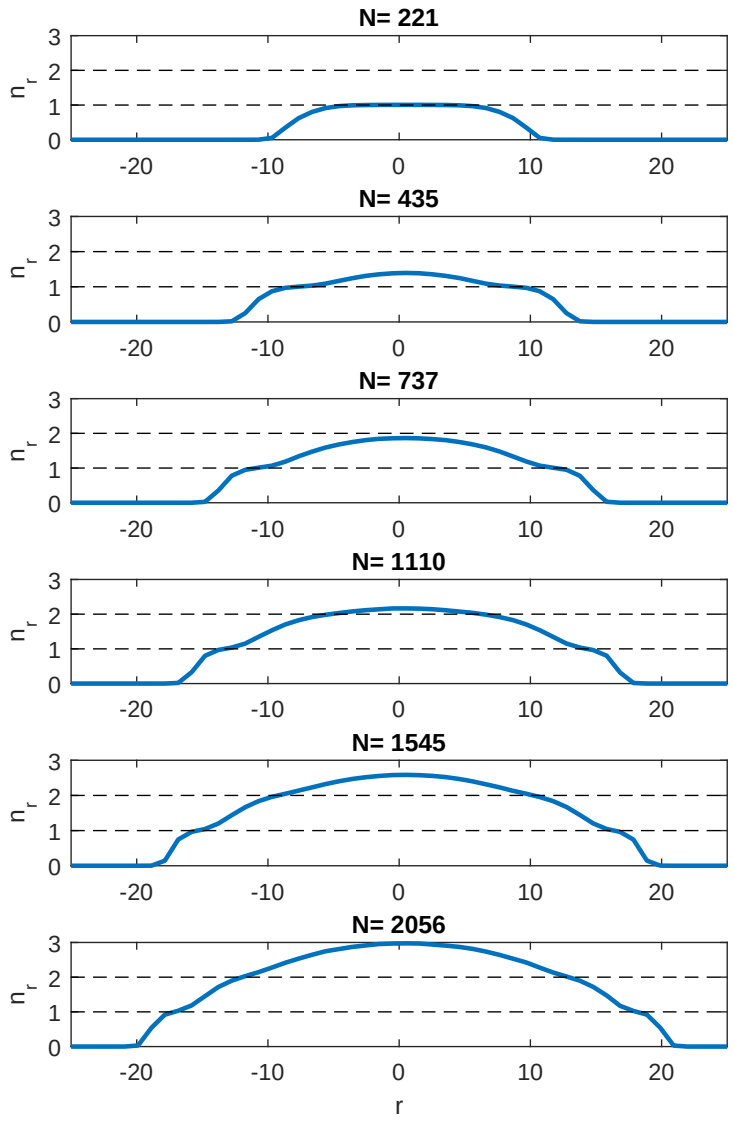

Fig. 3.11 Radial profiles of total density n_r for increasing number of particles at $U/t = 20$, $U_{ab}/t = 17$ and $\omega_H/t = 0.12$.

the conditions to stabilize a Mott-Insulator phase are satisfied, the high-energy cost and the reduced mobility (reduced hopping) featuring this kind of phases freeze the density distributions to a configuration really close to energy minimum but maybe not exactly the absolute one.

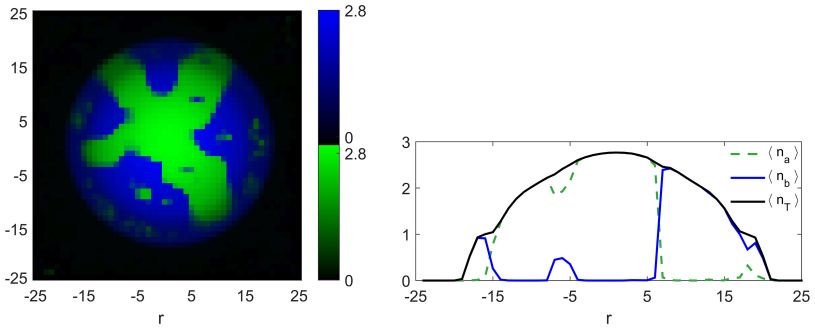

Fig. 3.12 Density maps (left panel) and density profile along the x axis ($y = 0$) for a harmonically trapped mixture simulated at $U/t = 20$, $U_{ab}/t = 24$ and $\omega_H/t = 0.12$.

3.4.1 TOF images in the trapped case

By computing correlators $\langle c_i^\dagger c_j \rangle$ for both species $c = a, b$, according to the relation (3.10), we obtained the momentum distribution of the two boson species also for the harmonically trapped case. In FIG. 3.13 we show the computed TOF images and associated density maps for three different interaction regimes. The different panels of FIG. 3.13 show the density maps (upper pannel) of species A (green) and B (blue) and TOF images of species A (central panel, green) and species B (lower panel, blue). Leftmost panels shows a mixture featuring a spatial shell structure with a plateau of SCF surrounded by a central and an outer shell of 2SF. The corresponding profile of this case is shown in the lower panel of FIG. 3.13, in this case $U/t = 20$, $U_{ab}/t = 17$ and $\omega_H/t = 0.12$. Central panels show a trapped mixture in a 2SF phase ($U/t = 10$, $U_{ab}/t = 7$ and $\omega_H/t = 0.03$) while the righmost case is a situation in wich dSF phase is stabilezed in the trap ($U/t = 10$, $U_{ab}/t = 15$ and $\omega_H/t = 0.03$).

As can be seen in FIG. 3.13, also in the trapped case the TOF images in which SCF and/or 2SF are stabilized (left and central column) exhibit similar behaviour due their isotropic superfluid character. The circular symmetry of the momentum distributions is due to the circular symmetry of the trap. When the demixing effect take place, we see that even in the trapped case a strong anisotropy in momentum distribution appears along the direction of maximum confinement. This is mainly due to the presence of the “hard-wall” between the two bosons species, that lead to interference between propagating and back-propagating matter waves of each species field along that direction of confinement. This provide by itself an interesting feature as it would allow to probe the presence of such a phase in real experiments.

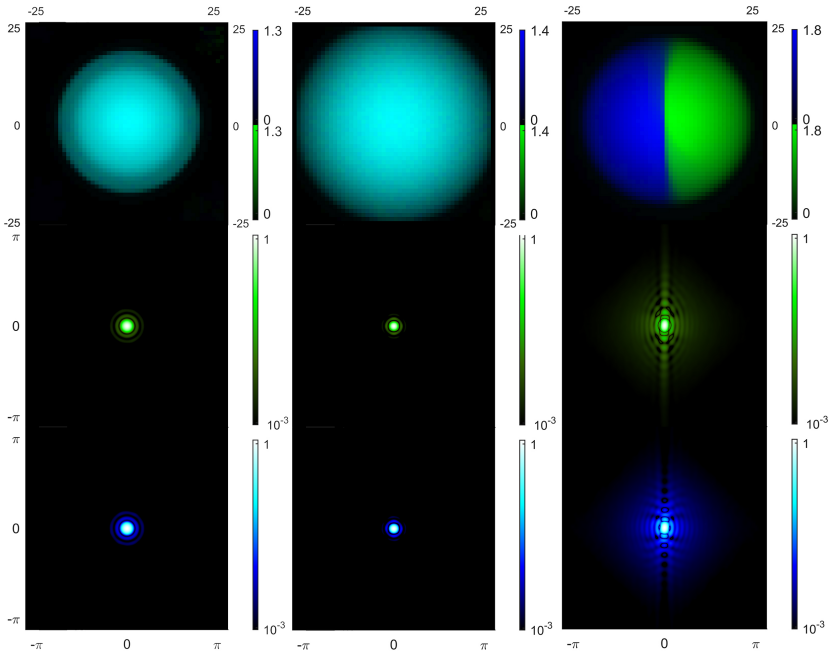

Fig. 3.13 Density maps (upper panels) of specie A (green) and B (blue) and computed TOF images of species A (green-central panels) and B (blue-lower panels) for three different interaction regimes. Left column: 2SF/SCF spatial shell structure for $U/t = 20$, $U_{ab}/t = 17$ and $\omega_H/t = 0.12$. Central column: 2SF trapped phase for $U/t = 10$, $U_{ab}/t = 7$ and $\omega_H/t = 0.03$. Right column: dSF trapped phase for $U/t = 10$, $U_{ab}/t = 15$ and $\omega_H/t = 0.03$.

Chapter 4

Phase Separation at finite Temperature

In this chapter we analyze the twin-species model at finite temperature paying particular attention to the influence of temperature fluctuations on phase separation and demixed phases. The results and discussions contained in this chapter have mainly been published in the paper [56]. As explained in chapter 2, the worm algorithm quantum Monte Carlo, exploiting its imaginary-time picture, allows us to explore quantum-thermal statistical averages of different physical quantities capable of describing our lattice-bosons system. By choosing an inverse-temperature β sufficiently large (typically $\beta = L/t$), one can explore the properties of the ground-state of the system. On the other hand, by simulating at smaller βs it is possible to estimates the expectation value of different physical observable O (described by the operator $\hat{O}$) that are proportional to the quantum-thermal average: $\langle e^{-\beta\hat{H}}\hat{O}\rangle$, that is the definition of "*expectation value*" of operator $\hat{O}$ in its quantum-statistical-mechanical formulation.

By simulating at finite temperature, we are interested in exploring the role of the temperature in the stabilization of demixed phases and quantifying how temperature fluctuations affect the demixed phases observed in the ground-state. What we find is that temperature fluctuation tend to compete with and eventually destroy demixing. This reveals interesting thermometric properties that can be exploited experimentally in order to achieve information on the temperature of the system. In the next chapter we will carry on this idea and we will show how it is possible to exploit the demixing

parameter described in the section 3.2.3 to measure the temperature in ultra-cold mixtures (see chapter 5 for details).

To perform this analysis we work at finite temperature in both the weak (WI) and strong interaction regimes (SI). We refer to weak (strong) interaction that range of U/t, U_{ab}/t where 2SF/dSF (SCF/dMI) phases can be stabilized in the ground state of the homogeneous twin-species model at $n = 1$. Within the weak interaction regime, we initially work at integer fillings and periodic boundary conditions (homogeneous case). We then move to consider the trapped case, studying the appearance of the spatial-shell structures, the relation between demixing and Time-Of-Flight images at finite temperature, and the interplay between temperature effects and demixing properties. Finally, we repeat the study in the strong-interacting regime for the trapped case, showing that, even within this scenario the thermometric properties of Δ are preserved.

4.1 Temperature-dependent mixing in a homogeneous case

We start our analysis at finite temperature in the homogeneous case. We work with periodic boundary conditions and integer fillings considering in particular, $n = 1$ and $n = 2$. The two cases correspond to $N_a + N_b = L^2$ and $N_a + N_b = 2L^2$, respectively, where L is the linear size of the lattice (in unit of the lattice step a). Also in this case we consider the case of twin-species model described so far.

As we have shown in the previous chapter, the ground-state ($T = 0$) phase diagram of a mixture of twin bosonic species trapped in an optical lattice, at total filling $n = 1$, features a demixed superfluid phase (dSF) and a demixed Mott-insulator (dMI) phase when the interspecies interaction becomes greater than the intraspecies repulsion, and a double-superfluid phase (2SF) or a supercounterflow (SCF) otherwise (see FIG. 3.1 in chapter 3).

To study the effect of temperature fluctuations, we first focus on the transition 2SF-dSF, since this can be observed for any choice of the filling factor [55], while the transition from dMI-SCF requires an integer value of the filling factor.

In order to quantify demixing effects, we compute the parameter Δ defined in the previous chapter (see section 3.2.3). For the sake of clearness we report here the definition of the parameter

$$\Delta = \frac{1}{M}\sum_i \left[\frac{\langle n_{ai}\rangle - \langle n_{bi}\rangle}{\langle n_{ai}\rangle + \langle n_{bi}\rangle}\right]^2, \tag{4.1}$$

where the sum runs over all the $M = L^2$ lattice sites; Δ ranges from 0, if all sites are equally populated, to 1, for complete demixing.

4.1.1 Total filling $n = 1$

We initially start our study at total filling $n = 1$. We simulated the system for different temperatures, and different values of the inter-species interaction U_{ab}/t. We found that temperature fluctuations tend to destroy the order brought by the demixing effect, leaving remarkable signatures of it in the behaviour of the Δ parameter.

In FIG. 4.1 we plot Δ as a function of inter-species interaction U_{ab}/t for different temperatures in the range $0.042 < T/t < 1$ and at fixed $U/t = 10$. At lower temperatures, a step-like increase in the value of the demixing parameter Δ signals the onset of strong demixing in the system. As the temperature is increased, thermal fluctuations become more prominent and the mixing of the two components is restored even for $U_{ab} > U$. Δ curves and their uncertainties in FIG. 4.1 are obtained by averaging multiple-run QMC simulations with different random-generators seeds and different initial conditions. The observed fluctuations are essentially due to transitions between equally stable states.

FIG. 4.2 shows Δ as a function of T/t for different values of inter-species interaction U_{ab}/t and at fixed $U/t = 10$. The main plot, which refers to the dSF phase, shows a pronounced dependence of Δ on temperature: a drop in Δ of three order of magnitudes within a relatively small range of temperatures. On the other hand, for the 2SF phase (inset of FIG. 4.2), Δ remains approximately of the same order of magnitude (and orders of magnitude smaller than in the dSF phase) with increasing T. The strong dependence of Δ on T/t displayed in FIG. 4.2 supports its application as a thermometer. The idea to exploit demixing as a mean to measure the temperature of the system can be practically realized by an experimental estimate of the Δ parameter (see chapter 5 for details).

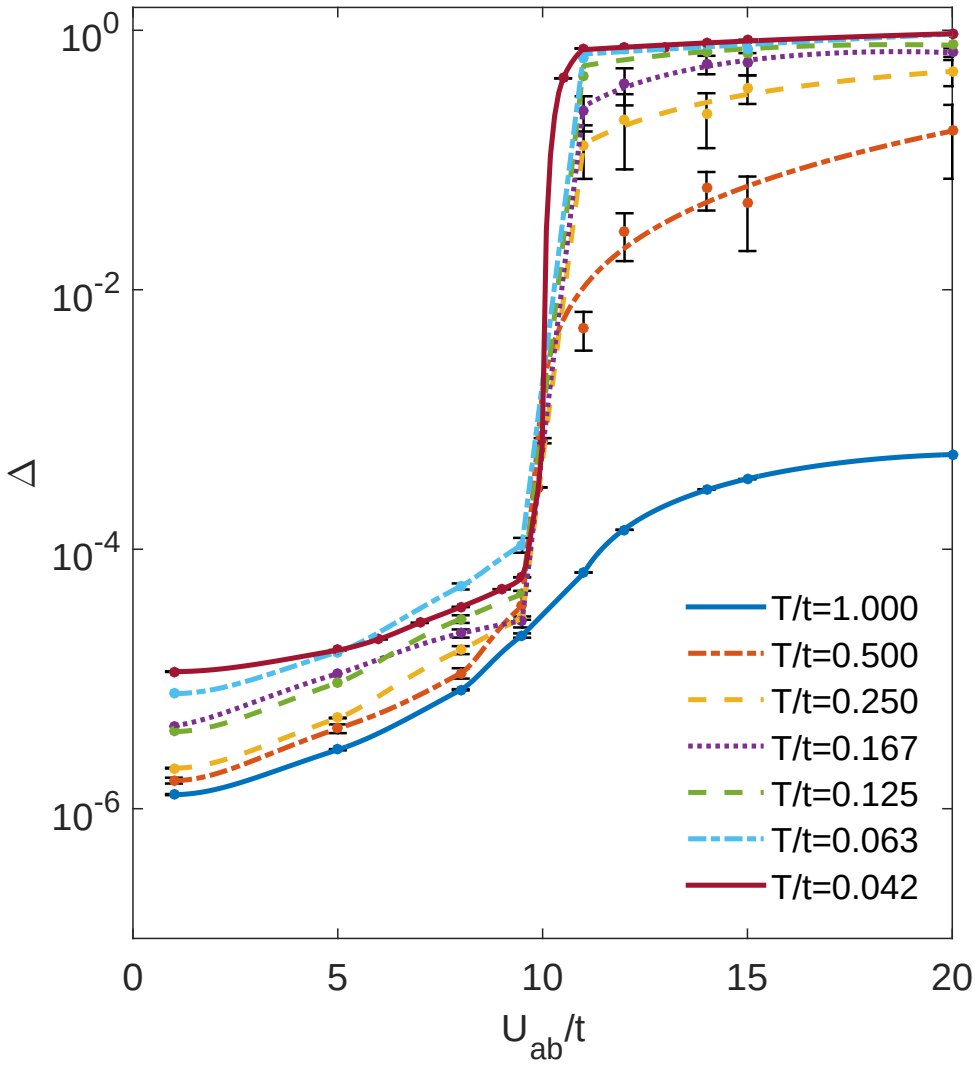

Fig. 4.1 Parameter Δ as a function of U_{ab}/t at different temperatures T/t at total filling $n = 1$ (lines are guidelines). Simulations performed for $U/t = 10$ along 2SF/dSF phase transition.

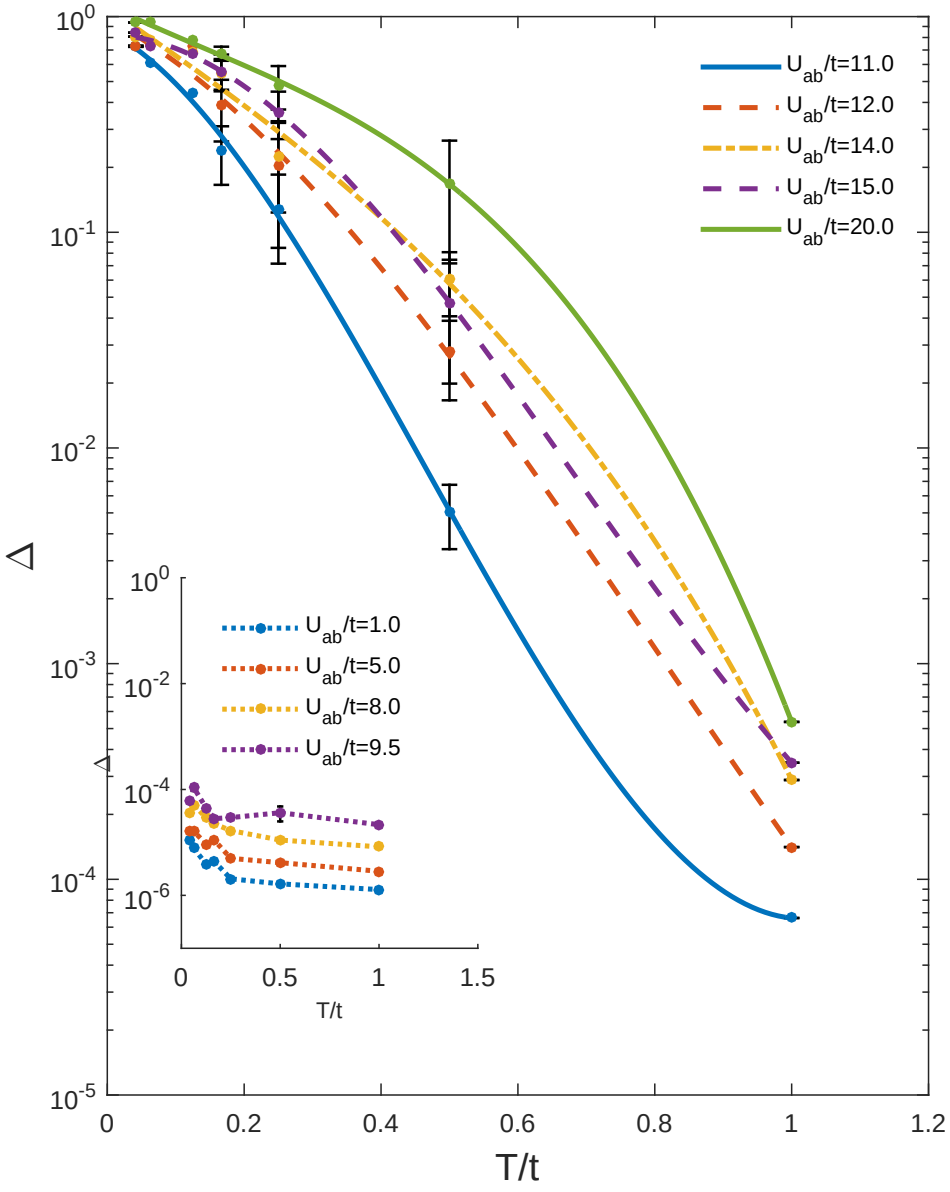

Fig. 4.2 Δ-parameter as a function of temperature T/t for different values of the inter-species potential U_{ab} (lines are guidelines). Simulations performed for $U = 10$, $n = 1$ along 2SF/dSF phase transition.

4.1.2 Total filling $n = 2$

For total filling factor $n = 2$, the larger energy penalty associated with the overlap between components leads, in general, to a more evident demixing [55] characterized by a neat spatial separation between the two species. This robustness against miscibility results in a stronger robustness against temperature fluctuations than at lower filling factors.

In FIG. 4.3 we plot Δ for $n = 2$ as a function of U_{ab}/t for the same interaction ($U/t = 10$) as in FIG. 4.1 but a larger temperature range. At $n = 2$ parameter Δ manifests an apparent similar behaviour against temperature with respect to the one at $n = 1$. However, a comparison with FIG. 4.1 shows that, at $n = 2$, a significant increase in temperatures is needed in order to destroy demixing. This is further demonstrated in the density maps of FIG. 4.4. FIG. 4.4 shows quantum-statistical average of computed occupation number per lattice site for $n = 1$ (left) and $n = 2$ (right) performed under same interactions and temperature conditions ($U/t = 10$, $U_{ab}/t = 14$ and $T/t = 0.5$).

In FIG. 4.5 we plotted Δ as a function of T/t for $n = 2$ and $U_{ab} > U$. By comparing FIG. 4.2 and 4.5 it is possible to appreciate the strong dependence of Δ with the temperature. This suggests that the presence of temperature fluctuations tends to destroy the spatial demixing of the two species and, how the strength of the inter-species interaction U_{ab} plays an important role in contrasting this effect. In both figures it can be easily noticed as a stronger repulsion between the two species (U_{ab}) leads to a slower decrease of $\Delta_{(T)}$ curves. On the other hand, this temperature-dependent mixing effect seems to be retarded in case of higher filling.

This behavior can be understood by observing that, for $U_{ab} > U$, increasing the filling factor further inhibits the start of the mixing process of the two components. In this sense, the minimal mixing action consists in displacing a single boson a (b) in the domain of components B (A). For $n = 2$, the heuristic calculation of the free-energy cost for creating a double pair ab gives $\Delta F = 2(U_{ab} - U)(n-1) - Tk_B\ln(L^4/4)$. The mixing temperature is found to be $k_BT = 2(U_{ab} - U)/\ln(L^4/4)$. For $n = 1$, the mixing process begins with the formation of a single pair ab and a hole. This entails $\Delta F = U_{ab} - Tk_B\ln(L^4/4)$ and $k_BT = U_{ab}/\ln(L^4/4)$. In both cases, using the parameter values of 4.5 and 4.5 gives $k_BT/t \sim 1$ in agreement with numerical results. The dependence on the lattice size L reflects the finite-size character of our

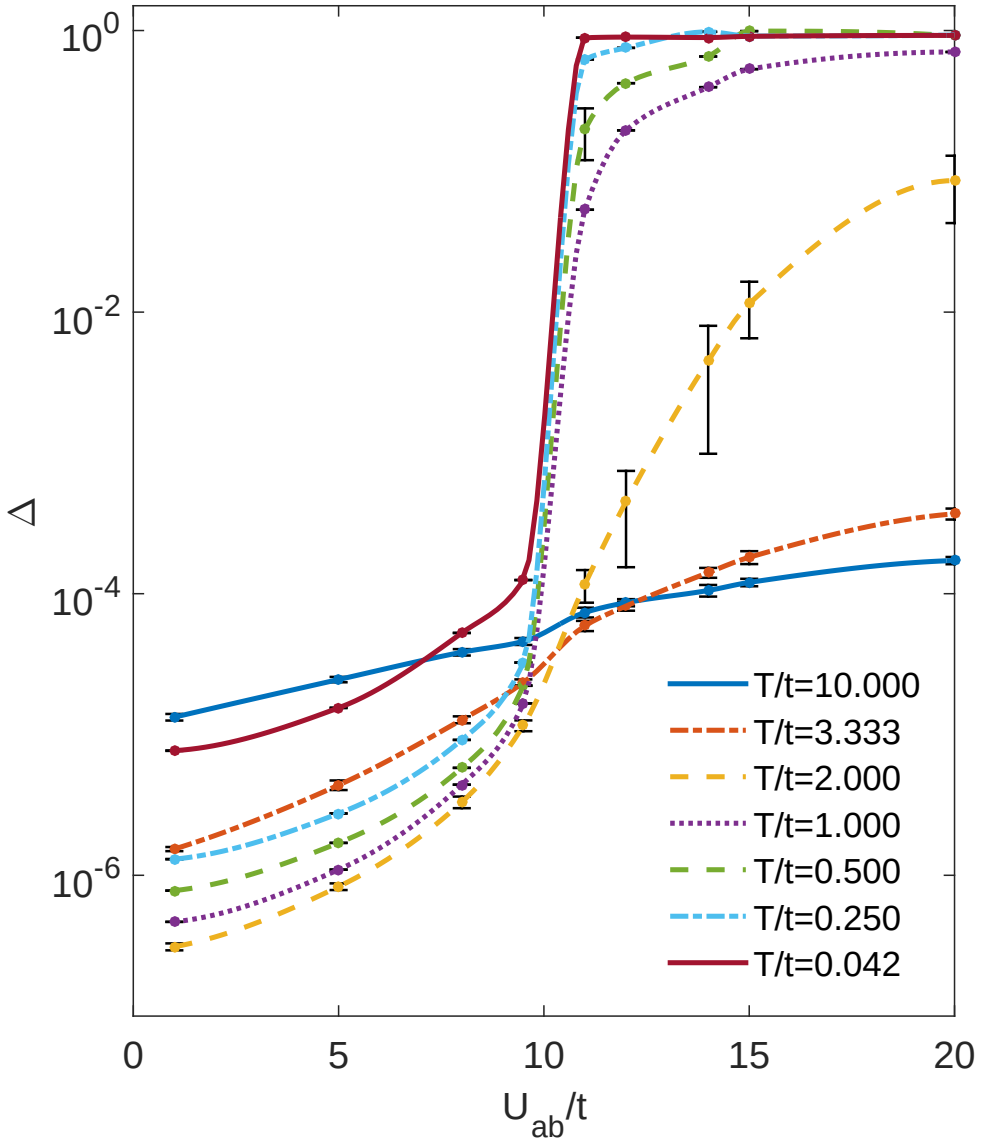

Fig. 4.3 Δ-parameter as a function of U_{ab} at different temperatures T/t at total filling $n = 2$ (lines are guidelines). Simulations performed for $U = 10$ along 2SF/dSF phase transition.

model. The temperature at which the first pairs *ab* crop up is proportional to U_{ab}, thus confirming the inhibition of the mixing effect for increasing U_{ab}.

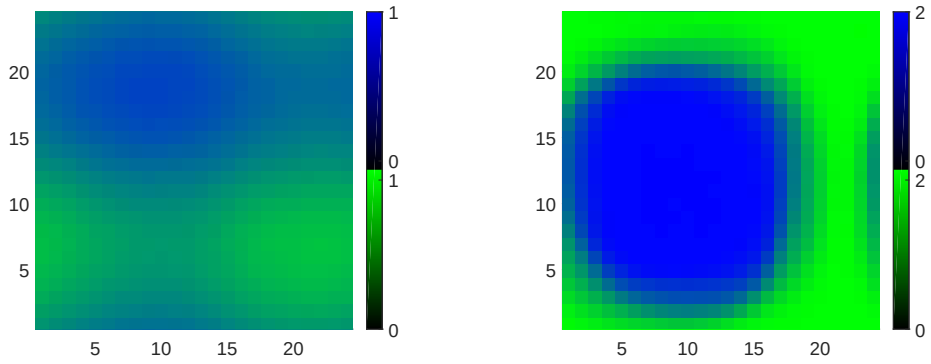

Fig. 4.4 Density maps for a dSF phase at $U/t = 10$, $U_{ab}/t = 14$ and $T/t = 0.5$ computed at $n = 1$ (Left-Panel) and $n = 2$ (Right-Panel).

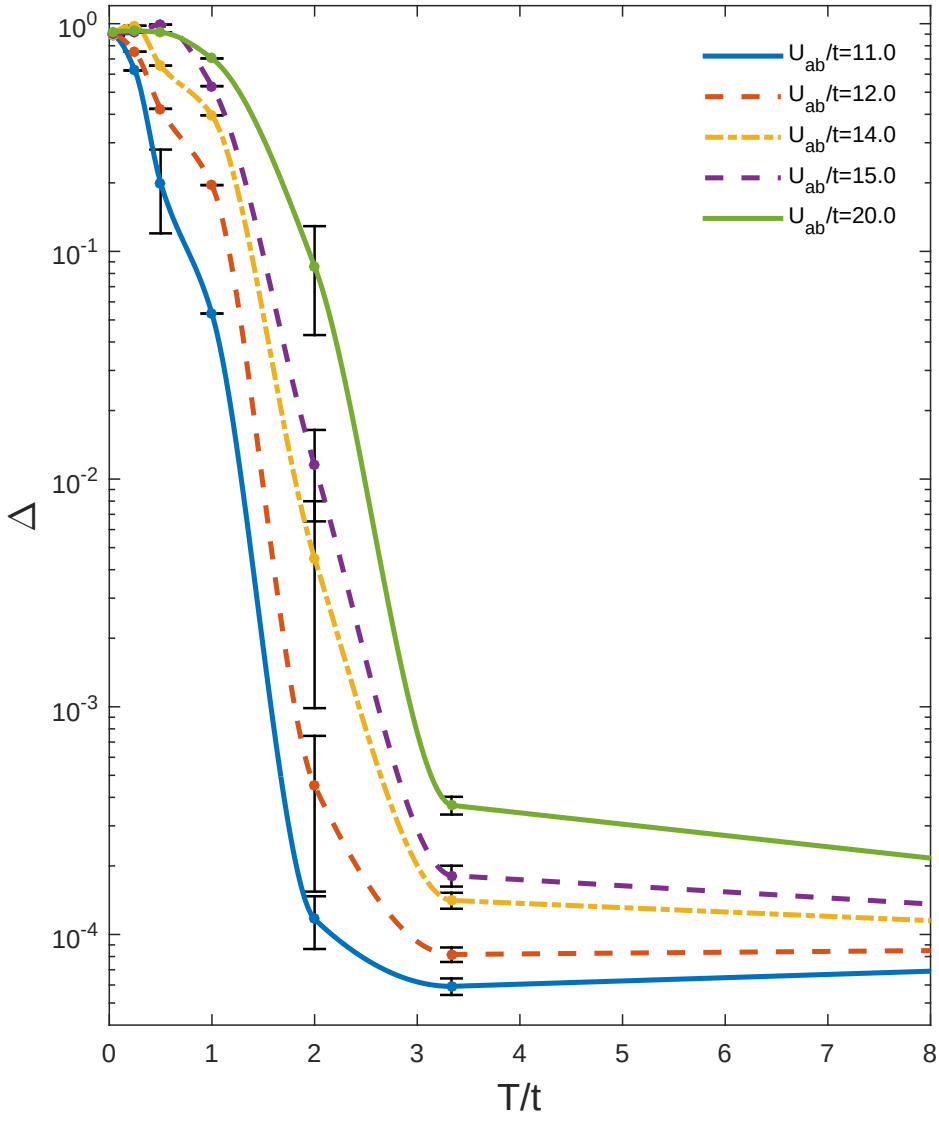

Fig. 4.5 Δ-parameter as a function of T/t for different values of $U_{ab}/t > U$ $(U/t = 10)$ at total filling $n = 2$ (lines are guidelines).

4.2 Temperature-dependent mixing in a trap

In order to consider a more general and realistic scenario, we extend our investigation to a generic filling factor by relaxing the homogeneity assumption and study the system in a harmonic trap. In the presence of a harmonic potential, the chemical potential of species $c = a, b$, transforms according to

$$\mu_{ci} = \mu_c - \omega_H \vec{r}_i^{\,2} \tag{4.2}$$

where ω_H is the strength of the harmonic trap (expressed in unit of the hopping amplitude t), and $\vec{r}_i$ the position vector of lattice site i. This leads to a space-dependent local filling factor $n_{\vec{r}}$ through the lattice, allowing us to explore in a more complete way the influence of the temperature on the interplay between mixed/demixed phases in condition of generic filling factors.

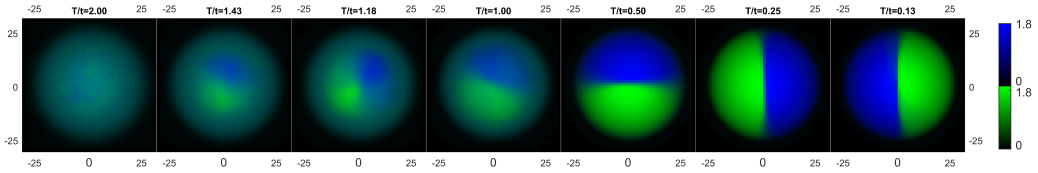

Fig. 4.6 Density maps for decreasing temperature (left to right). The mixture ($U/t = 10$, $U_{ab}/t = 15$) is trapped in a harmonic potential of strength $\omega_H/t = 0.03$.

As shown in chapter 3, the presence of the demixing effect is not affected a priori by the application of a harmonic potential as far as the condition $U_{ab} > U$ is satisfied. At sufficiently low temperatures the demixing effect in the trap manifests itself through the occurrence of a sharp and straight boundary between the two species (see FIG. 3.10 in chapter 3). This represents the minimum-energy configuration for a demixed system in a trap, as originally predicted by [72] for continuous systems.

We consider then a mixture trapped in a harmonic potential for different temperatures. In general, we see that even in the trapped case temperature fluctuations tend to destroy the demixing effect. This phenomena is well visible in Fig. 4.9 where we plotted from left to right several density maps for decreasing value of the temperature ($U/t = 10$,$U_{ab}/t = 15$,$\omega_H/t = 0.03$ and $N \approx 1670$). It can be easily seen as increasing temperatures lead to a progressive destruction of the spatial demixing between the two species.

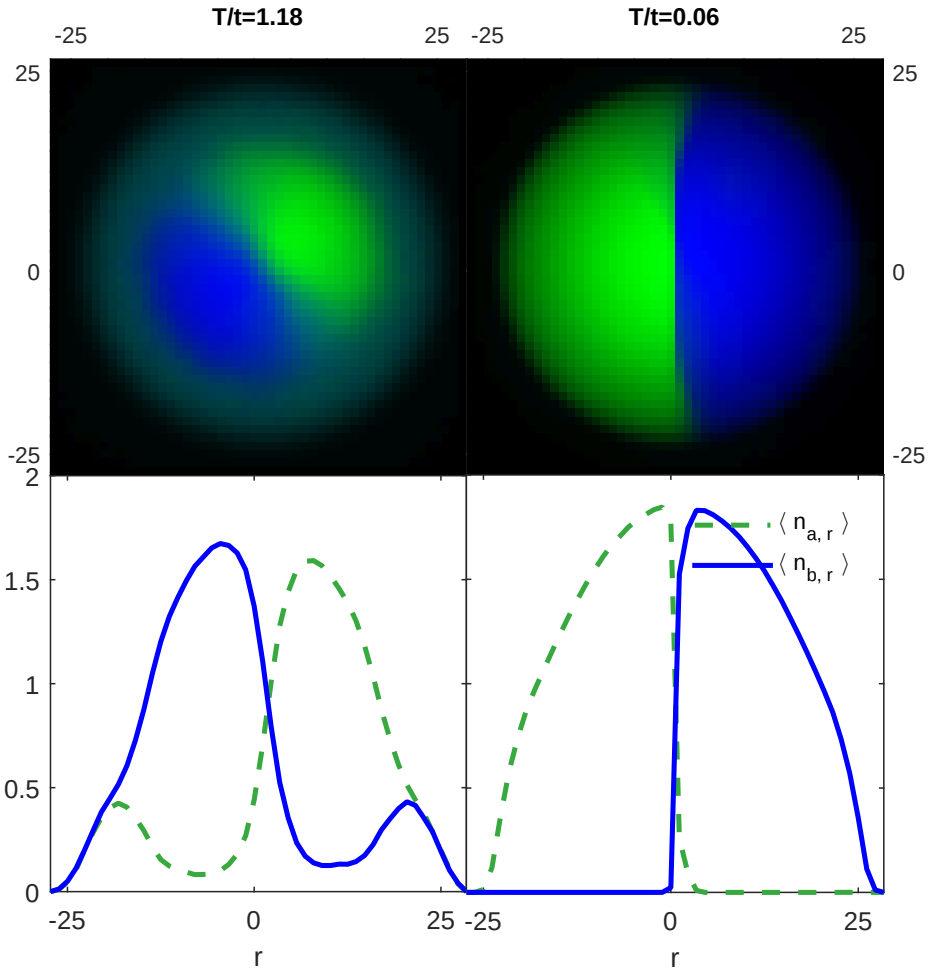

Fig. 4.7 Density maps (first row) and their section at $y = L/2$ along x-direction (second row) for temperatures $T/t = 1.00$ (left column) and $T/t = 0.06$ (right column). The mixture ($U/t = 10$, $U_{ab}/t = 15$) is trapped in a harmonic potential of strength $\omega_H/t = 0.03$.

For intermediate temperatures this effect give rise to spatial shell structures (see FIG. 4.9 and 4.7) in which a central demixed phase (dSF) is surrounded by a shell of mixed phase (2SF). In the first row of FIG. 4.9 it is well visible that the temperature-induced mixing effect first appears where the density is lower (that is in the outer shell) and in the proximity of the boundary separating the two species. Such an effect is due to the larger entropy associated with demixing in these regions. For sufficiently large temperatures we detected the presence of a third surrounding shell of a Normal-Fluid (NF) phase. As expected, the thickness of the NF shell increases for increasing temperatures (see below section 4.2.2 for details).

The fact that we find a demixed phase at the center of the trap where the local filling is higher, and a mixed phase in the surrounding shell where the local filling is lower, confirms what we have found in the homogeneous case, in which higher fillings (center of the trap) manifest stronger robustness to the temperature-dependent mixing effect. However, it is worth stressing that, even if this mixing effect reaches its maximum in the outer shell, it is not restricted only to that region. Indeed, in general it extends to the entire lattice. This can be seen by looking at the lower row of FIG. 4.7 in which a section of the density map of the two species is plotted for $y = L/2$ along the x-direction. From Fig. 4.7 it can be noticed as in the case of shell structure (left panel), when the density of a species reaches its own maximum, the other does not go identically to zero as it does in the completely demixed case (right panel). A partial but finite mixing of the two species is present everywhere in the lattice.

In FIG. 4.8 we show the behaviour of the Δ parameter as function of T/t for the trapped case for $U/t = 10$, $U_{ab}/t = 15$ and a harmonic potential strength $\omega_H/t = 0.03$. Each Δ curve in the plot corresponds to a series of different simulations for different temperatures with the same number of bosons N in the system. Even in the trapped case, the parameter Δ very well quantifies the degree of spatial separation of the two species as well as the mixing effect induced by quantum fluctuations. Slightly higher number of bosons in the system confirms the robustness against temperature mixing effect at higher filling. Furthermore, we notice that the jump of Δ over the considered range of temperatures in the trapped case is smaller than in the homogeneous one (about one order of magnitude). Larger local densities at the center of the trap imply larger interactions energies thus reducing the boson mobility and their mixing degree.

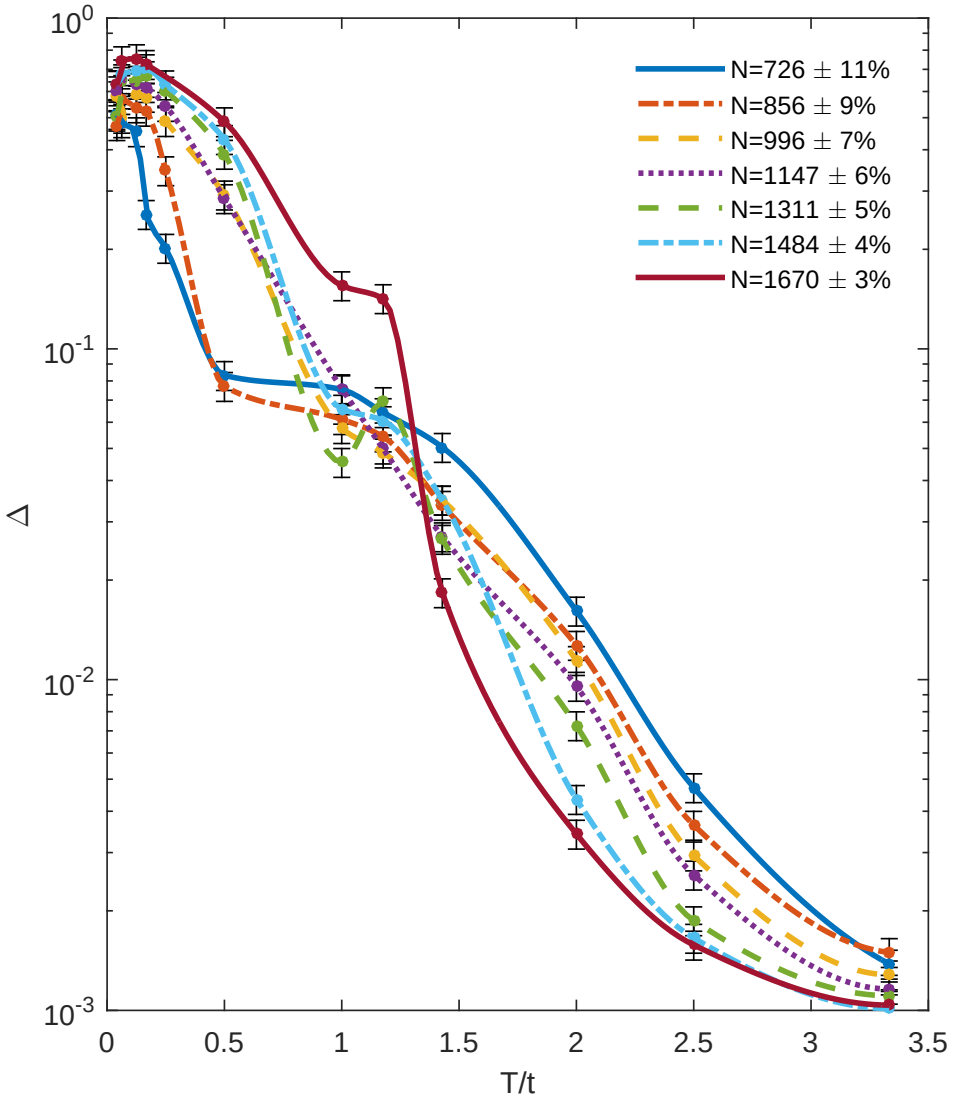

Fig. 4.8 Δ parameter as a function of T/t in the trapped case ($U/t = 10$, $U_{ab}/t = 15$ and $\omega_H/t = 0.03$) for different total boson number N (lines are guidelines).

4.2.1 TOF images at finite temperature

In search of additional experimental signatures of the temperature-driven transition from the dSF to the 2SF phase, we computed the momentum distributions $n_{c,\mathbf{k}} = |\phi_{(\mathbf{k})}|^2 \sum_{i,j} e^{i\mathbf{k}(\mathbf{r}_i - \mathbf{r}_j)} \langle c_i^\dagger c_j \rangle$ [78] for species $c = a, b$.

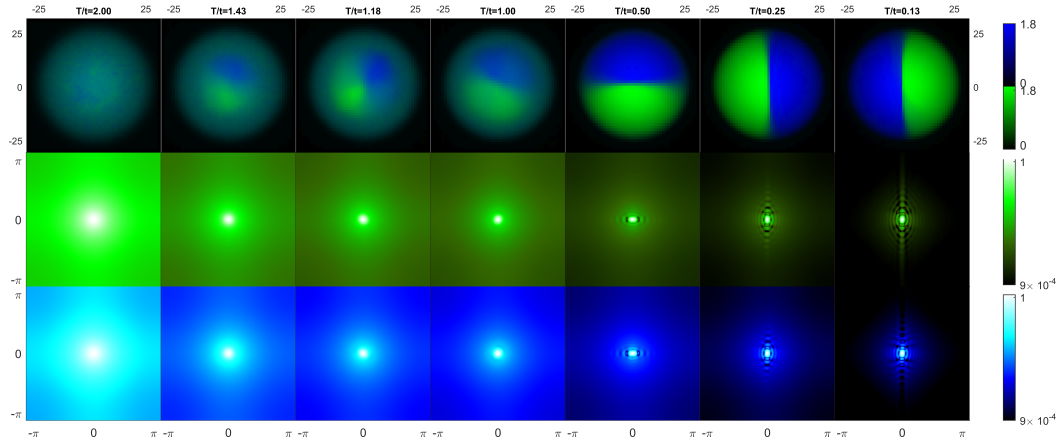

Fig. 4.9 Density maps (first row) and computed TOF images for specie A (second-row) and B (third-row) for decreasing temperature (left to right). The mixture ($U/t = 10$, $U_{ab}/t = 15$) is trapped in a harmonic potential of strength $\omega_H/t = 0.03$.

In second and third row of FIG. 4.9 we plotted the momentum distribution of species A (second row) and B (third row) for a trapped mixture at decreasing temperatures (left to right). By increasing the temperature in the system, we observe how the abrupt changes in the momentum distribution marks the appearance of the spatial shell structure and the mixed phase.

This dramatic change is outlined in FIG. 4.10 where we plot together density and momentum distribution of both species for a spatial shell structure configuration at $T/t = 1.00$ (left column) and a completely demixed one at $T/t = 0.06$ (right column). Both FIG. 4.9 and FIG. 4.10 are obtained by simulating the system with $N \approx 1670 \pm 3\%$ bosons, and for interactions $U/t = 10$, $U_{ab}/t = 15$ and $\omega_H/t = 0.03$. We observe the disappearance of the interference pattern of the single-species momentum distribution as soon as the phase coherence is restored over the entire lattice by the presence of mixed superfluid species. As shown in FIG. 4.7, the presence of a spatial shell structure implies a residual mixing of the two bosons species over the entire lattice. The fact that the two species are superfluid on the entire lattice, forces phase coherence among all the lattice sites producing no interference pattern when the optical lattice is turned off. On the other hand, when the "hard-wall" characterizing the spatial separation of the demixed phase is present, the phase coherence is restricted to the portions of the lattice where a single species is confined. This produces the interference pattern shown in the TOF images of FIGs. 4.9 and 4.10. Such patterns are essentially due to the interference of propagating

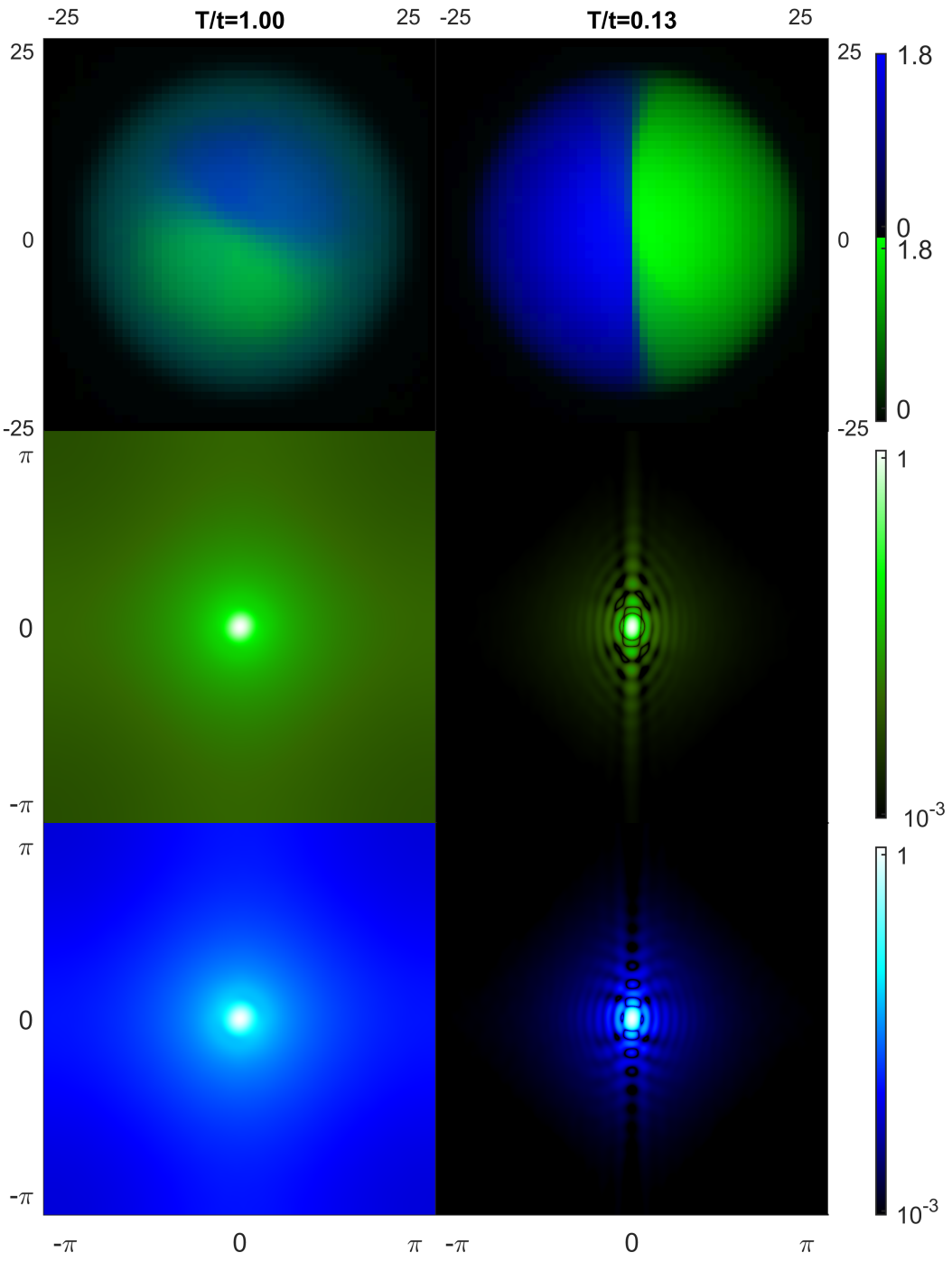

Fig. 4.10 Density maps (first row) and computed TOF images for specie A (second-row) and B (third-row) for temperatures $T/t = 1.00$ (left column) and $T/t = 0.06$ (right column). The mixture ($U/t = 10$, $U_{ab}/t = 15$) is trapped in a harmonic potential of strength $\omega/t = 0.03$.

and reflecting waves bouncing back from the “hard-wall” separating the demixed species.

TOF images of meta-stable states

By using TOF images it is possible to understand if the demixed system is in the ground state configuration or in a meta-stable state close to it. The minimum-energy configuration in a harmonically trapped system, is characterized by a straight boundary between the two species [72] (e.g. see right panel of FIG. 4.10). However, in Bose-Hubbard systems [83, 84] there exists infinitely-many local minima featuring meta-stable states whose energy is really close to the ground-state. These states are characterized by configuration of the mean occupation numbers slightly different from the minimum energy configuration. These configuration features in general irregular or multiple boundaries between the two species. By computing the TOF images of such non-equilibrium configurations, we find that the irregular/multiple boundaries of the demixed configuration leads to irregular and more complex interference patterns. Two example of these configurations are reported in FIG. 4.11. In the two panels we display the TOF images of both species A (central column) and B (right column) of two different systems with $N \approx 1453$ (Upper panel) and $N \approx 1644$ (Lower Panel), respectively. Both simulations are performed at $T/t = 0.042$, $U/t = 10$, $U_{ab}/t = 15$ and $\omega_H/t = 0.03$.

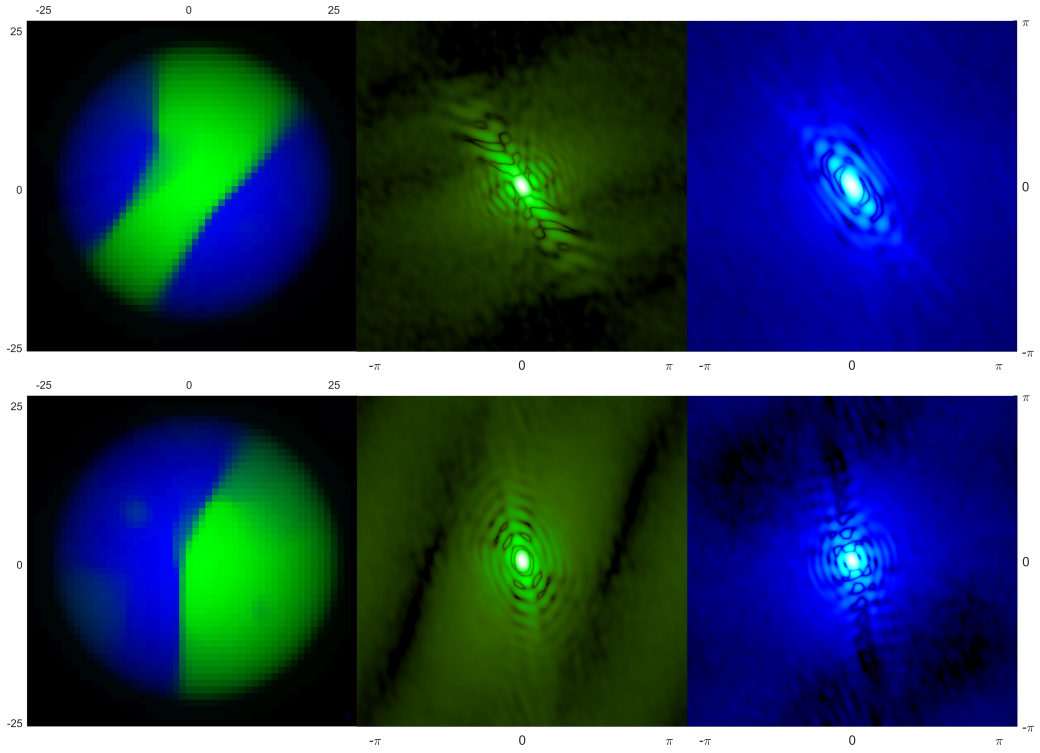

Fig. 4.11 Metastable configurations and related momentum distributoins of species A (central column) and B (right column). Simulation performed with $N \approx 1453$ (Upper panel) and $N \approx 1644$ (Lower Panel) at $T/t = 0.042$, $U/t = 10$, $U_{ab}/t = 15$ and $\omega_H/t = 0.03$

4.2.2 Normal fluid Phase Transition

For sufficiently high temperatures, the outer (spatial) shell is filled with a normal fluid (NF). In order to check the presence of the NF phase we computed the field-field correlators:

$$\langle \Psi_c(r)^\dagger \Psi_c(d) \rangle = \sum_{i:|\mathbf{r}_i|=r} \sum_{j:|\mathbf{r}_i-\mathbf{r}_j|=d} \langle c_i^\dagger c_j \rangle \tag{4.3}$$

for species $c = a, b$. These are obtained from correlators $\langle c_i^\dagger c_j \rangle$ by grouping together all the sites i at a given radius r (from the center of the trap) and all the sites j at a given distance $d = |\mathbf{r}_i - \mathbf{r}_j|$ from the sites i. In the right column of FIG. 4.12 we show the behaviour of correlators (4.3) of species A for increasing temperatures. Due to symmetry, the correlators of species B manifest the same behaviour and therefore are omitted. For the sake of completeness, the left column of FIG. 4.12 displays the corresponding density maps. FIG. 4.12 shows that for low temperatures the field-field correlation is spread uniformly all over the occupied lattice sites. On

the other hand, we notice that for sufficiently high temperatures the system manifests long-range correlation in a disk-like region around the trap center, and short-range correlation for larger radial distances. In particular, long-range correlations suggest the presence of superfluid phases (dSF and 2SF) in the central disk-like region, while short-range correlations suggest the presence of an external NF shell in the outer portion of the lattice. We notice as well that spatial-shell structures features an increasing thickness of the NF shell for increasing temperatures (last two rows of FIG. 4.12).

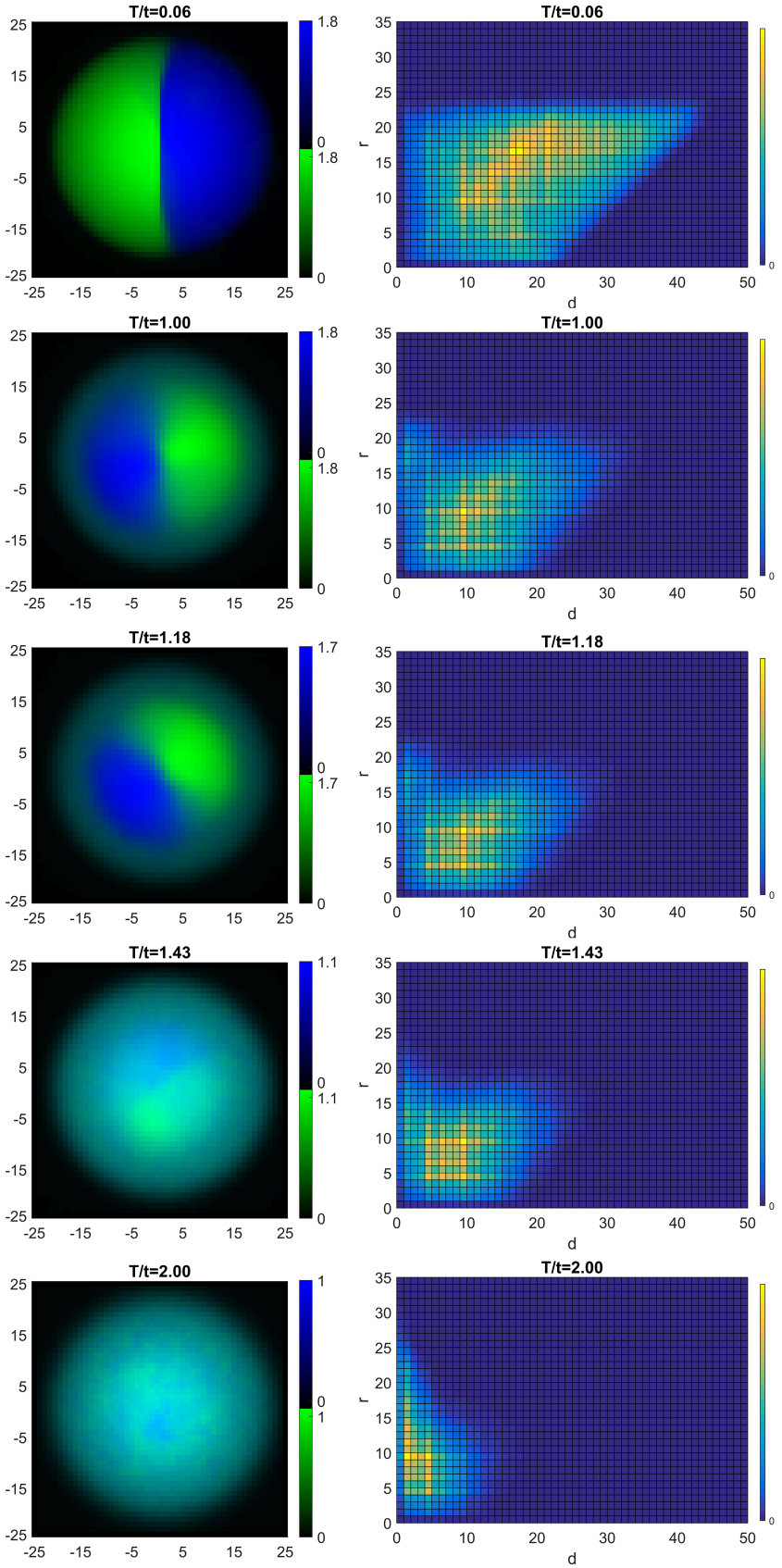

Fig. 4.12 Field-Field correlator $\langle \Psi_c(r)^\dagger \Psi_c(d) \rangle$ (in arbitrary units) of a single bosonic species ($c = a$) for increasing temperatures (right column), and their associated density maps (left column).

4.3 Strong interaction regimes

As did in chapter 3 at zero-temperature, we now move on considering the trapped system within the strong interaction regime. We run several simulations at finite temperature. The simulations are performed in the temperature range $T/t = 0.042 \div 3.33$ and for each case the density maps and the demixing parameter Δ are analyzed and estimated. We find that much richer spatial shell structures arise in the strong interaction regime, and that even in this case phase separation is progressively destroyed by temperature fluctuations.

In figure 4.13 we plot the parameter Δ as a function of temperature T/t for stronger values of U/t and U_{ab}/t ($U/t = 20$, $U_{ab}/t = 24$ and $\omega_H/t = 0.12$). We notice that even in the strong interaction regime Δ manifests a decreasing behaviour as a function of temperature. By comparing FIG.4.8 and FIG. 4.13 we notice that Δ undergoes a way smaller jump through the same range of temperature in the high interaction case.

In figure 4.14 we show that spatial shell structures arise also for larger values of interaction U/t and U_{ab}/t. However in these regimes, as shown in FIG. 3.1, the phase diagram exploits different quantum phases depending on the filling. In particular, for our selected value of $U/t = 20$ and $U_{ab}/t = 24$, at zero-temperature, and integer local filling, the system is expected to be in dMI state. The presence of such a phase can be noticed from the appearance of constant and integer density plateau in the total density profiles shown in FIG. 4.14 (second row plots, black-solid lines). The incompressibility of dMI phase lead to regions of constant integer filling. If the thickness of these plateau is small enough, the incompressibility of the Mott-Insulator is capable to counteract the action of the external harmonic trap that would impose a much smoother density profile. Such a phase can be observed in the regions of integer filling (density maps at $T/t = 0.25$ and $T/t = 0.06$ in FIG. 4.14). As discussed in chapter 3 the strong interaction and very low temperatures are responsible for the fragmented structure of these density maps, and they are intimately related with the metastable character of these configurations.

Furthermore, at higher temperatures (left columns in FIG. 4.14) in the outer regions, we find a mixed phase forming a thin shell with a $n = 1$ plateau, suggesting the presence of a SCF phase in that region. The SCF is by definition a mixed phase, but with that global Mott-Insulator character that could provide the incompressibility

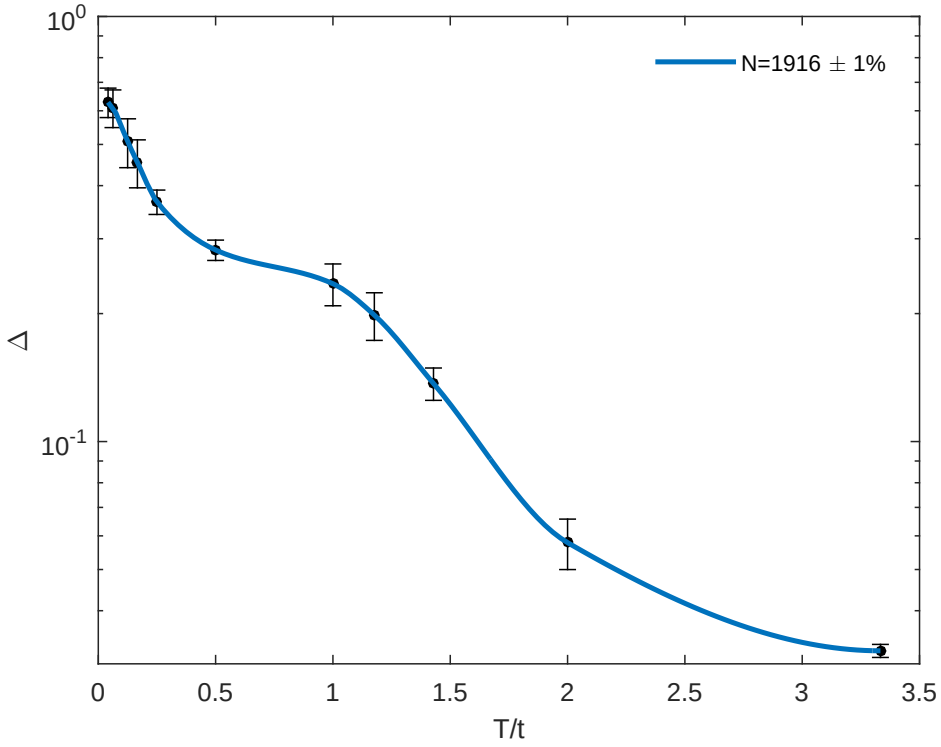

Fig. 4.13 Δ parameter as a function of T/t for a trapped system in the strong interaction regime ($U/t = 20$, $U_{ab}/t = 24$ and $\omega_H/t = 0.12$). Simulations are performed with $N \approx 1916$ particles.

responsible for the formation of constant density plateau. The problem is that, according to the phase diagram of FIG. 3.1, at $T/t \approx 0$, the SCF shouldn't be stabilized for value of U_{ab}/t above the diagonal $U_{ab} = U$. However, the SCF at $U_{ab} > U$ can be made accessible by temperature excitations, since the energy separation between the dMI and the SCF is of the order of $\sim |t^2/U - t^2/U_{ab} + U - U_{ab}|$ [1, 2].

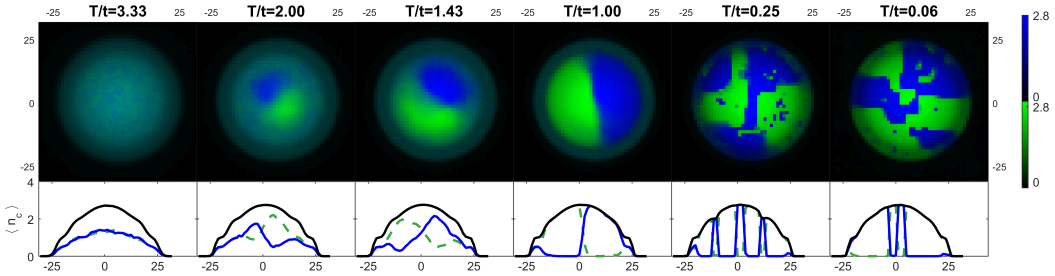

Fig. 4.14 Density maps (first row) and density profiles (second row) of species A (green) and B (blue), for decreasing temperature (left to right) in the SI regime: $U/t = 20$, $U_{ab}/t = 24$ and trapping potential strength $\omega_H/t = 0.12$. Density profiles $\langle n_c \rangle$ are computed along the horizontal axis through the center of the trap. The total density profile is also shown (black-solid line).

Chapter 5

Thermometry of ultra-cold mixtures

In this short chapter we illustrate a method for thermometry of a binary bosonic mixture trapped in an optical lattice. Our proposal, based on the fundamental principle of miscibility, works both in the weakly- and the strongly-interacting regime. This method has been proposed to the scientific community and has been published in the paper: "*Thermometry of Cold Atoms in Optical Lattices via Demixing*" [56].

Thermometry in optical lattices can be very cumbersome, a fact often limiting the comparison between theoretical and experimental findings is the lack of reliable estimators capable of extracting information on the temperature of this kind of systems. In general, measuring fundamental parameters, such as temperature, in strongly correlated quantum gases can be far from trivial. The physical reason is that the primary thermometric quantity used in cold atoms experiments, namely the momentum distribution, in strongly correlated regimes is often dominated by quantum rather than thermal fluctuations, thereby becoming quite insensitive to temperature variations. Furthermore, if compared with continuous counterparts where the typical condensation-temperatures range around the order of magnitude of about $10^2\ nK$, optical-lattice systems, due to their stronger-confinement, are expected to feature temperatures two order of magnitude lower (on the order of the tunneling amplitude $10^0 \div 10^1\ nK$). The extremely low expected temperatures, the difficulty to obtain reliable thermometric estimators together with fact that this is the regime where "quantum magnetism" is expected, make this issue extremely attractive and fascinating.

In the last few years, this challenge stimulated numerous theoretical proposals and experiments [42]. Within the well-understood weakly interacting regime, two main standard approaches have been carried out capable of measuring the temperature in optical lattice system. This is done in general through sample subsets [43, 44, 85, 47], or by measuring in-situ local density fluctuations with high-resolution imaging [34–39]. On the other hand, within the context of bosonic mixtures several seminal work have been reported. With a rubidium condensate, demixing between two spin components was induced by a magnetic field gradient and the width of the interface region was used to estimate the temperature [43]. Recently, the spin waves, or 'magnons', in a spinor Rb condensate were used to reduce the entropy per particle to values as low as $0.02\,k_B$ [48], an order of magnitude below the values required for the onset of magnetic phases [86]. However, the measure of the temperature in the so-called strong interaction (SI) regime still lack of reliable estimators.

In this chapter, we want to propose a thermometry technique for ultra-cold quantum mixtures in optical lattices based on the demixing of two mutually repulsive components. In the previous chapter (chapter 4) we have shown that temperature fluctuations compete with, and eventually destroy, demixing. The idea is to take advantage of this competition to propose a route for thermometry by employing the same global demixing estimator Δ defined in chapter 3 which can readily be measured and used to determine the temperature.

5.1 Δ-thermometer

Let's now move on designing our new thermometric technique. For doing so we first need to briefly review the thermometric property of parameter Δ. In chapter 4 we have shown that Δ parameter, in both trapped and homogeneous conditions, exhibits a decreasing behaviour as a function of the temperature T/t. For the sake of clearness, in the two panel of FIG. 5.1, we report the behaviour of parameter Δ as a function of temperature T/t and inter-species interaction U_{ab}/t, in the homogeneous case, for $n = 1$ (left panel) and $n = 2$ (right panel). The strong dependence of Δ on T displayed in the dSF phase describes very well the competition between the phase separation and the temperature fluctuations and motivates the basic idea of extracting the temperature from the measurement of the demixing parameter.

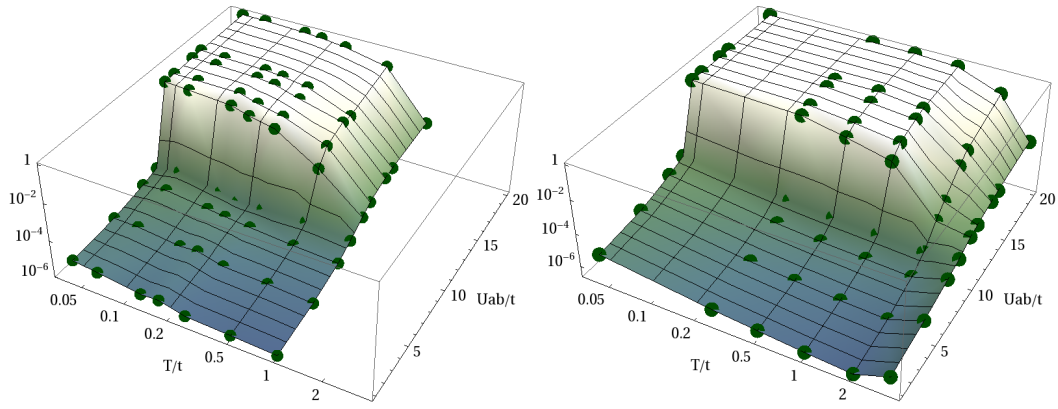

Fig. 5.1 Parameter Δ as a function of temperature T/t and interspecies interactions U_{ab}/t, at $U/t = 10$. Total filling $n = 1$ (left panel) and $n = 2$ (right panel). Points show numerical results.

Furthermore, in chapter 4, we outlined that at $n = 2$, much higher temperature are required in order to destroy demixing, showing that robustness against miscibility results in a stronger robustness against temperature fluctuations. In this sense, larger filling factors shift the operating range of the proposed thermometer towards higher temperatures. This provides an interesting scenario as in a real experimental setup, a harmonic trap is always present leading to non-uniform local filling profiles with central fillings in general higher than one.

In order to properly design a thermometric technique for real experimental applications, is therefore necessary to move to consider the harmonically trapped case. As seen in chapter 4, also in this topological scenario, the Δ has been proven to remarkably being able to return a reliable estimate of the temperature. Furthermore, Δ seems to work well not only in the weakly- but also within the strongly-interacting regime. We can therefore use QMC simulations to physically implement our Δ-thermometer.

By simply running simulations at different finite temperatures, within the correct settings of the inter-species and intra-species interaction U_ab/t and U/t, and loading an established number of particles in the system, it is possible to estimate for each simulation, the value of the parameter Δ and link it to the value of the temperature under which the simulation has been performed. If one is now able to measure experimentally the parameter Δ (see subsection 5.2 below), by knowing the number of particle in the system, and the parameter under which the experiment has been performed (the value of t, U, and U_{ab}), he would be able to link the measure of Δ

to the value of the temperature in the optical-lattice system. In FIG. 5.2 we plot

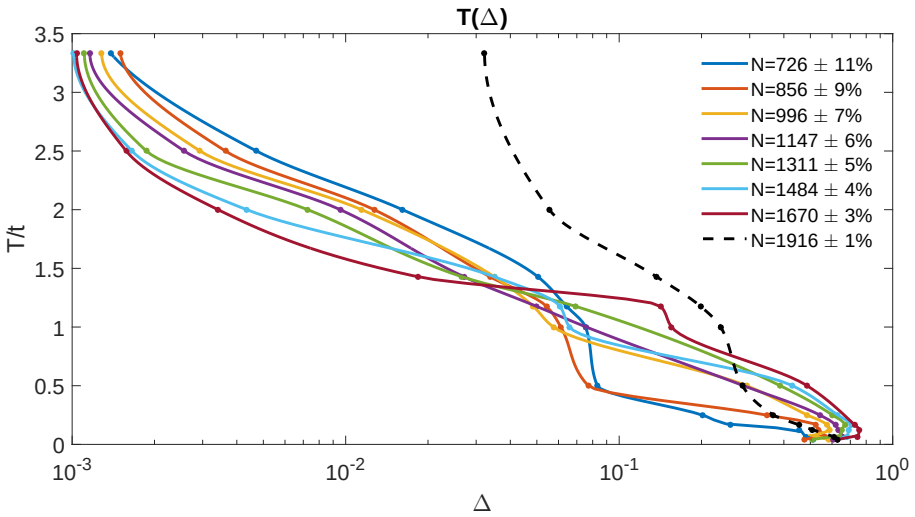

Fig. 5.2 Δ-thermometer: Temperature as a function of the parameter Δ in the trapped case. Solid lines: $\omega_H/t = 0.03, U/t = 10, U_{ab}/t = 15$; black dashed line: $\omega_H/t = 0.12, U/t = 20, U_{ab}/t = 24$.

the T VS Δ curves for both weak- and strong-interacting regime, obtained by the simulations shown in chapter 4 (see FIG. 4.8 and 4.13 for details). By exploiting the curves of FIG. 5.2 it is possible to link directly an experimental measurement in Δ with the corresponding measure of the temperature of the system $T(\Delta)$. This constitutes by itself the essence of our thermometric technique.

The range of measurable temperatures detectable with this technique can be expressed in Kelvin by knowing the value of the common hopping amplitude t of the twin-species. As shown in section 1.4.1, typical experimental tunneling amplitude for Rubidium and Potassium are: $t_{Rb}/k_B = 2.08\ nK$ and $t_K/k_B = 17.9\ nK$. In table 5.1 we report the temperature-range of the Δ-thermometer shown in FIG. 5.2 measured in Kelvin by considering the tunneling amplitude listed above.

T/t	T_{Rb} $[nK]$	T_K $[nK]$
0.042	0.08	0.75
0.5	1.04	8.95
1	2.08	17.90
1.5	3.12	26.85
2	4.16	35.80
2.5	5.20	44.75
3	6.24	53.70

Finally, our currently proposed thermometry technique can be validated by parallely measuring the temperature through an ordinary accepted technique [87]. This can be done by first considering the case of a moderately shallow optical lattice where, due to the sufficiently weak interspecies interaction, each species is superfluid and the temperature can independently be determined by their momentum distribution. Once the tare has been taken over, we can move forward to consider a deeper optical lattice, thus SI regimes, for which we lack of reliable temperature estimators other than the direct microscopic observation of particle-hole pairs. As we just showed above, within this regime, our proposed thermometry technique seems to prove a remarkably effective tool.

5.2 Experimental measure of Δ

The demixing parameter Δ defined in chapter 3 relies on single-site occupation numbers $\langle n_{ci}\rangle$:

$$\Delta = \frac{1}{M}\sum_i \left[\frac{\langle n_{ai}\rangle - \langle n_{bi}\rangle}{\langle n_{ai}\rangle + \langle n_{bi}\rangle}\right]^2. \tag{5.1}$$

For this reason, an experimental measurement of Δ can be obtained directly from high resolution microscope images [34–39]. However, being a global observable, Δ does not require knowledge of the local densities and is also obtained by spectroscopic techniques. Indeed, the number of sites occupied by both species can be detected by driving transitions sufficiently narrow in energy, involving either the internal atomic states, such as microwave transitions [88], or the external degrees of freedom, such as in band spectroscopy [89]. In practice, the task is eased in proximity of the interspecies Feshbach resonance enhancing U_{ab}. We focus on hyperfine transitions for sake of concreteness: if the interactions between final states are negligible with

respect to U_{ab}, a microwave field with a frequency shift $\sim U_{ab}\ell m$ with respect to the bare hyperfine splitting will drive transitions in all lattice sites with occupation numbers $(n_a, n_b) = (\ell, m)$ or (m, ℓ). A measurement of the transferred atoms yields the relative number of the lattice sites, $f(\ell, m)$, with the given fillings. Once all the $f(\ell, m)$ values are deduced from the microwave spectrum of transferred atoms, the demixing parameter is readily obtained as

$$\Delta_{exp} = \sum_{(\ell,m)} f(\ell, m)(\ell - m)^2/(\ell + m)^2. \tag{5.2}$$

Chapter 6

Analytic solution of the 2-sites BH model with the Bogoliubov approach

In this chapter we focus on the investigation of a simple two-sites BH model from the analytical and numerical point of view. This model describes the simplest but not trivial system where mixtures of different atomic species can be loaded in the trap formed by a double-well potential. Two-well systems has been experimentally realized by Albiez and co-workers in 2005 [90] by superposing a parabolic trap with a sinusoidal linear potential. From the theoretical point of view, this system has been widely explored within the mean-field approach to analyze the atomic counterpart of the Josephson effect in superconductor-oxide-superconductor junctions [91], the dynamical stability of binary mixtures [92, 93], different types of self-trapping solutions [94], the effectiveness of the space-mode description within the Gross-Pitaevskii picture [95, 96] and the Rabi-Josephson regime [97].

In the following we explore the low-energy properties of a two-species mixture confined in a double-well potential. The model describing this system is therefore a two-species Bose-Hubbard Hamiltonian defined on a two-site lattice. We first numerically diagonalize the Hamiltonian in the zero-temperature regime. We then use the numerical results to approach analytically the investigation of the low-energy regimes within the Bogoliubov approximation. The diagonalization is performed in both the strong-interaction ($|U_{ab}| > U$) and in the weak-interaction ($|U_{ab}| < U$) regime, by identifying weakly-occupied modes in the space-mode picture and in the momentum-mode picture, respectively. We considered here both the attractive and

repulsive inter-species interaction cases. We reconstruct the low-energy spectrum, comparing the latter with the numerical eigenspectrum, and provide an approximate form of weakly-excited states.

Despite the simplicity of the system, we find that the most fundamental properties of the mixing/demixing phase transitions shown in the previous chapters also arise in this simple model. By keeping fixed the intra-species interaction U, variations of inter-species interaction U_{ab} produce significant changes in the structure of the ground state. On the repulsive side ($U_{ab} > 0$), increasing U_{ab} drives the ground state from the uniform state (delocalization regime with mixed species) to a symmetric superposition of states exhibiting a macroscopic space separation (demixing) of the two species, passing through an intermediate configuration where the delocalized state and the symmetric demixed state coexist. On the other hand, in the attractive case ($U_{ab} < 0$), the uniform ground state features configurations in which bosons of different species tend to macroscopically populate the same site (localization regime with mixed species). Within this analysis, by reconstructing the low-energy spectrum we find that the mixing/demixing transition features a spectral collapse reflecting the dramatic change of the dynamical algebra of the model Hamiltonian.

The chapter is organized as follows. We first briefly review the two-sites BH model, we then move to the discussion of the numerical results and to introduce the analytical diagonalization method used.

The results and the discussions contained in this chapter have mainly been published in the paper [57].

6.1 The 2-site 2-species BH Hamiltonian

Recalling what we showed in chapter 1, the two-species Bose-Hubbard Hamiltonian for a two-site system is defined as:

$$\hat{H} = \sum_{c=a,b} \hat{H}_c + \hat{H}_{ab} \tag{6.1}$$

with

$$\hat{H}_c = \frac{U_c}{2}[\hat{n}_{c1}(\hat{n}_{c1}-1) + \hat{n}_{c2}(\hat{n}_{c2}-1)] - t_c\left(c_1^\dagger c_2 + c_2^\dagger c_1\right),$$

and

$$\hat{H}_{ab} = U_{ab}\left(a_1^\dagger a_1 b_1^\dagger b_1 + a_2^\dagger a_2 b_2^\dagger b_2\right) .$$

Where $\hat{n}_{c1} = c_i^\dagger c_i$ is the number operator of bosonic species $C = A, B$ in the site $i = 1,2$. The operator $c_i = a_i(b_i)$ annihilates a boson of species A (B) in the ith site ($i = 1,2$, with 1 (2) representing the left (right) well), U_c is the amplitude of the intra-species onsite interaction, t_c is the tunneling amplitude, and U_{ab} is the interspecies interaction amplitude between bosons in the same well. Boson operators a_i, $a_i^\dagger$, b_i and $b_i^\dagger$, in addition to $[a_i, a_j^\dagger] = \delta_{ij} = [b_i, b_j^\dagger]$ with $j = 1,2$, satisfy the commutators $[a_i, b_j] = 0$, and $[a_i, b_j^\dagger] = 0$. For each species, the total boson numbers $\hat{N}_c$ commute with $\hat{H}$ implying that $N_a = N_{a1} + N_{a2}$ and $N_b = N_{b1} + N_{b2}$ are conserved quantities. Also in this case, we work within the twin-species approximation, assuming species A and B with the same mass, the same intra-species s-wave scattering length, and experiencing identical double-well and harmonic confinements. In the following, we thus set $t_a = t_b \equiv t$ and $U_a = U_b \equiv U$, that is, the components A and B have the same hopping parameter and intra-species interaction.

6.2 Numerical analysis

We numerically solve the eigenvalue equation associated to Hamiltonian (6.1)

$$\hat{H}\,|\psi\rangle_n = E_n\,|\psi\rangle_n \tag{6.2}$$

for fixed numbers N_a and N_b of bosons of species A and B, respectively. In this case the Hamiltonian can be represented by a $M \times M$ matrix with $M = (N_a+1)(N_b+1)$ in the basis $|i,j\rangle_L \otimes |N_a - i, N_b - j\rangle_R$ with $i \in [0, N_a]$ and $j \in [0, N_b]$. For each eigenvalue E_n, with $n = 1,2,...,M$, the corresponding eigenstate $|\psi\rangle_n$ has the form

$$|\psi\rangle_n = \sum_{i=0}^{N_a}\sum_{j=0}^{N_b} C_n(i,j)|i,j\rangle_1 |N_a - i, N_b - j\rangle_2 , \tag{6.3}$$

In the ket $|i,j\rangle_L$, i (j) is the number of bosons of species a (b) in the left well, while in $|N_a - i, N_b - j\rangle_R$, $N_a - i$ ($N_b - j$) is the number of bosons of species A (B) in the right well. Since we focus our attention on the ground state ($n = 1$), we simplify the notation by setting $C_1(i,j) \equiv C(i,j)$.

When both the intra- and the inter-species interactions are zero, the ground state of Hamiltonian (6.1) is given by the product of two atomic (or SU(2)) coherent states (see, e. g., [98], [99]).

$$|\phi_{0_{CS}}\rangle = \frac{1}{\sqrt{N_a!N_b!}}\left(\frac{a_1^\dagger + a_2^\dagger}{\sqrt{2}}\right)^{N_a}\left(\frac{b_1^\dagger + b_2^\dagger}{\sqrt{2}}\right)^{N_b}|0,0\rangle_1|0,0\rangle_2\,, \tag{6.4}$$

where $|0,0\rangle_1|0,0\rangle_2$ is the state with no bosons. Coherent states of this form usually describe the superfluid phase for large t_c/U_c where bosons are uniformly distributed on the lattice and thus totally delocalized.

If one assumes that the intra-species interactions U_a, U_b are essentially negligible with respect to the (absolute value of the) inter-species interaction $|U_{ab}|$, the ground state of the Hamiltonian is essentially formed by a symmetric superposition of two states with macroscopically populated wells. Its form depends on the sign of U_{ab}. In particular, for $U_{ab} > 0$ (repulsive inter-species interaction), the ground state has the form

$$|\phi_{0_M}\rangle \simeq \frac{1}{\sqrt{2}}\Big(|N_a,0\rangle_1|0,N_b\rangle_2 + |0,N_b\rangle_1|N_a,0\rangle_2\Big)\,, \tag{6.5}$$

whereas for $U_{ab} < 0$ (attractive inter-species interaction) the ground state is

$$|\phi_{0_M}\rangle' \simeq \frac{1}{\sqrt{2}}\Big(|N_a,N_b\rangle_1|0,0\rangle_2 + |0,0\rangle_1|N_a,N_b\rangle_2\Big)\,. \tag{6.6}$$

In FIGs. 6.1, 6.2 and 6.3, we show the ground state of Hamiltonian (6.1) for different values of U_{ab}. The left panel of FIG. 6.1 represents the ground state when boson-boson interactions are zero, namely, $U = U_{ab} = 0$. This situation corresponds to the atomic coherent state (6.4). As shown in the right panel of the same figure for which $U_{ab} = 0$ and $U = 0.1t$, the distribution $|C(i,j)|^2$ becomes narrower as soon as the on-site repulsive interaction is switched on. By keeping fixed $U = 0.1t$, a finite and repulsive interaction U_{ab} balances this effect and causes the broadening of distribution $|C(i,j)|^2$ which becomes more and more pronounced when U_{ab} is increased, as the left panel of the first row in FIG. 6.2 shows. By further increasing the interspecies repulsion, the ground-state structure exhibits a transition to a configuration characterized by the coexistence of a delocalized state (well represented by state (6.4)) and the two localized states $|N_a,0\rangle_L|0,N_b\rangle_R$ and

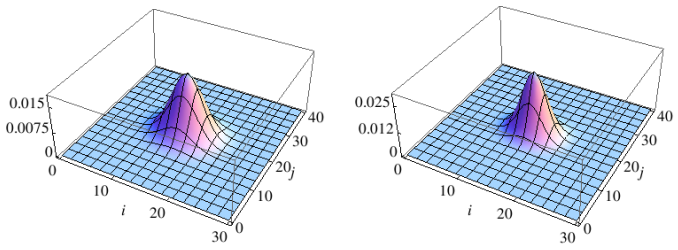

Fig. 6.1 Ground-state coefficients $|C(i,j)|^2$ vs i (left occupation numbers of species A) and j (left occupation number of species B) for $U_{ab} = 0$, $U = 0$ (left panel), $U = 0.1$ (right panel) and boson numbers $N_a = 30$, $N_b = 40$. Energies in units of t.

$|0,N_b\rangle_L|N_a,0\rangle_R$. Such an effect (already observed for bosons in a three-well potential with ring geometry [100]) is well visible in the first row (right plot) of FIG. 6.2.

This coexistence (where the ground state losses its coherence) is destroyed by a sufficiently-strong interspecies repulsion. In this case, the ground state becomes the symmetric superposition of (macroscopic) localized states described by state (6.5) and well illustrated in the second row (right plot) of FIG. 6.2. In correspondence to the same value of the on-site interaction U but with attractive interspecies interaction ($U_{ab} < 0$, see FIG. 6.3), distribution of $|C(i,j)|^2$ displays the same changes characterizing the repulsive case when U_{ab} is increased. FIG. 6.3 clearly shows that sufficiently strong inter-species attractions give rise to a superposition having the form of state (6.6) describing localized mixed species.

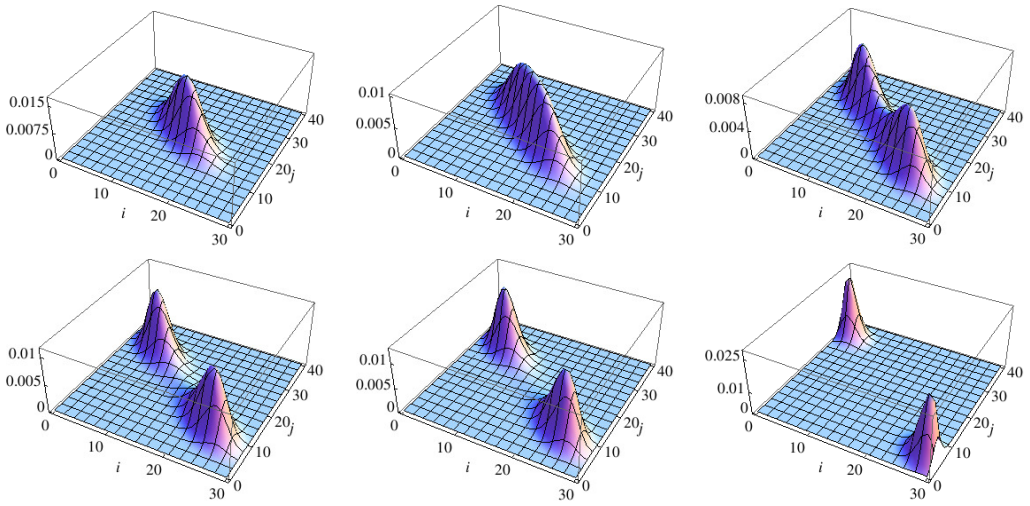

Fig. 6.2 Ground-state coefficients $|C(i,j)|^2$ vs i (left occupation numbers of species A) and j (left occupation number of species B) for $U = 0.1$. First row: $U_{ab} = 0.15$, $U_{ab} = 0.16$, $U_{ab} = 0.165$. Second row: $U_{ab} = 0.168$, $U_{ab} = 0.17$, $U_{ab} = 0.2$. Number of bosons: $N_a = 30$, $N_b = 40$. Energies in units of t.

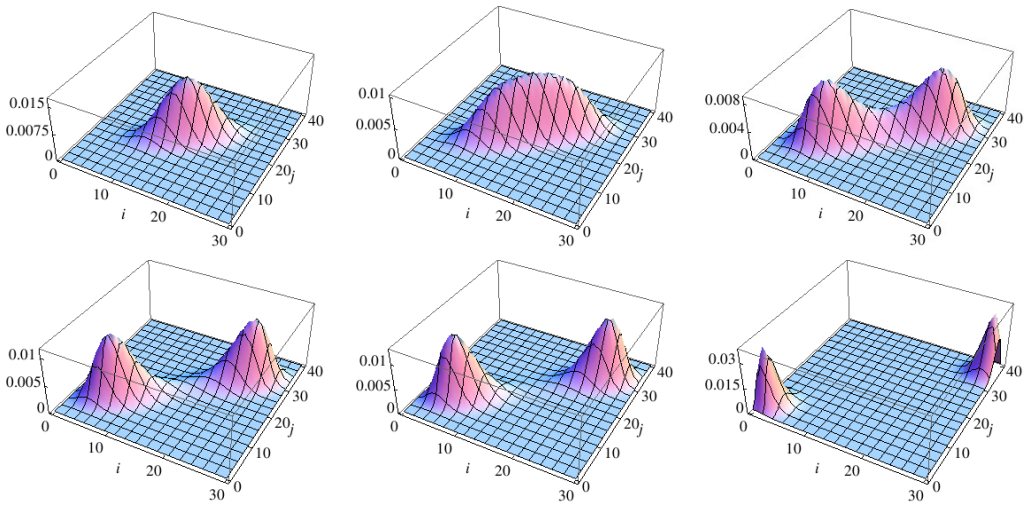

Fig. 6.3 Ground-state coefficients $|C(i,j)|^2$ vs i (left occupation number of species A) and j (left occupation number of species B) for $U = 0.1$. Top-bottom. First row: $U_{ab} = -0.15$, $U_{ab} = -0.16$, $U_{ab} = -0.165$. Second row: $U_{ab} = -0.168$, $U_{ab} = -0.17$, $U_{ab} = -0.21$. Boson numbers: $N_a = 30$, $N_b = 40$. Energies in units of t.

6.3 Diagonalization through Bogoliubov approach

The analysis of section 6.2 about the different regimes characterizing the ground state provides useful information for studying the spectrum of the model Hamiltonian through the Bogoliubov approach.

In the two strong-interaction regimes ($|U_{ab}| > U_c$) relevant to $U_{ab} > 0$ (repulsive interaction) and $U_{ab} < 0$ (attractive interaction), the macroscopic localization effects illustrated in FIGs. 6.2 and 6.3, respectively, show how for $U_{ab} > 0$ one observes an almost complete spatial separation of the two species strongly localized in different sites, whereas for $U_{ab} < 0$ one has an almost complete merging of the two species localized at the same site. This allows one to identify weakly-occupied modes and thus to implement the Bogoliubov scheme.

A more complicated situation is found in the regimes $|U_{ab}| < U_c$ (again including the cases $U_{ab} < 0$ and $U_{ab} > 0$), where the two bosonic species are completely delocalized and the boson populations essentially exhibit the same size in the two wells. In this second case, the correct approach for diagonalizing the Hamiltonian is found by looking for macroscopically-occupied modes within the momentum-mode picture.

6.3.1 Weak-interaction regime $|U_{ab}| < U_c$

We start by discussing the diagonalization scheme in the repulsive case of the weak-interaction regime ($|U_{ab}| < U_c$) involving delocalized populations and species mixing. Since the two species are almost equally distributed in the two wells a simple way to recognize weakly-occupied modes [101] is to introduce momentum-like operators

$$\hat{A} = \frac{(a_1 + a_2)}{\sqrt{2}}, \tag{6.7}$$

$$\hat{\alpha} = \frac{(a_1 - a_2)}{\sqrt{2}}, \tag{6.8}$$

$$\hat{B} = \frac{(b_1 + b_2)}{\sqrt{2}} \tag{6.9}$$

and

$$\hat{\beta} = \frac{(b_1 - b_2)}{\sqrt{2}}. \tag{6.10}$$

Note that the boson-number conservation is now given by the relations

$$\begin{cases} N_a = N_{a1} + N_{a2} = N_A + N_\alpha \,, \\ \\ N_b = N_{b1} + N_{b2} = N_B + N_\beta \,. \end{cases} \tag{6.11}$$

The Hamiltonian (6.1) in the new mode picture take the form:

$$\hat{H} = \frac{U_{ab}}{2}\sqrt{N_a N_b}\,(\hat{\alpha}+\hat{\alpha}^\dagger)\,(\hat{\beta}+\hat{\beta}^\dagger) + 2t_a\hat{N}_\alpha + 2t_b\hat{N}_\beta \\ + \frac{U_a}{4}N_a(\hat{\alpha}+\hat{\alpha}^\dagger)^2 + \frac{U_b}{4}N_b(\hat{\beta}+\hat{\beta}^\dagger)^2 + K, \tag{6.12}$$

where the terms depending on N_a, N_b are grouped in the constant

$$K = \frac{U_a}{4}(N_a^2 - N_a) + \frac{U_b}{4}(N_b^2 - N_b) + \frac{U_{ab}}{2}N_a N_b - tN \,, \tag{6.13}$$

and third-order (or higher-order) terms have been neglected. We notice that in the current regime ($|U_{ab}| < U_c$), modes $\hat{A}$, $\hat{B}$ are macroscopically occupied, ($N_A \gg N_\alpha$, $N_B \gg N_\beta$) and can be regarded as complex parameters within the Bogoliubov approximation. The application of this scheme provides the diagonal Hamiltonian

$$\hat{H}_D = K - 2t + \sqrt{R_\alpha}\,(2\hat{\alpha}^+\hat{\alpha}+1) + \sqrt{R_\beta}\,(2\hat{\beta}^+\hat{\beta}+1) \,, \tag{6.14}$$

where $K = \sum_{c=a,b} U_c(N_c^2 - N_c)/4 + U_{ab}N_aN_b/2 - tN$, and $t_a = t_b = t$ has been assumed. The symbols R_α and R_β are defined by

$$R_{\alpha,\beta} = t[t + (u \mp D)/4] \,, \quad D = \sqrt{\Delta^2 + 4U_{ab}^2 N_a N_b} \,, \tag{6.15}$$

with signs $-$ $(+)$ corresponding to R_α (R_β), $u = U_aN_a + U_bN_b$, and $\Delta = U_aN_a - U_bN_b$. Note that, we have tacitly assumed $U_bN_b > U_aN_a$. In the opposite case $U_bN_b < U_aN_a$ the definitions of R_α, R_β are simply exchanged.

The eigenvalues read

$$E(N_\alpha, N_\beta) = K - 2t + \sqrt{R_\alpha}(2N_\alpha + 1) + \sqrt{R_\beta}(2N_\beta + 1) \tag{6.16}$$

and the corresponding energy eigenstates

$$|E(N_\alpha, N_\beta)\rangle = |N_A\rangle|N_B\rangle\hat{U}^\dagger\hat{S}_\alpha\hat{S}_\beta|N_\alpha\rangle|N_\beta\rangle \tag{6.17}$$

are obtained by mixing the squeezed Fock states $\hat{S}_\alpha|N_\alpha\rangle$ and $\hat{S}_\beta|N_\beta\rangle$ ($\hat{S}_\alpha$ and $\hat{S}_\beta$ are, in fact, squeezing operators) through the SU(2)-group rotation $\hat{U}$. We remand to our paper [57] for the detailed calculations.

As far as $4t+u > D$, the quantity R_α is positive and the contributions to the spectrum relevant to N_α and N_β are both discrete. A dramatic change in the energy spectrum emerges when $R_\alpha \to 0$. By rewriting the condition $4t+u > D$ in the form $U_aU_b + \Delta_t > U_{ab}^2$, and observing that $\Delta_t = 8t(t+u)/N_aN_b \simeq 0$ for bosonic populations large enough, this effect takes place when

$$U_aU_b - U_{ab}^2 \to 0^+ . \tag{6.18}$$

The latter formula reproduces for $U_a = U_b = U$ (twin species) the well-known mixing condition $U = U_{ab}$ characterizing bosonic mixtures and derived heuristically in subsection 3.2.1 for large-size lattices.

For U_{ab}^2 approaching the product U_aU_b from below, the inter-level separation for the α-mode spectrum tends to vanish thus determining, for $U_{ab}^2 = U_aU_b$, the transition to a continuous spectrum (spectral collapse). Hamiltonian (6.12) (emerging from the Bogoliubov approach and leading to the diagonal form (6.14)) thus predicts a *spectral collapse* of the energy levels for $U_{ab}^2 \to U_aU_b$. This mechanism is discussed in detail in [101] and [102]. The resulting macroscopic effect (also observed in Ref. ([103])) can be interpreted as the hallmark of the transition from the mixed-species regime (illustrated in the first row, left panel of FIG. 6.2) to the demixed regime involving, for $U_{ab} > 0$, the spatial separation of the two species (illustrated in the second row, right panel of FIG. 6.2).

The left panels of FIGs 6.4 and 6.5 corresponding to the repulsive and the attractive case, respectively, describe the eigenvalues of the 2-species Hamiltonian in the weak-interaction regime $|U_{ab}| < U$.

Such figures clearly show the excellent agreement between the eigenvalues provided by equation (6.16) and the eigenvalues determined numerically. By following the same "Bogoliubov vs numerics" path, it is interesting to check if the expected transition to a continuous spectrum (spectral collapse) discussed above, is observed.

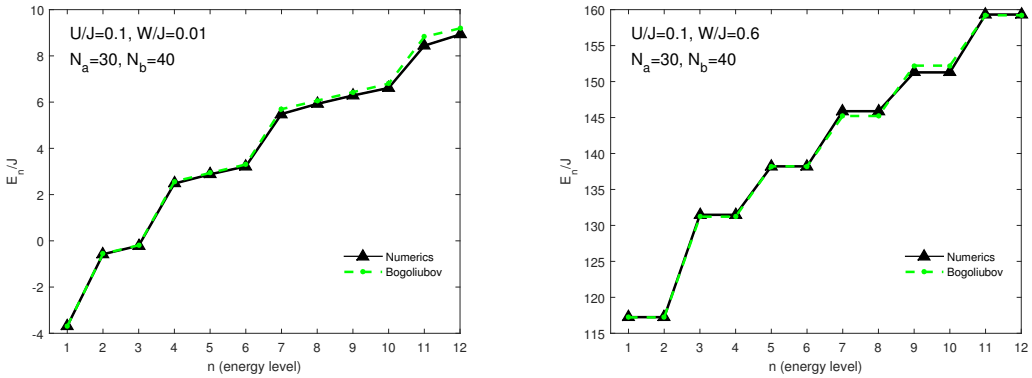

Fig. 6.4 Case $U_{ab} > 0$ with $U_a = U_b \equiv U$. Left panel: $U_{ab} < U$. Black triangles: eigenvalues obtained numerically. Green dots: Eigenvalues obtained by Eq. (6.16), $(N_\alpha, N_\beta) = (0,0),(1,0),(0,1),(1,1),(2,1),...$ correspond to the energy level $n = 1,2,3,4,5,...$ ($n = 1$ denotes the ground state). Right panel: $U_{ab} > U$. Black triangles: eigenvalues obtained numerically. Green dots: Eigenvalues obtained by Eq. (6.23), $(N_{a1}, N_{b2}) = (0,0),(0,1),(1,0),(1,1),(1,2),...$ correspond to the energy level $n = 1,2,3,4,5,....$ All the quantities are dimensionless. Lines are for eye-guide.

To this end we have calculated the exact eigenvalues of model (6.1) for two cases described in Fig. 6.6 by the squares-solid (red) line ($U_{ab} << U$) and circles-dashed (black) line where the interspecies interaction $U_{ab} \simeq U$. The latter case represents the limit $U_a U_b - U_{ab}^2 \to 0^+$ with $U_a = U_b = U$ (see formula (6.18)). The comparison of the two lines clearly shows how the continuous character of the energy spectrum emerges in the limit $U - U_{ab} \to 0^+$.

The change $U_{ab} > 0 \to U_{ab} < 0$ does not affect the essence of the previous scheme so that the same conclusions can be found, in the attractive case, when $|U_{ab}|$ is increased and the demixing effect illustrated in FIG. 6.3 takes place.

The dramatic change of the algebraic structure of $\hat{H}$ reflecting the occurrence of the spectral collapse suggests that a different mode picture must be used when $|U_{ab}| > U$ in order to get the Hamiltonian into the diagonal form. This is discussed in the next subsection.

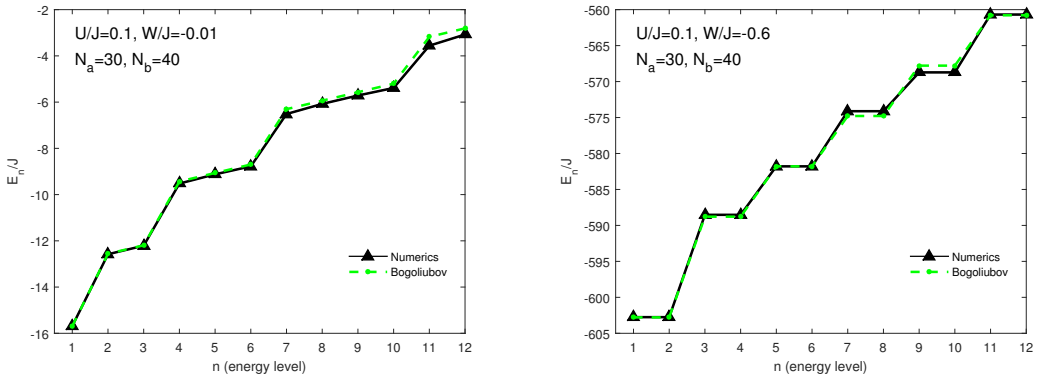

Fig. 6.5 Case $U_{ab} < 0$ with $U_a = U_b \equiv U$. Left panel: $|U_{ab}| < U$. Black triangles: eigenvalues obtained numerically. Green dots: Eigenvalues obtained by Eq. (6.16), $(N_\alpha, N_\beta) = (0,0),(1,0),(0,1),(1,1),(2,1),...$ correspond to the energy level $n = 1,2,3,4,5,...$ ($n = 1$ denotes the ground state). Right panel: $|U_{ab}| > U$. Black triangles: eigenvalues obtained numerically. Green dots: Eigenvalues obtained by Eq. (6.33), $(N_{a1}, N_{b2}) = (0,0),(0,1),(1,0),(1,1),(1,2),...$ correspond to the energy level $n = 1,2,3,4,5,....$ All the quantities are dimensionless. Lines are for eye-guide.

6.3.2 Strong-interaction regime $|U_{ab}| > U_c$

As far as the strong-interaction regime ($|U_{ab}| > U_c$) is concerned we begin by considering the repulsive case ($U_{ab} > 0$). For U_{ab} sufficiently larger than U_c the two bosonic species are spatially separated. Their boson distributions feature therefore two possible forms

$$\begin{cases} N_{a2} << N_{a1} \simeq N_a\,, \quad N_{b1} << N_{b2} \simeq N_b\,, \\ \\ N_{b2} << N_{b1} \simeq N_b\,, \quad N_{a1} << N_{a2} \simeq N_a\,, \end{cases} \tag{6.19}$$

where two bosonic modes are macroscopically occupied and $N_c = N_{c1} + N_{c2}$ with $c = a,b$ are conserved quantities. Such configurations are totally equivalent under the exchange of the site-1 and site-2 populations.

Within this two possible scenarios the effective Hamiltonian involving modes a_2 and b_1 read

$$\hat{H}_1 = C(N_a,N_b) + \sigma_a \hat{N}_{a2} + \sigma_b \hat{N}_{b1} - t_a\sqrt{N_a}\,(a_2^\dagger + a_2) - t_b\sqrt{N_b}\,(b_1^\dagger + b_1)\,, \tag{6.20}$$

with

$$C(N_a,N_b)=\frac{1}{2}\sum_{c=a,b}U_c\Big(N_c^2-N_c\Big)\,,\quad \sigma_a=U_{ab}N_b-U_aN_a\,,\quad \sigma_b=WN_a-U_bN_b\,. \tag{6.21}$$

The opposite case $N_{a1}<<N_a$ and $N_{b2}<<N_b$ leads to the effective Hamiltonian

$$\hat{H}_2=C(N_a,N_b)+\sigma_a\hat{N}_{a1}+\sigma_b\hat{N}_{b2}-t_a\sqrt{N_a}\,(\hat{a}_1^\dagger+\hat{a}_1)-t_b\sqrt{N_b}\,(\hat{b}_2^\dagger+\hat{b}_2)\,. \tag{6.22}$$

The two Hamiltonians are then diagonalized through the Bogoliubov approach by considering the maximally-occupied modes according to the two cases (6.19). We remand to [57] for the detailed calculations of the diagonalization process through the Bogoliubov scheme.
For the first configuration of bosons (6.19), corresponding to the case in which Hamiltonian $\hat{H}\simeq\hat{H}_1$, the energy eigenvalues are found to be

$$E_1(N_{a2},N_{b1})\simeq E_0(N_a,N_b)+\sigma_a\,N_{a2}+\sigma_b\,N_{b1}\,, \tag{6.23}$$

with

$$E_0(N_a,N_b)=\sum_{c=a,b}\left[\frac{U_c}{2}\big(N_c^2-N_c\big)-\frac{t_c^2N_c}{\sigma_c}\right]\,, \tag{6.24}$$

and

$$\sigma_a=U_{ab}N_b-U_aN_a\,,\quad \sigma_b=U_{ab}N_a-U_bN_b\,. \tag{6.25}$$

Note that the general conditions $U_a\neq U_b$ and $t_a\neq t_b$ have been kept since they do not affect the diagonalization process. The eigenvalues of the 2-species Hamiltonian in the strong-interaction regime $|U_{ab}|>U$ are illustrated in the right panel of FIG. 6.4 in the repulsive case.

Also in this case, the eigenvalues provided by equation (6.23) and the eigenvalues determined numerically show an excellent agreement. The eigenstates corresponding to the eigenvalues (6.23) are

$$|E_1(N_{b1},N_{a2})\rangle=|N_{a1}\rangle|z_{b1},N_{b1}\rangle|z_{a2},N_{a2}\rangle|N_{b2}\rangle \tag{6.26}$$

(recall that $N_{b2} = N_b - N_{b1}$ and $N_{a1} = N_a - N_{a2}$) where the two generalized Glauber coherent states [104]

$$|z_{b1}, N_{b1}\rangle = \hat{D}(z_{b1})|N_{b1}\rangle \,, \quad |z_{a2}, N_{a2}\rangle = \hat{D}(z_{a2})|N_{a2}\rangle \tag{6.27}$$

incorporate the displacement operators $\hat{D}(z_{a2})$ and $\hat{D}(z_{b1})$. The latter ensure the reduction of Hamiltonian $\hat{H}$ to the diagonal form for $z_{a2} \equiv t_a\sqrt{N_a}/\sigma_a$, and $z_{b1} \equiv t_b\sqrt{N_b}/\sigma_b$.

Formula (6.23) shows that the lowest energy state of the double-well system is found for $N_{b1} = N_{a2} = 0$ which gives

$$|E_1(0,0)\rangle = |N_a\rangle|z_{bL}\rangle|z_{aR}\rangle|N_b\rangle \,. \tag{6.28}$$

In this case $|z_{b1}, N_{b1}\rangle$ and $|z_{a2}, N_{a2}\rangle$ reduce to two Glauber coherent states $|z_{b1}\rangle$ and $|z_{a2}\rangle$ implying that the minimum-uncertainty relation of boson operators reaches its optimized form in the ground state.

The same diagonalization scheme can be applied to the case $N_{a1} \ll N_{a2}$, $N_{b2} \ll N_{b1}$ and implies the approximation $H \simeq H_2$ described by formula (6.22). In this case the eigenvalues and the eigenstates of $\hat{H}_2$ are found to be

$$E_2(N_{a1}, N_{b2}) \simeq E_0(N_a, N_b) + \sigma_a \, N_{a1} + \sigma_b \, N_{b2} \,, \tag{6.29}$$

and

$$|E_2(N_{aL}, N_{bR})\rangle = |z_{aL}, N_{aL}\rangle|N_{bL}\rangle|N_{aR}\rangle|z_{bR}, N_{bR}\rangle \,. \tag{6.30}$$

Following the same lines as before, it is possible to determine the conditions $z_{a1} \equiv t_a\sqrt{N_a}/\sigma_a$, and $z_{b2} \equiv t_b\sqrt{N_b}/\sigma_b$ taking the Hamiltonian into the diagonal form. For $N_{a1} = N_{b2} = 0$ the lowest energy eigenvalue is achieved which satisfies $E_2(0,0) = E_0(N_a, N_b) \equiv E_1(0,0)$ and is associated with $|E_2(0,0)\rangle = |z_{a1}\rangle|N_a\rangle|N_b\rangle|z_{b2}\rangle$ again containing two Glauber coherent states. Due to the degeneracy of the Bogoliubov spectrum (eigenvalues (6.23) and (6.29) are identical), the obvious form of the ground state (gs) is thus given by

$$|E_{gs}\rangle = \frac{1}{\sqrt{2}}\Big(|E_1(0,0)\rangle + |E_2(0,0)\rangle\Big) \,, \tag{6.31}$$

which well reproduces qualitatively the behavior of the ground state illustrated in the second row of FIG. 6.2 for U_{ab} sufficiently larger than U. Weakly-excited states can be derived together with their eigenvalues by constructing suitable symmetrized combinations of equal-energy states $|E_{\pm}(q,p)\rangle = (|E_1(q,p)\rangle \pm |E_2(p,q)\rangle)/\sqrt{2}$ where $N_{a2} = N_{a1} = q$ and $N_{b2} = N_{b1} = p$. The degeneracy characterizing such states, well known for a system of two symmetric wells with a single atomic species [105], can be removed by applying to states $|E_{\pm}(q,p)\rangle$ the approximation scheme developed in reference [106] for a double-well potential.

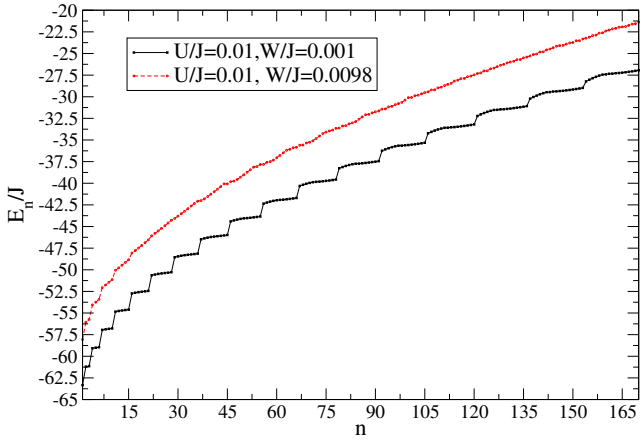

Fig. 6.6 Numerical calculation of the energy levels of model(6.1). $N_a = 30$, $N_b = 40$, $U_a/t = U_b/t \equiv U/t = 0.01$. The spectral collapse is illustrated by comparing the spectrum for $U_{ab}/t = 0.001$ (squares-solid) and $U_{ab}/t = 0.0098$ (circle-dashed). Horizontal axis: Excitation number n. Vertical axis: eigenvalues E_n of Hamiltonian (6.1) in units of t.

We now move to consider the attractive case in the strong interaction regime. Here the two bosonic species features a mixed and coupled state in which both bosonic fields tend to occupy the same lattice site leaving the remaining one empty. In the strongly-attractive interaction regime, namely for $|U_{ab}|$ sufficiently larger than U and $U_{ab} < 0$, the two configurations describing the ground state of the system are

$$\begin{cases} N_{a2} << N_{a1} \simeq N_a\,, \quad N_{b2} << N_{b1} \simeq N_b\,, \\ \\ N_{a1} << N_{a2} \simeq N_a\,, \quad N_{b1} << N_{b2} \simeq N_b\,, \end{cases} \tag{6.32}$$

where both the possibilities entail the localization of the two species in one of the two wells. Due to the attractive interaction the macroscopically occupied modes are

those corresponding to the same well for each population. The Hamiltonian of the system in this case features the eigenvalues

$$E_3(N_{a2},N_{b2}) \simeq \tilde{E}_0(N_a,N_b) + \sigma_a\, N_{a2} + \sigma_b\, N_{a1}\ , \tag{6.33}$$

The equivalent spectrum found by exchanging left and right populations is given by the formula:

$$E_4(N_{a1},N_{b1}) \simeq \tilde{E}_0(N_a,N_b) + \sigma_a\, N_{a1} + \sigma_b\, N_{b1}\ , \tag{6.34}$$

where

$$\tilde{E}_0(N_a,N_b) = E_0(N_a,N_b) - |U_{ab}|N_aN_b. \tag{6.35}$$

here E_0 is given by Eq. (6.24) and the inter-species interaction U_{ab} has been replaced with $|U_{ab}|$ in σ_a and σ_b. The right panel of FIG. 6.5 illustrates the Bogoliubov spectrum (6.33) and the numerical spectrum for the two-sites BH model in the strong-interaction attractive case $|U_{ab}| > U$, $U_{ab} < 0$. As in the repulsive case, an excellent agreement characterizes the Bogoliubov and numerical eigenvalues (at sufficiently low energies).

6.3.3 Range of validity of the Bogoliubov approximation

To better illustrate the range of validity of the Bogoliubov scheme, we compare the Bogoliubov and the numerical spectrum for a number of energy levels ($n = 40$) larger than that of FIGs. 6.4 and 6.5. FIG. 6.7 shows that their agreement remains qualitatively satisfactory when n is increased. Deviations become more and more visible for n larger than $n \sim 30$, but overall the Bogoliubov eigen-energies well reproduce the numerical ones. Both the case $U_{ab} < U$ (left panel) and $U_{ab} > U$ (right panel) are considered for $U_{ab} > 0$. The same results can be shown to hold in the attractive case. For $|U_{ab}| > U$ and large number of bosons, the agreement between the exact numerical diagonalization and the Bogoliubov scheme can be estimated by calculating the relative error as a function of parameters σ_a and σ_b. This is defined by

$$\Delta E_n = \sqrt{\frac{\sum_n (E_n - E_{n,B})^2}{\sum_n E_n^2}}\ , \tag{6.36}$$

where E_n and $E_{n,B}$ refer to the levels obtained numerically and from the Bogoliubov spectrum (6.23), respectively. FIG. 6.8 shows the dependence of ΔE_n from σ_a and

σ_b at fixed $W > 0$ and U. σ_a and σ_b can be varied by increasing the boson number N since $\sigma_a = (3U_{ab} - 2U)N/5$ and $\sigma_b = (2U_{ab} - 3U)N/5$ with a fixed population ratio $N_a/N_b = 2/3$ (see (6.25)). The rapid decreasing of ΔE_n for large N (in Fig. 6.8, $\sigma_a = 8$, $\sigma_b = 1$ correspond to $N = 130$) highlights that, in the semiclassical limit, the Bogoliubov spectrum approaches the numerical one (the same results are found in the attractive case $U_{ab} < 0$).

It can be noticed that, the only *caveat* in applying the Bogoliubov scheme concerns the ratio N_a/N_b and U/U_{ab}. A careful choice of the latter quantities must be done in order to avoid possible diverging behavior of the constant energy (6.24). On the other hand, this pathology does not affect the Bogoliubov spectrum found in section (6.3.1) for $|U_{ab}| < U$.

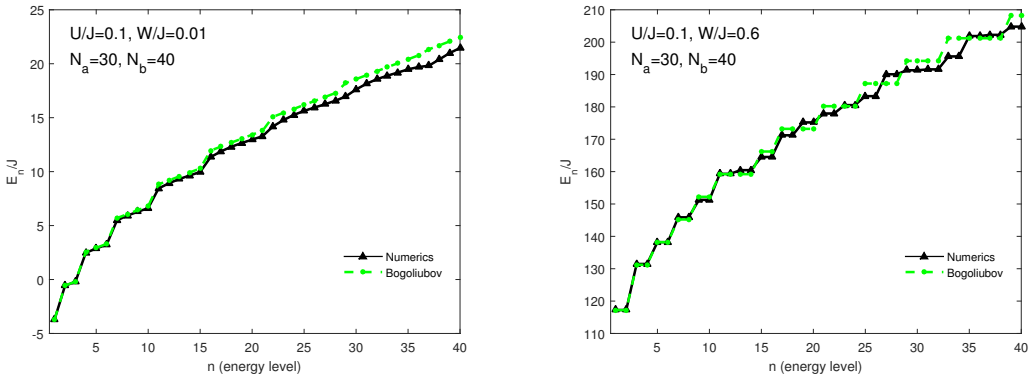

Fig. 6.7 In these panels we show that the agreement of the Bogoliubov and the numerical spectrum remains satisfactory even for a larger number of energy levels. Deviations become more and more visible for n larger than $n \sim 30$. Both the case $U_{ab} < U$ (left panel) and $U_{ab} > U$ (right panel) are considered for $U_{ab} > 0$.

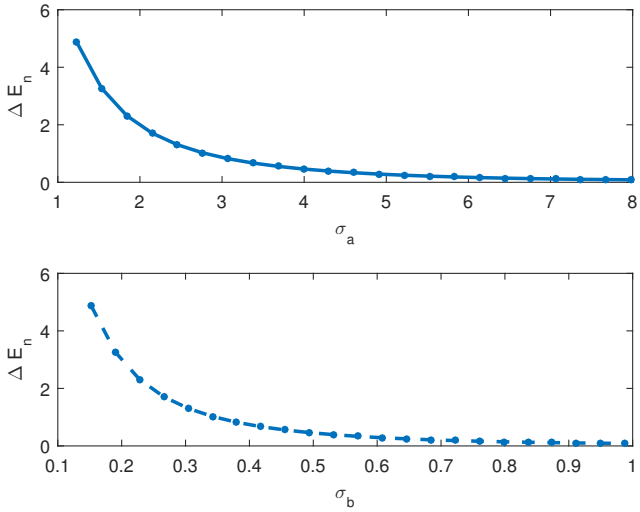

Fig. 6.8 Relative error ΔE_n, described by formula (6.36), as a function of σ_a (upper panel) and σ_b (lower panel), for $U_{ab} = 0.169$, and $U = 0.1$ (see eq. (6.25)). Both σ_a and σ_b are varied increasing N with $N_a/N_b = \frac{2}{3}$. The two panels show how the Bogoliubov spectrum approaches the numerical spectrum in the limit $N \gg 1$.

Conclusion

In this thesis we reported on the work carried out during my years of PhD and published in the papers [55–57]. Motivated by recent studies on two-components systems, we have investigated the properties of ultra-cold bosonic mixtures. We mainly focused on mixture of a twin-species bosonic mixture trapped in a 2D optical lattice. We studied the system under different lattice topologies and filling factor conditions. The study has been largely carried out by means of path-integral quantum Monte Carlo simulations by the two-worm algorithm. When the complexity of the model allowed it we also provided some numerical and analytical results.

We have reconstructed the ground-state phase diagram for the twin species model at integer total filling $n = 1$. We observed different quantum phases depending from the interplay between inter- and intra-species potentials. We have observed a demixed superfluid phase and demixed Mott-Insulator phase when the inter-species interaction becomes greater than the intra- species repulsion, and a double superfluid phase or a supercounterflow otherwise. We have focused our investigation to determine under which conditions these quantum phases can be stabilized and detected, paying particular attentions to the features of demixed quantum phases. Demixed phases, feature spatial separation of the two components on the lattice and manifest themselves experimentally with anisotropic time of flight images.

On the other hand we showed that, the $T = 0$ phase diagram for generic non-integer filling factors exhibits a much simpler form leading to the stabilization of only two-quantum phases, namely: demixed superfluid for $U_{ab} > U$ and double superfluid otherwise. In this situation we studied also the properties of phase separation, showing that stronger filling results in a sharper signature of the demixing between the two components. In order to provide more reliable results closer to real experimental setups, we moved to consider the system trapped in a harmonic potential. We did this in both the weakly- and strongly-interacting regimes. We

found that, even in the trapped case, the demixed quantum phases can be stabilized as far as the condition $U_{ab} > U$ is satisfied, and that if the interaction is weak enough only superfluid-like quantum phases are allowed. This results in mixtures either completely double-superfluids or completely demixed superfluids depending on the ratio between inter- and intra-species interaction. Furthermore, we found that within the strong interaction regime, the local filling factor imposed by the presence of the trap leads to the formation of spatial-shell structures where different quantum phases can coexist within the trap. In this regime shell of incompressible supercounterflow and demixed Mott-Insulator phases have been found intercalated by shells o double superfluid or demixed superfluid.

We then studied the system at finite temperature showing that temperature fluctuations progressively destroy spatial separation between the two species with signatures visible also in the momentum distribution. We performed the study both in the homogeneous/trapped conditions and we showed how this competition between phase separation and thermal fluctuations can be very well described by the behaviour of the demixing parameter Δ. In both weakly- and strongly-interacting regimes the parameter Δ is suppressed in a temperature range of the order of the tunneling energy suggesting its application as a thermometer. We then proposed a new route for thermometry of strongly-correlated binary mixtures capable to exploits the thermometric properties of the experimentally-measurable demixing parameter in order to obtain information on the temperature of the system. This method seems to be capable of working on a broad range of interaction regimes. It can be tared and validated through independent techniques, and it seems to be particularly suitable in the regime where "quantum magnetism" is expected. This feature is of a particular interest as, with the recent observations of anti-ferromagnetic correlations, reliable thermometry in optical lattices for strongly-interacting regimes is sorely needed to advance the field of 'quantum magnetism' with ultracold atoms.

Finally, we investigated the system of two bosonic components in a double well potential (well described by a four space-mode BH model) by applying the Bogoliubov approach. We showed how the fundamental properties of the mixed/demixed phase transitions can be derived analytically also for this simple model, and how this transition is directly related to and well represented by the change of the algebraic structure characterizing the model Hamiltonian. This is witnessed by the spectral collapse of the eigenvalues spectrum. Furthermore by solving the problem numerically,

we showed how the Bogoliubov approximation well reproduce the exact energy spectrum determined numerically and the correct value of the ground-state energy.

Acknowledgements

I would like to thank my tutor Prof. Vittorio Penna for all the patient, time, help and the support provided during these three years of PhD. Barbara Capogrosso-Sansone for the amazing time spent at the University of Oklahoma (OU), all the fruitful discussions and suggestions, and for being so kind and patient on teaching me the "most profound secrets" of the Worm-Algorithm Quantum Monte Carlo. I would like also to thank Francesco Minardi for his help, support, professionality, and useful suggestions on the experimental side.

Furthermore, I'd like to thank all the PhD students of the Department of Applied Science and Technology (DISAT) of the Politecnico di Torino for all the amazing time, fun, lunches, sushi, coffees, AperiDISAT and smiles we have had together during these three years of PhD. A special thanks goes to Sala Dottorandi *Giovanni Rana* Secondo Piano, to Patrick and Evelyn, to Sere, Paolo, Anna "Il Capo", Jacopo, Riccardo and Erik. A particular *Gracias* to Diego and Marcelo for teaching me the S-expanded way of life, for the work we have done together, and for all the discussion, both bomber- and physics-related. Finally, for all the reasons listed above, and infinitely more, I'd like to say Thank You to Lucretzia. Being the Absolute-Gnagna of the PhD in Physics, being absolutely special, or having lost the Seminar-challenge, are just some of those.

This thesis was supported by MIUR (PRIN 2010LLKJBX). The computing for this thesis was performed at the OU Supercomputing Center for Education and Research (OSCER) at the University of Oklahoma (OU), Norman Oklahoma, USA.

References

[1] A. B. Kuklov and B.V. Svistunov, Phys. Rev. Lett. 90, 100401 (2003).

[2] A. B. Kuklov, and B. V. Svistunov, Phys. Rev. Lett. 114, 149901 (2015).

[3] L.-M. Duan, E. Demler and M. D. Lukin, Phys. Rev. Lett. 91, 090402 (2003).

[4] E. Altman, W. Hofstetter, E. Demler, and M. D. Lukin, New J. Phys. 5, 113 (2003).

[5] A. B. Kuklov, N. Prokof'ev, and B. V. Svistunov, Phys. Rev. Lett. 92, 050402 (2004).

[6] A. Argüelles and L. Santos, Phys. Rev. A 75, 053613 (2007).

[7] A. Hu, L. Mathey, I. Danshita, E. Tiesinga, C. J. Williams, and C. W. Clark, Phys. Rev. A 80, 023619 (2009).

[8] A. Hubener, M. Snoek, and W. Hofstetter, Phys. Rev. B 80, 245109 (2009).

[9] S. G. Söyler, B. Capogrosso-Sansone, N. V. Prokof'ev, B. V. Svistunov, New J. Phys. 11, 073036 (2009).

[10] B. Capogrosso-Sansone, S. G. Söyler, N. V. Prokof'ev, and B. V. Svistunov, Phys. Rev. A 81, 053622 (2010).

[11] T. Oghoe, and N. Kawashima, Phys. Rev. A 83, 023622 (2011).

[12] C.-M. Chung, S. Fang, and P. Chen, Phys. Rev. B 85, 214513 (2012).

[13] Y. Li, L. He, and W. Hofstetter, New J. Phys. 15, 093028 (2013).

[14] Y. Nakano, T. Ishima, N. Kobayashi, T. Yamamoto, I. Ichinose and T. Matsui, Phys. Rev. A 85, 023617 (2012).

[15] J.-P. Lv, Q.-H. Chen, and Y. Deng, Phys. Rev. A 89, 013628 (2014).

[16] A. Isacsson, Min-Chul Cha, K. Sengupta, and S. M. Girvin, Phys. Rev. B 72, 184507 (2005).

[17] M. Guglielmino, V. Penna and B. Capogrosso-Sansone, Laser Physics 21, 1443 (2011).

[18] R. V. Pai, J. M. Kurdestany, K. Sheshadri, R. Pandit, Phys. Rev. B 85, 214524 (2012).

[19] L. Mathey, Phys. Rev. B 75, 144510 (2007).

[20] M. Iskin, Phys. Rev. A 82, 033630 (2010).

[21] T. Mishra, R. V. Pai, and B. P. Das, Phys. Rev. A 76, 013604 (2007).

[22] P. Jain and M. Boninsegni Phys. Rev. A 83, 023602 (2011).

[23] T. Roscilde and J. I. Cirac, Phys. Rev. Lett. 98, 190402 (2007).

[24] P. Buonsante, S. M. Giampaolo, F. Illuminati, V. Penna, and A. Vezzani, Phys. Rev. Lett. 100, 240402 (2008).

[25] M. Guglielmino, V. Penna and B. Capogrosso-Sansone, Phys. Rev. A 82, 021601(R) (2010).

[26] D. Benjamin and E. Demler, Phys. Rev. A 89, 033615 (2014).

[27] J. Catani, L. De Sarlo, G. Barontini, F. Minardi, and M. Inguscio, Phys. Rev. A 77, 011603(R) (2008).

[28] G. Thalhammer, G. Barontini, L. De Sarlo, J. Catani, F.Minardi and M. Inguscio, Phys. Rev. Lett. 100, 210402 (2008).

[29] B. Gadway, D. Pertot, R. Reimann, and D. Schneble, Phys. Rev. Lett. 105, 045303 (2010).

[30] B. Gadway, D. Pertot, J. Reeves, D. Schneble, Nature Physics 8, 544 (2012).

[31] P. Soltan-Panahi, J. Struck, P. Hauke, A. Bick, W. Plenkers, G. Meineke, C. Becker, P. Windpassinger, M. Lewenstein and K. Sengstock, Nat. Phys. 7, 434 (2011).

[32] P. Soltan-Panahi, D. S. Luhmann, J. Struck, P. Windpassinger and K. Sengstock, Nature Physics 8, 71 (2012)

[33] M. Guglielmino, V. Penna and B. Capogrosso-Sansone, Phys. Rev. A 84, 031603(R) (2011).

[34] W. S. Bakr, J. I. Gillen, A. Peng, S. Fölling, and M. Greiner, Nature 462, 74 (2009).

[35] J. F. Sherson, C. Weitenberg, M. Endres, M. Cheneau, I. Bloch and S.Kuhr, Nature 467, 69 (2010).

[36] L. W. Cheuk, M. A. Nichols, M. Okan, T. Gersdorf, V. V. Ramasesh, W. S. Bakr, T. Lompe and M. W. Zwierlein, Phys. Rev. Lett. 114, 193001 (2015).

[37] M. F. Parsons, F. Huber, A. Mazurenko, C. S. Chiu, W. Setiawan, K. Wooley-Brown, S. Blatt, and M. Greiner, Phys. Rev. Lett. 114, 213002 (2015).

[38] E. Haller, J. Hudson, A. Kelly, D. A. Cotta, B. Peaudecerf, G. D. Bruce, and S. Kuhr, Nat. Phys.İ1, 738 (2015).

[39] L. W. Cheuk, M. A. Nichols, K. R. Lawrence, M. Okan, H. Zhang, and M. W. Zwierlein, Phys. Rev. Lett. 116, 235301 (2016).

[40] S. G. Söyler, B. Capogrosso-Sansone, N. V. Prokof'ev, and B. V. Svistunov, New J. Phys. 11, 073036 (2009).

[41] I. Bloch, J. Dalibard, and W. Zwerger, Rev. Mod. Phys. 80, 885 (2008).

[42] D. C. McKay and B. DeMarco, Reports on Progress in Physics 74, 54401 (2011).

[43] D. M. Weld, P. Medley, H. Miyake, D. Hucul, D. E. Pritchard, and W. Ketterle, Phys. Rev. Lett. 103, 245301 (2009); D. M. Weld, H. Miyake, P. Medley, D. E. Pritchard, and W. Ketterle, Phys. Rev. A 82, 51603 (2010).

[44] S. Nascimbéne, N. Navon, K. J. Jiang, F. Chevy, and C. Salomon, Nature 463, 1057 (2010).

[45] D. McKay and B. DeMarco, New J. Phys. 12, 55013 (2010).

[46] D. McKay and B. DeMarco, New J. Phys. 12, 55013 (2010).

[47] M. Hohmann, F. Kindermann, T. Lausch, D. Mayer, F. Schmidt, and A. Widera, Phys. Rev. A 93, 43607 (2016).

[48] R. Olf, F. Fang, G. E. Marti, A. MacRae, and D. M. Stamper-Kurn, Nat. Phys. 11, 720 (2015).

[49] R. A. Hart, P. M. Duarte, T.-L. Yang, X. Liu, T. Paiva, E. Khatami, R. T. Scalettar, N. Trivedi, D. A. Huse, and R. G. Hulet, Nature 519, 211 (2015).

[50] M. F. Parsons, A. Mazurenko, C. S. Chiu, G. Ji, D. Greif, and M. Greiner, arXiv:1605.02704 (2016).

[51] L. W. Cheuk, M. A. Nichols, K. R. Lawrence, M. Okan, H. Zhang, E. Khatami, N. Trivedi, T. Paiva, M. Rigol, and M. W. Zwierlein, Science 353, 6305 (2016).

[52] J. H. Drewes, L. A. Miller, E. Cocchi, C. F. Chan, D. Pertot, F. Brennecke, and M. Kohl, arXiv:1607.00392 (2016).

[53] N.V. Prokof'ev, B.V. Svistunov, I.S. Tupitsyn - Phys. Lett. A 238 253-257 (1998).

[54] N.V. Prokof'ev, B.V. Svistunov, I.S. Tupitsyn - Zh. E ksp. Teor. Fiz. 114, 570-590 (1998).

[55] F. Lingua, B. Capogrosso-Sansone, M. Guglielmino, and V. Penna, Phys. Rev. A 92, 053610 (2015).

[56] F. Lingua, B. Capogrosso-Sansone, F. Minardi, and V. Penna, arXiv:1609.08352 (2016).

[57] F. Lingua, G. Mazzarella and V. Penna, J. Phys. B. 49, 205005 (2016).

[58] I. Bloch, J. Dalibard and W. Zwerger, Rev. Mod. Phys. 80, 885 (2008).

[59] J. Hubbard, Proc. R. Soc. A 276, 1365 (1963).

[60] J. Hubbard, Proc. R. Soc. A 277, 1369 (1964).

[61] J. Hubbard, Proc. R. Soc. A, 281 1386 (1964).

[62] J. Hubbard, Proc. R. Soc. A, 285 1403 (1965).

[63] J. Hubbard, Proc. R. Soc. A, 296 1444 (1967).

[64] M. Lysebo and L. Veseth, Phys. Rev. A 81, 032702 (2010).

[65] K. Suthar, and D. Angom, Phys. Rev. A 93, 063608 (2016).

[66] P. Jain, S. Moroni, M. Boninsegni, L. Pollet, Phys. Rev. A 88, 033628 (2013).

[67] Y. Eto, M. Kunimi, H. Tokita, H. Saito, and T. Hirano, arXiv:1505.04882v1

[68] S. Tojo, Y. Taguchi, Y. Masuyama, T. Hayashi, H. Saito and T. Hirano, Phys. Rev. A 82, 033609 (2010).

[69] S. B. Papp, J. M. Pino, and C. E. Wieman, Phys. Rev. Lett. 101, 040402 (2008).

[70] E. Nicklas, H. Strobel, T. Zibold, C. Gross,y B. A. Malomed, P. G. Kevrekidis, and M. K. Oberthaler, Phys. Rev. Lett. 107, 193001 (2011)

[71] E. Nicklas, W. Muessel, H. Strobel, P. G. Kevrekidis, M. K. Oberthaler, arXiv: 1407.8049v1

[72] P. Ao and S. T. Chui, Phys. Rev. A 58, 6 4836 (1998).

[73] L. Pollet, M. Troyer, K. Van Houcke and S. M. A. Rombouts, Phys. Rev. Lett. 96, 190402 (2006).

[74] L. Pollet, C. Kollath, U. Schollwock and M. Troyer, Phys. Rev. A 77, 023608 (2008).

[75] F. Zhan and I. P. McCulloch, Phys. Rev. A 89, 057601 (2014)

[76] E. L. Pollock and D. M. Ceperley, Phys. Rev. B 36, 8343 (1987).

[77] T. Holstein and H. Primakoff, Phys. Rev. 58, 1098 (1940).

[78] V. A. Kashurnikov, N. V. Prokof'ev and B. V. Svistunov Phys. Rev. A 66, 031601 (2002).

[79] G. G. Batrouni, V. Rousseau, R. T. Scalettar, M. Rigol, A. Muramatsu, P. J. H. Denteneer, M. Troyer, Phys. Rev. Lett. 89, 117203 (2002).

[80] S. Folling, A. Widera, T. Muller, F. Gerbier and I. Bloch, Phys. Rev. Lett. 97, 060403 (2006).

[81] Ma. Rigol, G. G. Batrouni, V. G. Rousseau, R. T. Scalettar, Phys. Rev. A 79, 053605 (2009).

[82] T. Mishra, R. V. Pai, and B. P. Das, Phys. Rev. A 76, 013604 (2007).

[83] P. Buonsante, S. M. Giampaolo, F. Illuminati, V. Penna, and A. Vezzani, Phys. Rev. Lett. 100, 240402 (2008).

[84] T. Roscilde, and J. I. Cirac, Phys. Rev. Lett. 98, 190402 (2007).

[85] D. McKay and B. DeMarco, New J. Phys. 12, 55013 (2010).

[86] B. Capogrosso-Sansone, S. Söyler, N. Prokofev, and B. V. Svistunov, Phys. Rev. A 81, 53622 (2010).

[87] Y. Kato, Q. Zhou, N. Kawashima, and N. Trivedi, Nat. Phys. 4, 617 (2008).

[88] G. K. Campbell, J. Mun, M. Boyd, P. Medley, A. E. Leanhardt, L. G. Marcassa, D. E. Pritchard, and W. Ketterle, Science 313, 649 (2006).

[89] W. S. Bakr, P. M. Preiss, M. E. Tai, R. Ma, J. Simon, and M. Greiner, Nature 480, 500 (2011).

[90] M. Albiez, R. Gati, J. Fölling, S. Hunsmann, M. Cristiani and M. K. Oberthaler, Phys. Rev. Lett. 95, 010402 (2005).

[91] A. Barone and G. Paternò *Physics and Applications of the Josephson effect*, New York: Wiley (1982); H. Otha in *SQUID: Superconducting Quantum Devices and their Applications*, edited by H.D. Hahlbohm and H. Lubbig, Berlin: de Gruyter (1977)

[92] S. Ashhab and Lobo C, Phys. Rev. A 66, 013609 (2002).

[93] X. Q. Xu, L. H. Lu, and Y. Q. Li, Phys. Rev. A 78, 043609 (2008).

[94] I. I. Satjia, R. Balakrishnan, P. Naudus, J. Heward, M. Edwards, and C. W. Clark, Phys. Rev. A 79, 033616 (2009).

[95] G. Mazzarella, M. Moratti, L. Salasnich, M. Salerno and F. Toigo, J. Phys. B: At. Mol. Opt. Phys. 42, 125301 (2009).

[96] B. Juliá-Díaz, M. Melé-Messeguer , M. Guilleumas, and A. Polls, Phys. Rev. A 80, 043622 (2009).

[97] G. Mazzarella, B. Malomed, L. Salasnich, M. Salerno, and F. Toigo, J. Phys. B: At. Mol. Opt. Phys. 44, 035301 (2011).

[98] R. Gilmore, C. M. Bowden, and L. M. Narducci, Phys. Rev. A 12, 1019 (1975).

[99] P. Buonsante, and V. Penna, J. Phys. A: Math. Gen. 41, 175301 (2008).

[100] P. Buonsante, V. Penna, and A. Vezzani, Phys. Rev. A 82, 043615 (2010).

[101] V. Penna, Phys. Rev. E 87, 052909 (2013).

[102] V. Penna and F. A. Raffa, Int. J. Quantum Inform. 12, 1560010 (2014).

[103] S. Felicetti, J. S. Pedernales, I. L. Egusquiza, G. Romero, L. Lamata, D. Braak, and E. Solano, Phys. Rev. A 92, 033817 (2015).

[104] A. I. Solomon, Y. Feng and V. Penna, Phys. Rev. B 60, 3044 (1999).

[105] G. J. Milburn, J. Corney, E. M. Wright and D. F. Walls, Phys. Rev. A 55, 4318 (1997).

[106] L. D. Landau and E. M. Lifsits Quantum Mechanics (Oxford: Pergamon) (1957).

Appendix A

Derivation of $\mathscr{H}_0$

As shown in equation (1.72) the kinetic part $\mathscr{H}_0$ of the hamiltonian $\mathscr{H}$ describing a weakly interacting Bose-gas trapped in a periodic potential takes the form:

$$\hat{\mathscr{H}_0} = \sum_{n,\vec{k}} \varepsilon_n(k) b^{\dagger}_{nk} b_{nk} \tag{A.1}$$

where $\varepsilon_n(k)$ are the Bloch eigenvalues derived explicitly from the Bloch Theorem. If the single particle states are extremely localized in space, then the expression for the Block eigenvalues reduces to

$$\varepsilon_n(k) = 2\varepsilon_n \sum_{r\in x,y,z} [1 - \cos(a_r k_r)] \tag{A.2}$$

where a_r is the period of the lattice in direction $r = x, y, z$. Is now possible to swap from the Bloch basis to the Wannier basis representation

$$b_{nk} = \sum_i \frac{1}{\sqrt{M}} a_{ni} e^{-i\vec{k}\cdot\vec{R}_i}. \tag{A.3}$$

by substituting (A.3) into (A.1), the hamiltonian $\hat{\mathscr{H}}_0$ becomes:

$$\begin{aligned}
\hat{\mathscr{H}}_0 = \sum_{n,\vec{k}} \varepsilon_n(k) b^\dagger_{nk} b_{nk} = \sum_{n,\vec{k}} \varepsilon_n(k) \frac{1}{M} \sum_i a^\dagger_{ni} e^{i\vec{k}\cdot\vec{R}_i} \sum_j a_{nj} e^{-i\vec{k}\cdot\vec{R}_j} = \\
= \frac{1}{M} \sum_n \sum_i \sum_j \sum_{\vec{k}} \varepsilon_n(k) a^\dagger_{ni} a_{nj} e^{i\vec{k}\cdot\vec{R}_i} e^{-i\vec{k}\cdot\vec{R}_j} = \\
= \sum_n \sum_i \sum_j a^\dagger_{ni} a_{nj} \frac{1}{M} \sum_{\vec{k}} \varepsilon_n(k) e^{i\vec{k}\cdot\vec{R}_i} e^{-i\vec{k}\cdot\vec{R}_j} = \\
= \sum_n \sum_i \sum_j a^\dagger_{ni} a_{nj} \frac{1}{M} \sum_{\vec{k}} 2\varepsilon_n [3 - \sum_r \cos(a_r k_r)] e^{i\vec{k}\cdot(\vec{R}_i - \vec{R}_j)} = \\
= \sum_n \sum_i \sum_j a^\dagger_{ni} a_{nj} 6\varepsilon_n \frac{1}{M} \sum_{\vec{k}} e^{i\vec{k}\cdot(\vec{R}_i - \vec{R}_j)} + \\
- \sum_n \sum_i \sum_j a^\dagger_{ni} a_{nj} \frac{1}{M} \sum_{\vec{k}} 2\varepsilon_n \sum_r \cos(a_r k_r) e^{i\vec{k}\cdot(\vec{R}_i - \vec{R}_j)} = \hat{\mathscr{H}}_{01} + \hat{\mathscr{H}}_{02} \quad \text{(A.4)}
\end{aligned}$$

where

$$\hat{\mathscr{H}}_{01} = \sum_n \sum_i \sum_j a^\dagger_{ni} a_{nj} 6\varepsilon_n \frac{1}{M} \sum_{\vec{k}} e^{i\vec{k}\cdot(\vec{R}_i - \vec{R}_j)} \quad \text{(A.5)}$$

$$\hat{\mathscr{H}}_{02} = - \sum_n \sum_i \sum_j a^\dagger_{ni} a_{nj} \frac{1}{M} \sum_{\vec{k}} 2\varepsilon_n \sum_r \cos(a_r k_r) e^{i\vec{k}\cdot(\vec{R}_i - \vec{R}_j)} \quad \text{(A.6)}$$

Solving $\hat{\mathscr{H}}_{01}$ we notice that $\frac{1}{M}\sum_{\vec{k}} e^{i\vec{k}\cdot(\vec{R}_i - \vec{R}_j)} = \delta_{ij}$ by definition of the Fourier Series.

$$\hat{\mathscr{H}}_{01} = \sum_n \sum_i \sum_j a^\dagger_{ni} a_{nj} 6\varepsilon_n \delta_{ij} = 6 \sum_n \varepsilon_n \sum_i a^\dagger_{ni} a_{ni} = 6 \sum_n \varepsilon_n \sum_i \hat{n}_{ni} \quad \text{(A.7)}$$

Term $\hat{\mathscr{H}}_{02}$:

$$\begin{aligned}
\hat{\mathscr{H}}_{02} = - \sum_n \sum_i \sum_j a^\dagger_{ni} a_{nj} \frac{1}{M} \sum_{\vec{k}} 2\varepsilon_n \sum_r \cos(a_r k_r) e^{i\vec{k}\cdot(\vec{R}_i - \vec{R}_j)} = \\
= - \sum_n \sum_i \sum_j a^\dagger_{ni} a_{nj} \frac{1}{M} \sum_{\vec{k}} 2\varepsilon_n \sum_r \cos(a_r k_r) \times \\
\times e^{i\vec{k}\cdot([a_x i_x \vec{u}_x + a_y i_y \vec{u}_y + a_z i_z \vec{u}_z] - [a_x j_x \vec{u}_x + a_y j_y \vec{u}_y + a_z j_z \vec{u}_z])} = \\
= - \sum_n \sum_i \sum_j a^\dagger_{ni} a_{nj} \frac{1}{M} \sum_{\vec{k}} 2\varepsilon_n \sum_r \cos(a_r k_r) e^{i\vec{k}\cdot(\sum_l a_l i_l \vec{u}_l - \sum_l a_l j_l \vec{u}_l)}, \quad \text{(A.8)}
\end{aligned}$$

where indexes r and l run over the three spatial directions x, y and z

$$\hat{\mathscr{H}}_{02} = -\sum_n \sum_i \sum_j a^\dagger_{ni} a_{nj} \frac{1}{M} \sum_{\vec{k}} 2\varepsilon_n \sum_r \cos(a_r k_r) e^{i\vec{k}\cdot\sum_l a_l (i_l - j_l)\vec{u}_l} =$$
$$= -\sum_n \sum_i \sum_j a^\dagger_{ni} a_{nj} \frac{1}{M} \sum_{\vec{k}} 2\varepsilon_n \sum_r \frac{e^{ia_r k_r} + e^{-ia_r k_r}}{2} e^{i\vec{k}\cdot\sum_l a_l (i_l - j_l)\vec{u}_l}. \quad \text{(A.9)}$$

Using the fact that the scalar product $\vec{k}\cdot\vec{u}_l = k_l$ by definition

$$\hat{\mathscr{H}}_{02} = -\sum_n \sum_i \sum_j a^\dagger_{ni} a_{nj} \frac{1}{M} \sum_{\vec{k}} 2\varepsilon_n \sum_r \frac{e^{ia_r k_r} + e^{-ia_r k_r}}{2} e^{i\sum_l a_l (i_l - j_l) k_l} =$$
$$= -\sum_n \sum_i \sum_j a^\dagger_{ni} a_{nj} \frac{1}{M} \sum_{\vec{k}} \varepsilon_n \sum_r (e^{ia_r k_r} e^{i\sum_l a_l (i_l - j_l) k_l} + e^{-ia_r k_r} e^{i\sum_l a_l (i_l - j_l) k_l})$$
$$= -\sum_n \sum_i \sum_j a^\dagger_{ni} a_{nj} \frac{1}{M} \sum_{\vec{k}} \varepsilon_n \sum_r (e^{i\sum_l a_l (i_l - j_l + \delta_{lr}) k_l} + e^{i\sum_l a_l (i_l - j_l - \delta_{lr}) k_l}) \quad \text{(A.10)}$$

Analyzing the terms

$$\sum_{r\in\{x,y,z\}} e^{i\sum_l a_l (i_l - j_l \pm \delta_{lr}) k_l} = \sum_{r\in\{x,y,z\}} e^{i\vec{k}\cdot(\vec{R}_i - \sum_l a_l (j_l \pm \delta_{lr})\vec{u}_l)} \quad \text{(A.11)}$$

we notice that $\sum_l a_l (j_l \pm \delta_{lr})\vec{u}_l = \vec{R}_{j_{r_\pm}}$ denotes nothing more than the coordinate of the two nearest neighbor (± 1 lattice step) of the site j along the direction $r = x, y, z$. We can then rewrite the term (A.11) in a more compact form as

$$\sum_{r\in\{x,y,z\}} e^{i\sum_l a_l (i_l - j_l \pm \delta_{lr}) k_l} = \sum_{r\in\{x,y,z\}} e^{i\vec{k}\cdot(\vec{R}_i - \vec{R}_{j_{r_\pm}})} \quad \text{(A.12)}$$

The Hamiltonian term $\hat{\mathscr{H}}_{02}$ takes then the form

$$\hat{\mathscr{H}}_{02} = -\sum_n \sum_i \sum_j a^\dagger_{ni} a_{nj} \frac{1}{M} \sum_{\vec{k}} \varepsilon_n \sum_r \left(e^{i\vec{k}\cdot(\vec{R}_i - \vec{R}_{j_{r_+}})} + e^{i\vec{k}\cdot(\vec{R}_i - \vec{R}_{j_{r_-}})} \right) \quad \text{(A.13)}$$

where $R_{j_{r+}}$ and $R_{j_{r-}}$ are the nearest neighbor sites of j along the direction $r = x, y, z$ in position $+1$ site and -1 site respectively.

$$\hat{\mathscr{H}}_{02} = -\sum_n \sum_i \sum_j a^\dagger_{ni} a_{nj} \varepsilon_n \sum_r \frac{1}{M} \sum_{\vec{k}} \left(e^{i\vec{k}\cdot(\vec{R}_i - \vec{R}_{j_{r_+}})} + e^{i\vec{k}\cdot(\vec{R}_i - \vec{R}_{j_{r_-}})} \right) \quad \text{(A.14)}$$

Exploiting again the property of the Fourier series that $\frac{1}{M}\sum_{\vec{k}} e^{i\vec{k}\cdot(\vec{R}_i-\vec{R}_l)} = \delta_{il}$ we obtain

$$\begin{aligned}\hat{\mathscr{H}}_{02} &= -\sum_n \sum_i \sum_j a^\dagger_{ni} a_{nj} \varepsilon_n \sum_r \left(\delta_{i j_{r_+}} + \delta_{i j_{r_-}}\right) = \\ &= -\sum_n \varepsilon_n \sum_j \left(\sum_{j_{r_+}} a^\dagger_{n j_{r_+}} a_{nj} + \sum_{j_{r_-}} a^\dagger_{n j_{r_-}} a_{nj}\right) = \\ &= -\sum_n \varepsilon_n \sum_{\langle i,j\rangle} a^\dagger_{ni} a_{nj} \quad \text{(A.15)}\end{aligned}$$

where $\langle i, j\rangle$ denotes the sum over nearest neighboring sites.

The Hamiltonian term $\hat{\mathscr{H}}_0$ is finally obtained buy putting together our results

$$\hat{\mathscr{H}}_0 = \hat{\mathscr{H}}_{01} + \hat{\mathscr{H}}_{02} = 6\sum_n \varepsilon_n \sum_i \hat{n}_{ni} - \sum_n \varepsilon_n \sum_{\langle i,j\rangle} a^\dagger_{ni} a_{nj} \quad \text{(A.16)}$$

Appendix B

Derivation of the Two-Species Bose-Hubbard Model

The derivation of Hamiltonian (1.82) is obtained by the expansion of the field operators of the two-species Hamiltonian (1.64) in the Wannier spatial-mode basis. The Hamiltonian of a mixture of two weakly-interacting bosonic gases (1.64) was written as

$$\hat{\mathscr{H}} = \hat{\mathscr{H}}_{0a} + \hat{\mathscr{U}}_a + \hat{\mathscr{H}}_{0b} + \hat{\mathscr{U}}_b + \hat{\mathscr{W}}, \tag{B.1}$$

with

$$\begin{aligned}
\hat{\mathscr{H}}_{0a} &= \int d^3x \hat{\Psi}_a^\dagger(\vec{x}) \Big[-\frac{\hbar^2}{2m}\nabla^2 + V(\vec{x}) \Big] \hat{\Psi}_a(\vec{x}), && \text{(B.2)}\\
\hat{\mathscr{U}}_a &= \frac{U_{0a}}{2} \int d^3x \, (\hat{\Psi}_a^\dagger(\vec{x}))^2 (\hat{\Psi}_a(\vec{x}))^2, && \text{(B.3)}\\
\hat{\mathscr{H}}_{0b} &= \int d^3x \hat{\Psi}_b^\dagger(\vec{x}) \Big[-\frac{\hbar^2}{2m}\nabla^2 + V(\vec{x}) \Big] \hat{\Psi}_b(\vec{x}), && \text{(B.4)}\\
\hat{\mathscr{U}}_b &= \frac{U_{0b}}{2} \int d^3x \, (\hat{\Psi}_b^\dagger(\vec{x}))^2 (\hat{\Psi}_b(\vec{x}))^2, && \text{(B.5)}\\
\hat{\mathscr{W}} &= U_{ab} \int d^3x \hat{\Psi}_a^\dagger(\vec{x}) \hat{\Psi}_a(\vec{x}) \hat{\Psi}_b^\dagger(\vec{x}) \hat{\Psi}_b(\vec{x}) && \text{(B.6)}
\end{aligned}$$

By grouping $\hat{\mathscr{H}}_{0a}$, $\hat{\mathscr{U}}_a$ and $\hat{\mathscr{H}}_{0b}$, $\hat{\mathscr{U}}_b$ such that

$$\begin{aligned}
\hat{\mathscr{H}}_a &= \hat{\mathscr{H}}_{0a} + \hat{\mathscr{U}}_a && \text{(B.7)}\\
\hat{\mathscr{H}}_b &= \hat{\mathscr{H}}_{0b} + \hat{\mathscr{U}}_b && \text{(B.8)}
\end{aligned}$$

we clearly notice that $\hat{\mathscr{H}}_a$ and $\hat{\mathscr{H}}_b$, if expanded in the Wannier representation, give as result the single-species Bose-Hubbard Hamiltonian derived in the previous section (they are the same as (1.66)).

$$\hat{\mathscr{H}}_a = -t_a \sum_{\langle i,j \rangle} a_i^\dagger a_j + \frac{U_a}{2} \sum_i \hat{n}_{ai}(\hat{n}_{ai} - 1) \tag{B.9}$$

$$\hat{\mathscr{H}}_b = -t_b \sum_{\langle i,j \rangle} b_i^\dagger b_j + \frac{U_b}{2} \sum_i \hat{n}_{bi}(\hat{n}_{bi} - 1) \tag{B.10}$$

with $t_a = \varepsilon_{0a}$ ($t_b = \varepsilon_{0b}$) the hopping amplitude of species A (B), and $U_a = U_{0a}$ ($U_a = U_{0b}$) the intra-species interaction of species A (B). The derivation of the Two-Species Bose-Hubbard Model is then accompished by simply expanding the two-body inter-species interaction term (B.6).

Derivation of $\hat{\mathscr{W}}$. Let's start by expanding the two bosonic field-operators in the Wannier basis

$$\hat{\Psi}_a(\vec{x}) = \sum_{ni} W_{ni}(\vec{x}) a_{ni}, \tag{B.11}$$

$$\hat{\Psi}_b(\vec{x}) = \sum_{mj} W_{mj}(\vec{x}) b_{mj}. \tag{B.12}$$

The new expression are then inserted in (B.6)

$$\begin{aligned} \hat{\mathscr{W}} &= U_{ab} \int d^3x \hat{\Psi}_a^\dagger(\vec{x}) \hat{\Psi}_a(\vec{x}) \hat{\Psi}_b^\dagger(\vec{x}) \hat{\Psi}_b(\vec{x}) = \\ &= U_{ab} \sum_{ni} \sum_{lr} \sum_{mj} \sum_{gs} \int d^3x W_{ni}^*(\vec{x}) W_{lr}(\vec{x}) W_{mj}^*(\vec{x}) W_{gs}(\vec{x}) a_{ni}^\dagger a_{lr} b_{mj}^\dagger b_{gs}, \end{aligned} \tag{B.13}$$

using the fact that $\int d^3x W_{ni}^*(\vec{x}) W_{lr}(\vec{x}) W_{mj}^*(\vec{x}) W_{gs}(\vec{x}) = \delta_{irjs}\delta_{nlmg}$

$$\begin{aligned} \hat{\mathscr{W}} &= U_{ab} \sum_{ni} \sum_{lr} \sum_{mj} \sum_{gs} \delta_{irjs}\delta_{nlmg} a_{ni}^\dagger a_{lr} b_{mj}^\dagger b_{gs} = \\ &= U_{ab} \sum_{ni} a_{ni}^\dagger a_{ni} b_{ni}^\dagger b_{ni} = U_{ab} \sum_{ni} \hat{n}_{nai} \hat{n}_{nbi}. \end{aligned} \tag{B.14}$$

Restricting ourselves to the single-band approximation we get

$$\hat{\mathscr{W}} = U_{ab} \sum_i \hat{n}_{ai} \hat{n}_{bi} \tag{B.15}$$

If we substitutes now (B.9), (B.10) and (B.15) into (B.1) we obtain the Two-Species Bose-Hubbard Hamiltonian (1.82) described above:

$$\hat{\mathscr{H}} = \frac{U_a}{2}\sum_i \hat{n}_{ai}(\hat{n}_{ai}-1) - t_a \sum_{\langle i,j\rangle} a_i^\dagger a_j + \\ + \frac{U_b}{2}\sum_i \hat{n}_{bi}(\hat{n}_{bi}-1) - t_b \sum_{\langle i,j\rangle} b_i^\dagger b_j + U_{ab}\sum_i \hat{n}_{ai}\hat{n}_{bi} \quad \text{(B.16)}$$